Numerical computations of the unsteady flow in turbochargers

by

Fredrik Hellström

April 2010
Technical Reports from
Royal Institute of Technology
KTH Mechanics
SE-100 44 Stockholm, Sweden

Akademisk avhandling som med tillstånd av Kungliga Tekniska Högskolan i Stockholm framlägges till offentlig granskning för avläggande av teknologie doktorsexamen onsdagen den 26 Maj 2010 kl 10.15 i sal F3, Lindstedtsvägen 26, Kungliga Tekniska Högskolan, Stockholm.

Universitetsservice US–AB, Stockholm 2010

Abstract Turbocharging the internal combustion (IC) engine is a common technique to increase the power density. If turbocharging is used with the downsizing technique, the fuel consumption and pollution of green house gases can be reduced. In the turbocharger, the energy of the engine exhaust gas is extracted by expanding it through the turbine which drives the compressor by a shaft. If a turbocharged IC engine is compared with a natural aspirated engine, the turbocharged engine will be smaller, lighter and will also have a better efficiency, due to less pump losses, lower inertia of the system and less friction losses. To be able to further increase the efficiency of the IC engine, the understanding of the highly unsteady flow in turbochargers must be improved, which then can be used to increase the efficiency of the turbine and the compressor. The main objective with this thesis has been to enhance the understanding of the unsteady flow in turbocharger and to assess the sensitivity of inflow conditions on the turbocharger performance.

The performance and the flow field in a radial turbocharger turbine working under both non-pulsatile and pulsatile flow conditions has been assessed by using Large Eddy Simulation (LES). To assess the effects of different operation conditions on the turbine performance, different cases have been considered with different perturbations and unsteadiness of the inflow conditions. Also different rotational speeds of the turbine wheel were considered. The results show that the turbine cannot be treated as being quasi-stationary; for example, the shaft power varies for different frequencies of the pulses for the same amplitude of mass flow. The results also show that perturbations and unsteadiness that are created in the geometry upstream of the turbine have substantial effects on the performance of the turbocharger. All this can be summarized as that perturbations and unsteadiness in the inflow conditions to the turbine affect the performance.

The unsteady flow field in ported shroud compressor has also been assessed by using LES for two different operational points. For an operational point near surge, the flow field in the entire compressor stage is unsteady, where the driving mechanism is an unsteadiness created in the volute. For an operational point far away from surge, the flow field in the compressor is relatively much more steady as compared with the former case. Although the stable operational point exhibits back-flow from the ported shroud channels, which implies that the flow into the compressor wheel is disturbed due to the structures that are created in the shear layer between the bulk flow and the back-flow from the ported shroud channels.

Descriptors: Pulsatile flow, radial turbine, centrifugal compressor, pipe flow, effects of inlet conditions, effects of heat transfer, stall, surge, Large Eddy Simulation.

Contents

Paper 1

Paper 2

Paper 3

Paper 4

Paper 5

Paper 6

Paper 7

Paper 8

Part I

Overview and summary

CHAPTER 1

Introduction

Turbocharging the internal combustion (IC) engine is a common technique to increase the power density. By turbocharging and utilizing downsizing technique, the fuel consumption and pollution of green house gases can be reduced. The turbocharger consists of turbine, a compressor and a shaft with supporting bearings. In the turbocharger, the energy of the engine exhaust gas is extracted by expanding it through the turbine which drives the compressor by the shaft. This means that parts of the wasted energy in the exhaust gas, which can be as much as 30-40 % of the chemical energy released by the combustion is used to increase the density of the air admitted to the cylinder. Thereby the power output of the engine can be increased or alternatively the engine size can be reduced, without decreasing the power output. If a turbocharged IC-engine is compared with a natural aspirated engine with the same power output, the turbocharged engine will be smaller, lighter and requires a smaller installation space. The turbocharged IC-engine will also have a better efficiency, due to less pump losses, lower inertia of the system and less the friction losses due to smaller cylinders, valves etc. Due to the design of the IC-engine, with reciprocating pistons, the flow in the exhaust manifold and the turbine is highly unsteady, with the frequency and amplitude of the pulsatile flow determined by the size of the engine, number of cylinders and the operational point.

To be able to further increase the efficiency of the IC-engine, the understanding of the highly unsteady flow in turbochargers must be improved, which then can be used to increase the efficiency of the turbine and the compressor. The objectives of the work described in this thesis are as follows:

- Study in detail and analyze turbine flows under conditions found in IC-engines.
- Assess the sensitivity of boundary conditions on the turbine performance
- Assess the validity and shortcomings of quasi-stationary flow assumption in IC-engine gas management
- Assess the mechanism in a radial compressor that leads to surge

The performance of the turbine working in both non-pulsatile and pulsatile flows has been considered. Also, the flow in the compressor part is assessed with the focus on an operational point closed to surge. The compressor in the turbocharger application is also of the radial type. The operational range of the compressor is limited by choke at high mass flow rate and by surge at low mass flow rates. Additionally surge is an unstable flow phenomenon, which creates unwanted additional noise. Therefore, it is important to extend the operational range of the compressor.

The main focus of the work has been on several components that affect the turbocharging:

- The physics of pulsatile flow in bent pipes which are related to exhaust IC-engine manifolds and are important for generating inflow conditions for the turbine.
- Effects of inflow conditions on the turbine performance for both non-pulsatile and pulsatile flow conditions.
- Effects of heat losses on the turbine performance.
- Radial compressor flow at two operating points and comparing the LES results with existing experimental data.

The approach used for all studies is time resolved three-dimensional numerical flow simulations. The results have been compared to experimental data when such data is available.

The work described in the thesis makes a contribution in understanding the flow in the turbine and its dependence on the boundary conditions, such as the inflow conditions and wall losses. These aspects are of importance from engineering point of view; i.e. for the integration of the turbocharger in the car engine. By improved understanding of the flow, a better understanding of the sources of losses in the turbine is achieved. The experience gained in the computational analysis can help in improving the modeling of such flows. Also, the knowledge of the pulsatile flow and how the turbine behaves under highly unsteady flow conditions can be used when new turbochargers are designed for or integrated into IC-engines. Such knowledge enables one to focus on the factors that mostly affect the performance of the turbocharger. An important aspect is the inflow condition to the turbine and compressor (due to upstream-piping and flow pulsations). By appropriate design and integration work the efficiency of the turbocharger in the system may be improved. The improved understanding of the issues related to the integration of the turbocharger into the IC-engine gas exchange system is the main contribution of this thesis.

The main achievements from this thesis are the following findings:

- The turbine performance is strongly affected by perturbations and unsteadiness of the inflow conditions, but less affected by heat losses at the housing walls. Inlet conditions depend strongly on the shape of the engine exhaust manifold and the flow out of the cylinders.

- The deviation from the quasi-stationary assumption is not constant, and depends on both the considered geometry and flow conditions
- The mechanism that drives the unsteadiness in a ported shroud compressor is an unsteady separation bubble at the tongue. This conclusion is not exclusive since other mechanisms cannot be excluded.

The assessment of the flow in a radial compressor was conducted at the end of the PhD studies when the author had the opportunity to spend about six months at the University of Cincinnati. During this period, the Cincinnati group carried out extensive PIV measurements of the flow in a ported shroud compressor so as to enable an extend of the operational range.

The thesis is organized as follows: In Chapter 2 a brief overview of the steady and unsteady flow in pipes is given. This chapter is followed by Chapter 3 where the features of turbochargers, with focus on the turbine part, are discussed. Chapter 4 consider the used methods. In Chapter 5, the most important results are presented followed by conclusions in Chapter 6. Finally, in Chapter 7, a short summary of the included papers is given.

CHAPTER 2

Non-pulsatile and pulsatile internal flow

The exhaust manifold, situated between the engine and the turbine, can be viewed as being made of straight and curved pipe sections. Therefore, a literature survey on the steady and unsteady flow in different pipe configurations has been conducted to give a brief overview of the pulsatile internal flow in pipes. Also, a numerical study of the non-pulsatile and pulsatile flow has also been conducted, and the results are reported in Paper 1 and in a later chapter.

The most important flow variables for the pulsatile flow are the frequency and the amplitude of the pulsations and the pulse shape. In the engine application, the frequency and the amplitude of the pulsatile flow in the exhaust system will be determined by the numbers of cylinders of the engine and at which operation point the engine is working, i.e. the engine rotational speed and the throttle position. The geometry of the exhaust ports including the valves and the exhaust manifold will also affect the flow into the turbine, since single and double bends will introduce secondary flow, junctions will disturb the flow and there are also pressure waves that will be reflected in the manifold.

2.1. Flow in curved pipes

There are many applications where flow in bent pipes can be found, for example pipe-lines, exhaust systems and the blood flow in arteries. One typical feature of the flow in bent pipes is the so called Dean vortices, which are a pair of counter-rotating vortices. When the flow enters the bend, the fluid is accelerated near the inner wall. Simultaneously, the fluid near the outer wall is decelerated due to the adverse pressure gradient. This induces a secondary flow in the transverse plane of the pipe. Further downstream, the centrifugal force induces a second flow in the central part of the cross section from the inner wall to the outer wall and forms the two counter-rotating vortices, and those vortices are depicted in Figure 2.1.

Sudo *et al.* (1998) investigated the steady turbulent flow in a circular-sectioned 90° bend. The curvature radius ratio, defined as the ratio between the radius of the bend and the pipe radius, was four and the flow was assumed to be turbulent. At the inlet to the bend, φ=0°, the primary flow accelerates near the inner wall. At φ=30° the secondary flow starts to develops into a

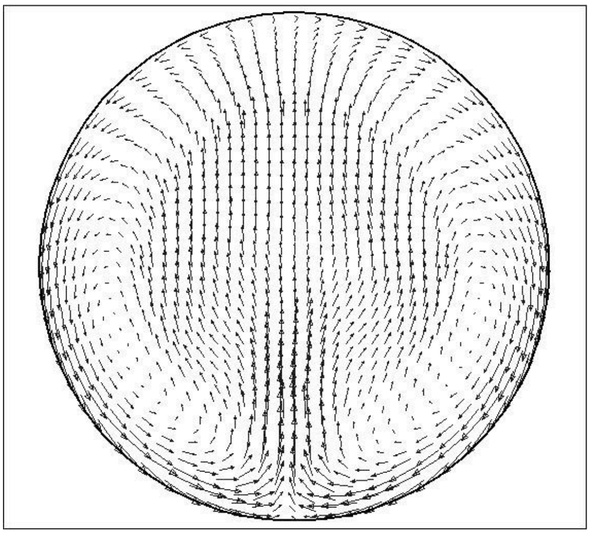

FIGURE 2.1. The counter-rotating Dean vortices.

counter rotating pair of vortices. Between φ=75° and 90° the primary flow is greatly distorted and the turbulence intensity and Reynolds stresses increases. Downstream of the bend, the distribution of primary flow velocity gradually becomes smooth and the vortices breaks down, but the effect of secondary flow remains at 10 diameters downstream of the bend. Sudo & Hibara (2000) also performed measurements on a 180° bend. The curvature radius was the same as for the 90° bend. Upstream to φ=60° the flow in the two different geometries shows similar characteristics. From φ=90° the secondary flow begins to weaken and meanders up and down in the central part of the tube. In this part of the bend, a low-velocity region exists in the middle and high velocity regions are located near the inner and outer walls.

Rutten *et al.* (2005) performed Large Eddy Simulations to investigate the turbulent flow through 90° pipe bend. The purpose of this investigation was to see how long the extension must be to avoid distortion of the flow field from the bend at the inlet boundary. The conclusion from the investigation was that an extension length of three diameters is sufficient. The computed data is validated by comparing the first and second order statistical moments with PIV measurements by Brucker (1998). Power spectra of LES and PIV velocity signals are also compared and the agreement of the numerical and experimental results is good. The computed flow field showed the counter-rotating Dean vortices, which are not of equal strength at all times and alternately dominate the flow field. This alternately domination leads to alternately clockwise and anti-clockwise rotation of the flow close to the wall in the downstream tangent.

If a pipe is turned in two bends, with the bends in orthogonal planes, a swirling motion will be generated after the second bend, which is depicted in Figure 2.2.

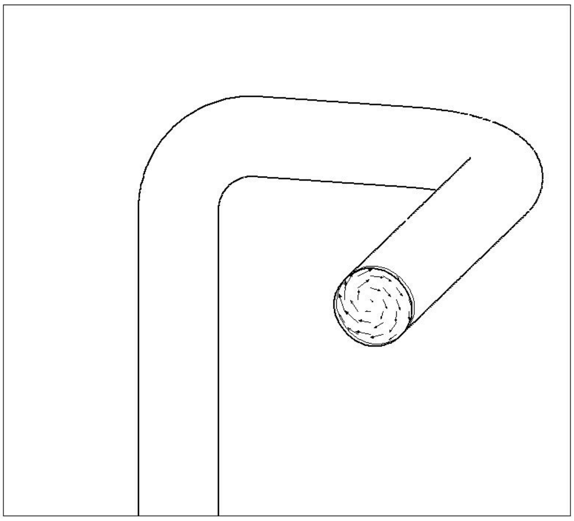

FIGURE 2.2. The swirl at the outlet of a double bent pipe.

The swirling motion at the outlet of the second bend is not an effect of the Dean vortices from the first bend; it is due to the non-uniform axial velocity distribution in radial direction at the inlet to second bend. If a non-uniform radial velocity distribution, with the maximal value rotated 90° with respect to the inner radius of the bend, is applied to the inlet to a single bend, the secondary flow consist of one vortex at the outlet of the bend. When the flow with high velocity and momentum enters the bend it is linked by the curvature to the region where the momentum is lower which induces a swirling motion. Since very few articles where found for this geometry, a numerical investigation of the pulsatile flow in a double bent pipe was performed, and the results are discussed in Chapter 5.

2.2. Internal pulsatile flow

Pulsatile flow is defined here as a flow that is composed of a steady component with a superimposed periodically varying temporal component. A special type of pulsatile flow is the oscillating flow, which is only consists of the time varying component, and hence the periodically time-averaged velocity is zero. The behavior of oscillating or pulsatile flow depends on the balance between the viscous effect and the acceleration of the fluid. The relative importance of the acceleration term relative to the viscous term in the momentum equation can be expressed by the Womersley number, defined as:

$$\alpha = r \cdot \sqrt{\frac{2\pi \cdot f}{\upsilon}} \tag{2.1}$$

where r is the pipe radius, f the frequency and υ is the kinematic viscosity. A small value of the Womersley number implies that the effects of unsteadiness are less important as compared to viscous effects. For low Womersley number (α <1), the velocity behaves almost as being a quasi-steady flow which is in phase with the pressure gradient. As the Womersley number increases, the velocity starts to show a phase lag with respect to the pressure gradient, see for example Dec *et al.* (1991) and Ramaprian & Tu (1983). For pure oscillating very low Reynolds number flow the phase lag is 90° and for turbulent flow the phase lag is less than 90° according to Ramaprian & Tu (1983). For pure oscillating very low Reynolds number flow, the $\frac{\partial}{\partial t}$-term in the momentum equation (4.2) is balanced by the $\frac{\partial p}{\partial x_i}$-term. This can be showed by assuming one-dimensional oscillating flow and that the pressure gradient is described by $\frac{\partial p}{\partial x} = \hat{p} \cdot e^{i\omega t}$ where $\hat{p}$ is a constant and ω is the frequency of the oscillation. When this is inserted into the momentum equation (4.2) and solved for U, the following result is obtained: $U = -\frac{i\hat{p}}{\omega} \cdot e^{i\omega t}$. As can be seen, the phase shift between the velocity and the pressure is 90°.

For pulsatile turbulent flow, the time derivate term will be balanced both by the pressure gradient term and remaining terms in the momentum equations, including the Reynolds-stresses. Flow pulsations also affect the axial velocity profile in the pipe. The phase shift between the pressure and the bulk velocity gives overshoots in boundary layer which depends on that the flow in the region near the wall has lower momentum than the bulk flow, and therefore, it is more sensitive to changes in the axial pressure gradient. This effect increases with increasing frequency due to the inertia effect. Ramaprian & Tu (1983) carried out an experimental study of turbulent oscillatory flow in a long circular pipe. The oscillating frequencies correspond to a Womersley number of approximately 43 and 116, respectively. They compared the results with theoretical results for laminar oscillating pipe flow at the same frequency. The laminar flow shows sharper peaks of the overshoots in the boundary layer than the turbulent flow. Also, the peaks occur closer to wall for the laminar case. The experiments also show that the phase lag between pressure and velocity is smaller for turbulent flow than for the laminar flow. Dec *et al.* (1991) investigated a cyclic oscillating velocity field in a tail pipe of a pulse combustor using Laser Doppler Velocimetry (LDV). The oscillating frequencies varied from 67 to 101 Hz and the amplitude was up to 5 times the mean velocity. The mean Reynolds number, based on the bulk flow velocity and pipe diameter, was 3750. The turbulent flow shows a similar behavior to the theoretical laminar oscillating pipe flow, with a phase shift between the pressure and the velocity and velocity overshoots near the wall; the flow near the wall reverses earlier than the flow in the core region. The laminar flow solution also shows sharper overshoots relative to the core region profile, while the turbulent flow has a smoother axial velocity profile. According to Dec *et al.* (1991), the additional momentum transport in the turbulent flow dissipates the effects of the oscillations near the pipe walls. The turbulence intensity is uniform across the core region of the flow, but the behavior in the boundary layer has two different modes. When the streamwise pressure gradient is adverse, the turbulent intensity increases from the core to a maximum in the boundary layer and then going to zero at the wall. When the pressure gradient is favorable, the turbulent intensity drops from the core value throughout the boundary layer. The turbulent intensity also shows a maximum at times of zero-velocity crossings. From the measured velocity profiles, the instantaneous wall shear stresses were calculated. A trend of increasing cycle-averaged wall shear stress with increasing pulsation amplitude can be noted but no dependence on the frequency was found. The cycle-averaged wall shear stress is slightly greater than the wall shear stress predicted for steady turbulent flow at the same averaged mean Reynolds number.

For laminar pulsatile flow in a bent pipe, the secondary flow changes rotational direction from being outward to inward in the center when Reynolds number is increased for a certain Womersley number. Hamakiotes & Berger (1988) showed using numerical computations, that the Dean vortices do change rotation direction when Re exceeds 300. The Womersley number was 15 and curvature ratio was 1/7. The reversed vortices are called the Lyne vortices. Lyne (1970) showed analytically that the fluid is driven along the wall from the outer side to inner side under action of the pressure gradient in the same manner as for the Dean vortices. However, the pressure gradient in the boundary layer is not balanced by the centrifugal forces, and at the edge of the boundary layer, the flow returns centrifugally within in the boundary layer, and drags the fluid in the interior around in a pair of vortices, that are counter-rotating compared to the Dean vortex.

It may be expected that the heat transfer to or from a flow in a pipe should depend on the pulsation frequency, since the pulsations will affect the boundary layer. Both increase and decrease of the Nusselt number in pulsating flow has been reported in the literature for different pulsation frequencies, amplitudes and mean Reynolds numbers. The Nusselt number is defined as the ratio between the convective and conductive heat transfer:

$$Nu_L = \frac{h_{coef} \cdot L}{k_f} \tag{2.2}$$

h_{coef} is the heat-transfer coefficient, L is a characteristic length scale and k_f is the thermal conductivity. Wang & Zhang (2005) performed numerical computations of turbulent pulsatile flow in a straight pipe with U_{osc}/U_{mean}=3, where the Womersley number was varied from 40 to 60. The results showed that the axial pressure gradient has a phase lag of about 90° to the velocity. The results also showed that the instantaneous velocity profile was flat at the center of the pipe. In the region between the core region and the wall a velocity overshoot occurred at some instants. These overshoots had a velocity that was larger than the velocity in the core region, and more heat was transported at these instances. The thermal boundary layer thickness varied with the pulsation of the flow and was during a period, sometimes thinner and sometimes thicker than in a corresponding steady state flow case. The local Nusselt number was, for different Womersley numbers, higher than it was for the corresponding steady case. This then implies that the heat transfer was greatly enhanced by the pulsatile flow, especially in the entrance region. Wang and Zhang also showed that the local instantaneous Nusselt number had its maximum when the velocity reached its peak value and the Nusselt number reached its lowest value when the velocity was zero. The heat transfer was also enhanced when the velocity amplitude of the pulse was increased. The results from Dec & Keller (1989) experiments with a pulse combustor fitted with a tail-pipe showed that the Nusselt number in oscillating flow was significantly higher than for steady flow with the same mean Reynolds number. The experiments also showed that the Nusselt number increased with increasing frequency and pulsation amplitude. Habib *et al.* (2004) studied pulsatile pipe flow in a range of Re of $8\ 000 < \mathrm{Re} < 50\ 000$ and both enhancement and reduction in mean Nusselt number was reported. The Nusselt number decreased for low pulsating frequency. The maximum mean Nusselt number was obtained when the pulsating frequency was in the vicinity of the turbulent bursting frequency. At this pulsating frequency, the interaction of the pulsations and the turbulent bursting increased the heat transfer, and hence the Nusselt number increased. These phenomena can be explained by the turbulent bursting model, which states that the viscous sublayer is unstable, and due to turbulent structures, its growth and destruction occur periodically.

These different effects, such as the phase lag and increased heat transfer in pulsatile flow, will affect the performance of the radial turbine working under pulsatile flow conditions. The phase shift will imply that the static and dynamic pressure will be out of phase, which can affect the shaft power of the turbine. The pulsatile flow also increases the losses; for example the heat-losses to the ambient. The losses due to viscous effects will probably also increase, due stronger shear layers. This will most probably imply that the turbine cannot be treated as being a quasi-stationary flow device.

CHAPTER 3

Turbochargers, with focus on the turbine

Turbochargers can be used in many different applications, but they are all based on the same principle; a turbine part that utilities the energy from the hot gas that flows through the turbine which then drives a compressor which will increase the density of the gas. The bearings support the shaft, and shaft seals are also required to separate the compressed air and the exhaust gases from the bearing lubrication system. Turbochargers can be found on different types of internal combustion (IC) engines, from small four-stroke automotive engines to large two-stroke marine diesel engines. For small internal combustion engines, radial turbines are the most common type. Axial turbines are sometimes used for large IC engines in marine and power generation applications. The rotational speed of the turbine is normally limited by the requirements of the compressor and the maximum radius for a given rotational speed is limited by structural reasons. This means, for turbines that normally are used for small IC engines, that the radius of the turbine wheel must be small. For small axial turbines, this gives an unfavorable aspect ratio which will give rise to secondary flows and tip leakages which will result in poor efficiency. Since axial turbines also are more complicated and more expensive compared with radial turbines, the most common type of turbines for small IC engines is the radial type. Radial turbines can also deliver a larger specific power than an equivalent axial turbine.

3.1. Performance parameters

The fundamental parameters for turbines that define the performance are the mass flow, the pressure ratio, the rotational speed, the efficiency and the shaft power output. The most important quantities for the turbine are the shaft power and the efficiency. The shaft power, P_S, is defined here as

$$P_S = \bar{T}_{Shaft} \cdot \bar{\omega} \tag{3.1}$$

where $\bar{\omega}$ is the angular velocity and $\bar{T}_{Shaft}$ is the shaft torque.

Commonly one defines the efficiency η_{is} as the ratio of shaft power to the maximal isentropic power of the driving gas flow:

$$\eta_{is} = \frac{P_S}{\dot{m} \cdot c_p \cdot T_{01} \cdot (1 - \frac{p_2}{p_{01}}^{\frac{\gamma-1}{\gamma}})} \tag{3.2}$$

where $\dot{m}$ is the mass flow, T_{01} and p_{01} is the total gas temperature and pressure before the turbine and p_2 is the static pressure downstream of the turbine. c_p is the specific heat and γ is the specific heat ratio. This definition works well for non-pulsatile flow and for pulsatile flow at low frequencies. For higher frequencies, the non-constant phase shift between the mass flow, pressure and shaft torque makes it impossible to define an isentropic efficiency in a proper way.

The fundamental parameters can either be predicted by using analytic or semi-analytic models or by testing the turbocharger under controlled conditions. The fundamental parameters are often non-dimensionalized, see Table 1, to take account for the inlet conditions and are often reported in compressor and turbine maps. Since the diameter, D for a particular turbine is constant, it can be dropped. The turbines are also tested with the actual working gas, and hence, the gas constant R and γ can also be dropped. By doing so, the quasi-non dimensional parameters are obtained. The performance can also be reported as the referred parameters, which have the same units as the fundamental parameters. In the referred parameters, the inlet pressure and temperature are referred to reference values. It is common to assume that the referred parameters can be used for different inlet temperatures, but Serrano *et al.* (2007) conducted an experimental investigation where they assess how the inlet temperature of the turbine affected the turbine performance. They measured the performance for two different inlet temperature conditions, 525 °K and 825 °K, and the results showed that for the higher inlet temperature, the efficiency was 2 point higher, for the same corrected mass flow rate, rotational speed and pressure ratio, even though the heat transfer is higher for the hot case. The heat losses should decrease the efficiency, but on the other hand, heat transfer to the compressor will over-predict the delivered shaft power, since the heat transfer increases the outlet temperature of the turbine. The authors also claims that a higher temperature also implies that the oil temperature might be higher, which will give a lower viscosity and lower losses in the bearing. A higher temperature will also give a difference in the absolute pressure, which affects where the operational point is located in the h-s diagram. This then implies that for the hot conditions the enthalpy drop is higher for a given entropy increment, resulting in a higher isentropic efficiency. Serrano *et al.* (2007) did not discuss the influence of Mach number, which might affect the efficiency, since the transonic flows introduces additional losses due to shocks.

TABLE 1. Dimensional and non-dimensional parameters as defined by Baines (2005)

	Fundamental parameters	Non dimensional parameters	Quasi-non dimensional parameters	Referred parameters
Mass flow	$\dot{m}$	$\frac{m\sqrt{RT_0/\gamma}}{p_0 D^2}$	$\frac{m\sqrt{T_0}}{p_0}$	$\frac{m\sqrt{T_0/T_{ref}}}{p_0/p_{ref}}$
Pressure ratio	PR	PR	PR	PR
Rot. speed	N	$\frac{N \cdot D}{\sqrt{\gamma \cdot R \cdot T_0}}$	$\frac{N}{\sqrt{T_0}}$	$\frac{N}{\sqrt{T_0/T_{ref}}}$
Efficiency	η	η	η	η

The performance of a turbine is tested in gas stand where the turbine is driven by gas from an external compressor. The measurement can be performed both with cold and hot gas. In the later case, fuel is injected and burnt in a combustion chamber upstream of the turbine. Since the rotational speed is very high, it is very hard to directly measure the shaft power output of the turbine. Therefore, the compressor is throttled to control the load on the turbine, and by measuring the shaft speed, the inlet and outlet pressure, temperature and the mass flow through the turbine and the compressor, respectively, the efficiency of the turbine can be computed. This efficiency is the mechanical efficiency, since the bearing losses are included. The mechanical efficiency can be divided into two parts, the aero-dynamical efficiency of the turbine η_{aero} and the bearing efficiency, $\eta_{Bearing}$;

$$\eta_{mech} = \eta_{aero} \cdot \eta_{Bearing} \tag{3.3}$$

If the bearing losses are known, the aerodynamic efficiency of the turbine can be computed. The bearing losses can be estimated from known bearing characteristics or by measuring the bearing losses in a special rig, but so far the uncertainty in the measured data and thereby also in the estimation of the bearing losses, is high. This will make it difficult to compare the computed efficiency against measured data, since the computed efficiency is the aerodynamically efficiency while the efficiency based on measurements includes the bearing losses. Also, Shaaban & Seume (2006), showed that the heat transfer from the turbine to the compressor affect the measured isentropic efficiency, since the heat transfer from the turbine to the compressor increases the outlet temperature of the compressed gas. This then gives an over prediction of the shaft power, since the shaft power is computed from the temperature raise over the compressor.

3.2. The stator

The radial turbine comprise of two essential parts, the stator and the rotor. The stator takes the flow from the exhaust manifold of the engine, accelerates and distributes it around the periphery of the rotor. The stator itself consists of a volute and in some cases a nozzle. The design of the volute is critical, since it determines the inlet flow conditions to the nozzle and the rotor. The design of the volute can be done with design methods based on 1-D flow analysis to fully 3-D methods (Chen (2009)).

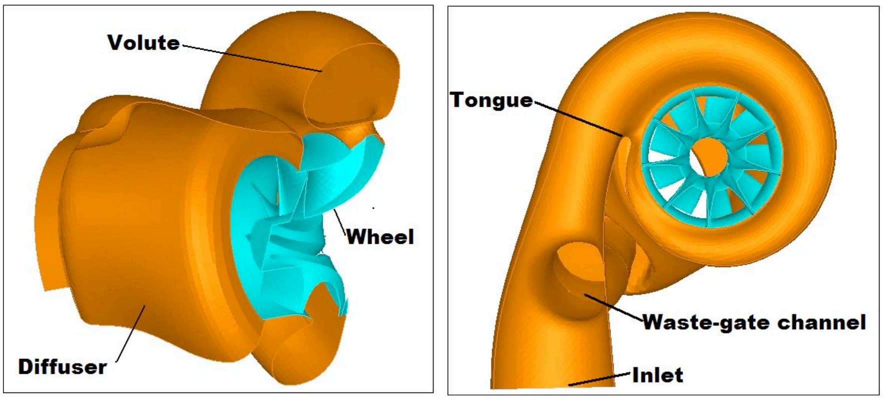

FIGURE 3.1. The different parts of a nozzle-less single scroll turbine.

The volute can be of a single or a multiple entry type. For automotive turbochargers, the single entry turbine is so far the most common type. A single entry volute is shown in Figure 3.1. Twin entry turbines, with a meridional divider, see Figure 3.2, are used on commercial diesel engines, but also for smaller automotive engines. The advantage of this type of system is that exhaust manifold can be divided, resulting in a better scavenge process due to less interference between the various cylinders, which give less rest gases in the cylinders. A multiple entry volute can also be divided in the circumferential direction, c.f. Copeland *et al.* (2009).

A single entry turbine has higher swallowing capacity, and therefore lower pressure ratio for a given mass flow and the pumping losses of the engine will be lower. However, by using a twin-entry turbine, a higher turbine pressure ratio can be reached in a shorter time and better utilization of the energy in the pulse, which improve the transient response of the engine. The drawback is that the twin-entry turbine has lower efficiency compared to single entry turbine, which has been showed by Capobianco & Gambarotta (1993). They measured the performance of a twin-entry turbine working under non-pulsatile and pulsatile flow conditions and compared the performance with an equivalent single entry turbine, and the efficiency was up to 5% lower for the twin-entry turbine for the non-pulsatile cases. Capobianco and Gambretta concluded that the lower efficiency was due to losses over the dividing tongue and losses in the shear layer between the flows leaving each entry. Yeo & Baines (1990) measured the shaft power for a twin entry turbine for different mass flow ratios in the two different entries, and computed the isentropic efficiency. The conclusion was that the lowest efficiency occurred when one of the two entries was fully closed, due to unfavorable incidence angle of the flow into the wheel. The incidence angle also varied in the axial direction at the inlet to wheel for this flow case, while the incidence angle was fairly constant in axial direction for equal mass flow in the two entries.

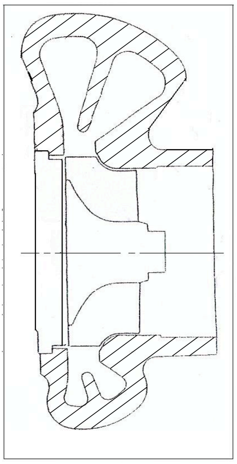

FIGURE 3.2. The volute for a twin-scroll turbine.

For turbines that are required to operate at high expansions ratios or high specific work output, a nozzle with vanes is required to turn the fluid, since a volute with nozzles will have better efficiency than a nozzle-less volute at these flow conditions. The nozzle, which is located between the volute and the wheel, consists of an annular ring of vanes which set the incidence angle of the working gas to the rotor and, in conjugate with the volute, further accelerate the fluid.

This implies that for a given flow capacity the volute with a nozzle can be smaller for a given acceleration and turning of the fluid. Nozzle-less volutes have the advantage to be simpler and cheaper, but the disadvantage that the relative inlet angle to wheel will not be uniform around the wheel, leading to deterioration of the efficiency due to increased incidence losses according to Winterbone *et al.* (1991). According to Simpson *et al.* (2009*a*) the non-uniformity of the flow field for vane-less volute is prominent just downstream of the tongue. For the vaned stator, the flow into the rotor was dominated by the jets and the wakes from each vane passage and vanes, respectively and those flow regions where only partially mixed in the inlet region to the wheel according to Simpson *et al.* (2009*b*).

Spence *et al.* (2007) conducted an experimental investigation to assess the differences in performance for vaned and vane-less volutes. They used three vane-less and three vaned volutes and for all the tested volutes, the same turbine wheel and diffuser was used. For each vane-less volute, which was designed for a specific pressure ratio, a corresponding volute with vanes was designed. They tested the different designs in non-pulsatile flow for pressure ratios over the turbine from 1.2 to 3.6, and the results show that the vane-less stators gave the best efficiency at all tested operation points; at the design points the efficiency advantage was between 2% and 3.5%.

For spark ignition (SI) engines designed for passenger cars, the wide operating range of the IC engine implies that the turbocharger is matched for a relative low engine speed and to limit the pressure ratio over the turbine at high engine speeds, parts of the exhaust gases are by-passed the turbine wheel by opening the waste-gate valve. This also limits the shaft power developed by the turbine, and hence, limiting the pressure at the inlet to the IC engine. A more advanced way to extend the operating range of the turbine is to use a variable turbine (VT). This can be done in two ways; one is to change the geometry of the volute (Variable Geometry Turbine, VGT) and the other approach is to use a variable nozzle (Variable Nozzle Turbine, VNT). Until recently, VNT have only been used for small and medium sized diesel engines, since a variable turbine can be used to get the correct pressure ratio between the air inlet system and the exhaust system to enable the use of an Exhaust Gas Recirculation (EGR) system. EGR is a key technology to reduce the NO_x-emissions of a diesel engine. For SI engines, the high exhaust temperature has limited variable turbines so far due to thermal expansion and durability, but at later years, variable turbines are also available for SI engines. There are different mechanical designs to change the geometry of the volute. One is to use a moveable sidewall of the volute to change the geometry of the volute, see for example Chapple *et al.* (1980). Since this mechanical design has some problems there are very few or no radial turbines based on this design available for automotive applications on the market. Other ways of changing the geometry is to use a flap valve at the tongue of the turbine, which will control the swallowing capacity of the turbine. A flap valve can also be used to direct the flow to either an outer larger scroll or to an inner smaller scroll as shown in Figure 3.3.

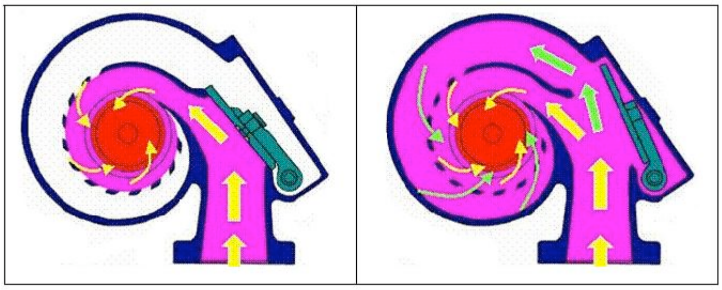

FIGURE 3.3. A Variable Geometry Turbine concept, from Andersen *et al.* (2006).

Another way to extend the operation range is to change the geometry of the nozzle. A moveable wall can be used to change the area of the nozzle. Rogo *et al.* (1986) investigated several moveable wall variations for a turbine with nozzles and concluded that a moveable sidewall is a viable design. The drawback with this design is that the moveable wall introduces losses due to leakage at the movable wall. The nozzle area can also be changed by pivoting the vanes in the nozzle, see Figure 3.4. The VNT turbine investigated by Capobianco & Gambarotta (1992) was of this type, and the comparison of the non-pulsatile performance for a VNT and a VGT turbine showed that the peak efficiency was lower for VT compared to a fixed turbine. This is most likely due to losses that the variable geometry systems induce due to leakage, wake losses behind the guiding vanes, separation, shocks and incidence losses, according to Capobianco & Gambarotta (1992) and Fukaya *et al.* (2000). But, the variable turbines showed better efficiency over a wider range, and of the two tested variable turbines, the VNT had the best efficiency. Andersen *et al.* (2006) investigated the performance of five different VNT and one VGT with the approximately same swallowing capacity, and they concluded that the VGT turbine is the most suitable variable turbine type for spark ignition engines. Some of the VNT had better efficiency at lower mass flow rates, but the VGT turbine had the best performance at high mass flow rates. They also investigated the cold start emissions for all the tested variable turbines, and they concluded that a VT most likely requires better exhaust after-treatment system than a fixed single scroll turbine. The reason for the poor cold start

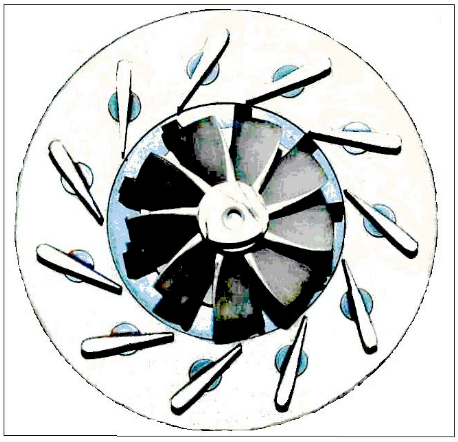

FIGURE 3.4. The variable vanes in nozzle for Variable Nozzle Turbine, from Andersen *et al.* (2006).

emissions is the larger mass and heat-transfer area. Due to lower efficiency at low mass flow rates compared to a fixed geometry turbine, an IC engine with a VT will have larger pump losses at low engine rotational speeds, but this is compensated by the higher boost pressure that can be achieved by a VT at low engine rotational speeds. A VT will also give better transient performance of the engine. The turbocharger lag can also be decreased with VT which has been shown by Filipi *et al.* (2001). Despite the many advantages with variable turbines, the most common type used on IC engines for passenger cars is the nozzle-less single-entry waste-gated radial turbine due to the robust design and the relative low cost.

3.3. The rotor

The rotor design is a compromise between aerodynamic performance, durability, weight and inertia and manufacturing cost. A rotor with low weight and inertia will respond fast to changes in load, but in order to reduce the weight, the rotor must be small, which leads to high velocities and sharp curvatures, which in turn decreases the aerodynamic efficiency. A design for good efficiency requires large blade passage areas to limit the gas velocity and small curvature of the blades to avoid separation and secondary flows. The specific work output of the turbine can be expressed with the Euler turbo-machine equation:

$$W_{Shaft} = U_1 \cdot C_{\theta 1} - U_2 \cdot C_{\theta 2} \tag{3.4}$$

where C_θ is the tangential velocity component of the gas at the inlet and outlet, respectively. U_j is the blade speed, $U_j = r_j \cdot \omega$. Station 1 is located at the rotor inlet and Station 2 at the rotor outlet, see Figure 3.5. For given rotational speed and radius, the maximum work output is achieved when the inflow tangential velocity component is high and the flow leaves the rotor in the axial direction.

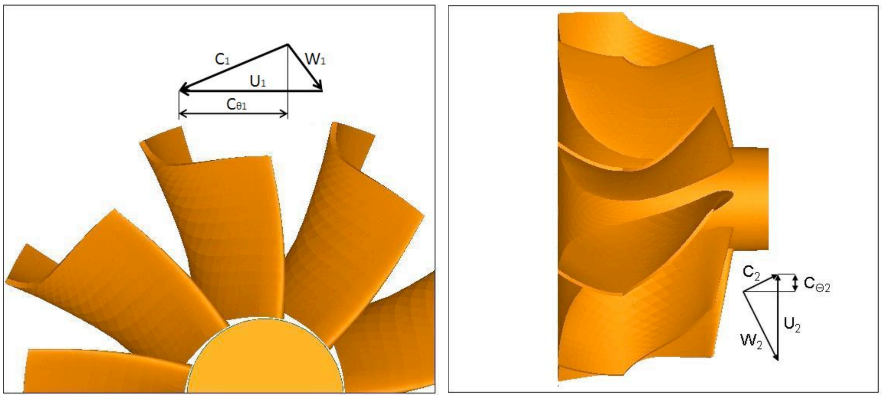

FIGURE 3.5. Rotor inlet (left) and outlet (right) velocity triangles.

A conclusion from the Euler turbo-machinery equation (3.4) is that the optimum velocity at the inlet to the rotor is a pure tangential velocity, but it has been showed that the optimum relative inlet flow angle is in the region between -40° and -20° (c.f. Baines (1996) and Moustapha *et al.* (2003)). Spence & Artt (1998) showed that a 99 mm radial turbine was reasonably tolerant to relative incidence angles between -40° to +30°. An angle of incidence is positive when the inlet velocity tends to impinge on the blade tips at the pressure side of the blade. If the flow is more or less radial, it will separate at the leading edge of the suction side, and a recirculation zone will be formed. If the inflow angle is more negative than approximately -40° the flow will separate at the leading edge of the pressure side as shown in Figure 3.6.

The efficiency will also be higher if the exit flow of the wheel have no or slightly negative swirl according to Flaxington & Swain (1999). There are very few available articles in the open literature that discuss how to optimize the design of the wheel. This might depend on the low component cost for automotive turbochargers, which imply the manufacturers use the cut-and-try techniques (Flaxington & Swain (1999)), and therefore they have large databases for different designs.

Doran *et al.* (2001) studied the effects of different shroud profiles at different operating points. In their experimental study, they used four different shroud profile radius for a 99.0 mm radial inflow nozzle turbine. The results showed that the largest shroud radius gave the best performance under most

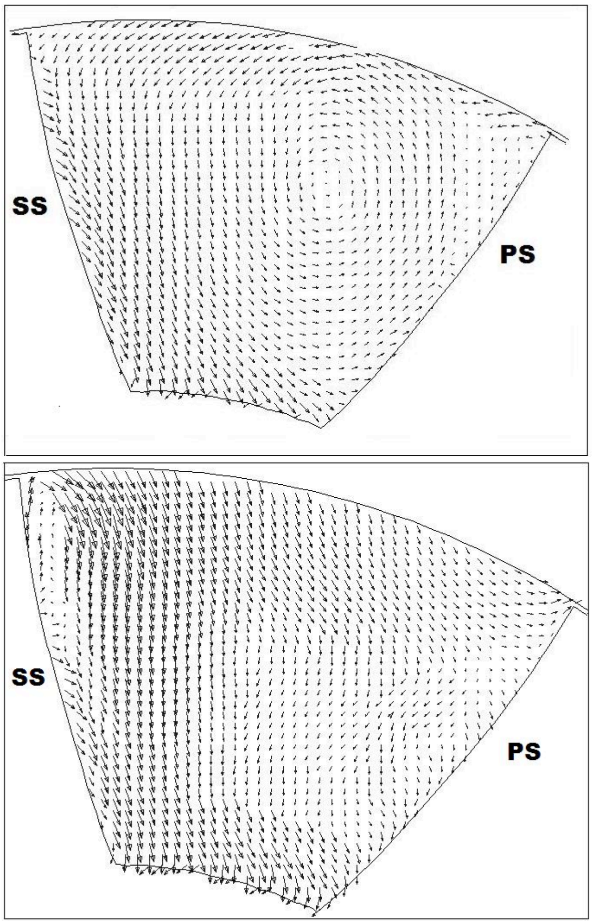

FIGURE 3.6. In-plane velocity components showing the tip vortex at the leading edge of the blade. Top figure: Relative inlet angle is approximately -65°. Bottom figure: Relative inlet angle is approximately 20°.

conditions, but at the highest rotational speed, the most shaped shroud profile gave 3.5 percent points better efficiency. They also performed one dimensional numerical analysis to examine the effect of shroud profile with respect to incidence angle. For negative incidence angles, a small radius of shroud curvature gave the best performance, while for positive inlet angles the largest radius gave the best performance. No measurements or 3-dimensional numerical computations were conducted in order to explain the effects of different shroud profiles.

Another way to increase the efficiency of the turbine is to use blades with inclined leading edges, which has for example been showed by Barr *et al.* (2006) by a numerical study for a turbine with an inlet tip diameter of 90 mm. They studied three different inclination angles; 0°, 15° and 30°. At design condition, the efficiency was almost equally, while at off-design conditions, the efficiency was improved by 2% for the 30° back sweep angle blade due to a strongly reduced tip vortex at the leading edge. The drawback of this design is that it increases the bending stresses in the blade, and therefore limits the used of back swept blades.

Futral & Holeski (1970) performed an experimental study with the objective to study the effects of tip clearance for a radial turbine. The wheel diameter was 152.9 mm, which is quite large compared to the size of the wheel of an automotive turbocharger. Tip clearance values of 0.25 to 7% of the passage height at the rotor entrance and at the rotor exit were used. The results showed that an increase of the axial tip clearance at the rotor entrance gave a decrease of the total efficiency of 0.15% for each percent increase of tip clearance. At the exit of the rotor, an increase of the radial tip clearance from 1% to 3% of the passage height gave a decrease of the efficiency of 1.6% for each percent increase of tip clearance. For the range of 3% to 7%, the decrease of efficiency was smaller, but still, larger than the effect of increasing the radial gap at the entrance. But, the tip clearance height is not the only parameter that affects the flow over the tip, and hence, the tip vortices and the losses that they introduce. Dambach & Hodson (2001) conducted an experimental investigation of the flow over the blade tip for different axial and radial tip-clearances for a radial turbine. The tip gap was varied from 0.6% to 1.2% of the local blade height. They showed that different blade tip gap height to blade width ratio gave different behavior for the tip leakage flow. If the ratio was below approximately $\frac{1}{6}$, the tip leakage flow was mixed with the boundary layer at the shroud, resulting in a tip leakage flow with low momentum, and hence, a less strong tip vortex at the suction side. If the ratio was larger than approximately $\frac{1}{6}$, the inertia effects dominated over the viscous effects, and the momentum of tip leakage flow from the pressure to suction side was higher, resulting in a stronger tip vortex. Also, they showed that the pressure difference over the gap remains relatively constant for the tested tip gap heights.

For turbines working in pulsatile flow, mixed flow turbines have some advantages compared to radial turbines. A mixed flow turbine is a turbine, with its leading edge of the blade inclined to the axial axis. This implies that the flow at the entrance to the wheel have both an axial velocity component and a radial velocity component. Mixed flow turbines is better due to less inertia and a mixed flow turbine can have non-zero blade angle and still maintain the radial fiber, which is favorable from a stress analysis point of view. Also, the less turning of the flow in the mixed flow turbine will imply that no or less separation occurs at the shroud side of the inlet region of the wheel (Rajoo & Martinez-Botas (2008)). Also, due to lower inertia, the mixed flow wheel can be designed with non-scalloped back disk, which is better from a structural point of view. The mixed flow turbine has also, regarding to Chen (2006), a generally better efficiency and swallowing capacity at high speed, which is the same as higher pressure ratio and lower U/C_s, but a lower efficiency at low speed. To overcome this drawback, the mixed flow turbine can be designed with some inlet blade angle, as already mentioned. With all this in mind, Chen (2006) designed a mixed flow turbine wheel, and when comparing the performance for this wheel with a corresponding radial turbine wheel, the result shows that the mixed wheel has better performance compared to a radial wheel and it is also lighter.

The U/C_s ratio is called the blade speed ratio, and U is the rotor tip speed and C_s defined as:

$$C_s = \sqrt{2 \cdot c_p \cdot T_{01} \cdot (1 - \frac{p_2}{p_{01}}^{\frac{\gamma-1}{\gamma}})} \tag{3.5}$$

Mixed flow turbines have the maximum efficiency at a U/C_s ratio of approximately 0.65, while a radial turbines have the best efficiency at blade speed ratio of approximately 0.7 (Chen *et al.* (1997)). The efficiency also drops substantially for U/C_s values below 0.7 for radial turbines, while mixed flow turbines can maintain high efficiency over a larger region of lower U/C_s ratios. Chou & Gribbs (1989) reported that a mixed flow turbine with twin entry volute is up 6 % better compared to a radial turbine, and on-engine test showed that a mixed flow turbine gave better over-all performance for a diesel engine compared to the same diesel engine with a radial turbine. In Watanabe *et al.* (1996), the result from a work where a mixed flow turbine is designed to obtain less inertia to improve transient response is reported. The objectives can be achieved with a smaller wheel diameter without losing efficiency, since a mixed flow turbine has a better swallowing capacity for the same diameter. Also, the inclined leading edge implies that the mixed flow turbine has better efficiency at low U/C_s. The mixed flow can also have up to 55% lower inertia compared to the radial turbine. On-engine tests with the designed mixed flow turbine show that the time to reach a boost pressure 53 kPa is reduced with 20% from 20 km/h at third gear for the mixed flow. Additional, a twin entry volute further reduced the time. Also, ball bearing system reduced the time with 9%. When combining this different enhancement, the time was reduced with approximately 40%. Chen *et al.* (2009) showed in a numerical study that an inclined leading edge for a mixed flow turbine improves the performance, and the pulse averaged efficiency was 2% higher. This general trend of higher efficiency during pulsatile flow conditions is also confirmed by Karamanis & Martines-Botas (2002). They designed and tested a mixed flow turbine, and the tested mixed flow turbine had a flatter efficiency curve when plotted versus U/C_s compared to a radial turbine. This means that the efficiency does not vary so much during an exhaust pulse, which is beneficial. Also, the tested turbine had a relative reduced sensitivity of the efficiency for different rotational speeds, and this means that the tested mixed flow turbine most probably have a better performance during pulsatile flow conditions. Palfreyman *et al.* (2002) studied the performance of four different turbine wheel geometries for a mixed flow turbine, and they concluded that a reduced chord length (with 18.75%) gave the largest deterioration of the efficiency, followed by a reduced number of blades (from 12 to 10), and then changing the inlet blade angle. The size of the gap between the blade tip and shroud also affects the efficiency, since the pressure gradient over the blade drives the flow over the tip and a jet and a tip vortex is created.

3.4. Turbine performance

As already mentioned, the flow in the exhaust system of an IC engine is highly pulsatile, and this affects the performance of the turbine. The performance of turbines working under pulsatile flow conditions has been assessed by many researches by both different numerical methods and by experiments. A typical feature of turbines working in pulsatile flow is that when plotting the mass flow versus shaft torque, as been done in Figure 3.7, the trajectory form a closed loop, enclosing the quasi-stationary trajectory. The same is valid when plotting the blade speed ratio U/C_s versus the efficiency. U/C_s varies during the pulse, since the rotational speed of the rotor is almost constant, whereas the variation of U/C_s is from low values of approximately 0.2 to high values above 1, which is far away from the optimal value of approximately 0.7.

For turbines operating under pulsatile flow conditions, the mean efficiency is lower compared to non-pulsatile flow conditions for the same mass flow and pressure ratio, but the instantaneous performance can be both higher and lower, see for example Winterbone *et al.* (1990), Winterbone *et al.* (1991), Dale & Watson (1986) and Capobianco & Gambarotta (1990). But it must be emphasized that it is very hard to compute the isentropic efficiency in an accurate way, due to the phase shift between pressure and mass flow (c.f. Hellstrom & Fuchs (2008*b*) and Ehrlich *et al.* (1997)) and the time it takes for the energy to propagate from the measuring point to the turbine wheel. It is also hard to measure the time dependent shaft power.

Winterbone *et al.* (1991) investigated the performance of a radial turbine in both non-pulsatile and pulsatile flow. The frequency of the pulsatile flow was 35 Hz. To measure the time dependent shaft power, they used a hydraulic

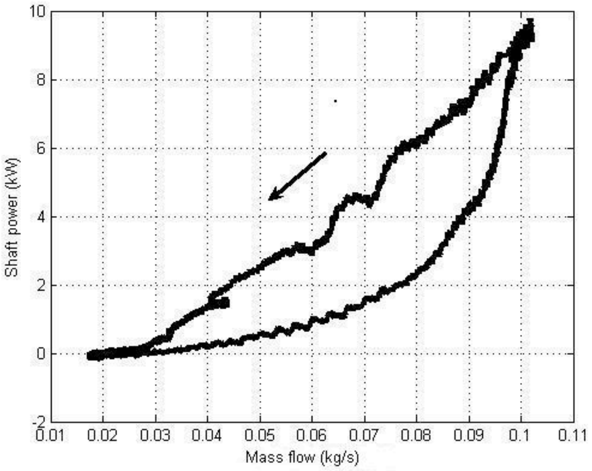

FIGURE 3.7. Computed shaft power vs. mass flow at inlet.

dynamometer in combination with the knowledge of the varying angular velocity. The time resolved shaft torque is then the sum of the mean shaft torque obtained from the hydraulic dynamometer and the product of the moment of inertia of the rotating part and the time derivate of the angular velocity. By analyzing the measured pressure distribution around the volute for both non-pulsatile and pulsatile operating conditions, they concluded that the flow in the turbine volute can be treated as being quasi-stationary, since the rate of change of pressure with respect to distance was much greater than it was with respect to time. Since the shaft torque measurements were time-resolved, they could compare them to the time resolved pressure traces at the inlet, and the phase lag between the pressure trace and the torque trace was about 40°. The time this phase lag corresponds to, is larger than the pressure wave travel time from the inlet to the rotor, and hence the phase lag do not only depend on the wave propagation time. Winterbone et al. also reported that the mass flow pulses were approximately in phase with the pressure pulses, but the mass flow trace was quite noisy, so it was hard to determine any phase shift. The rotational speed of the wheel varied with approximately 2% during the pulse. Wallace *et al.* (1969) investigated the effects of different frequencies, mass flows and turbine speeds. They used a dynamometer to measure the shaft torque of the turbine, and this dynamometer could be operated up to 100 000 rpm. The frequency of the pulsatile flow was varied from 16.7 Hz to 50 Hz, and they concluded that the turbine shaft torque first increased and then decreased with increasing frequency. The shaft power diminished slightly with increasing mass flow for constant rotational speed of the turbine wheel and mean inlet pressure to the turbine. Benson & Scrimshaw (1965) conducted experiments where the pulse frequency was varied from 30 Hz to 70 Hz, and the rotational speed of the turbine wheel was varied from 30 000 rpm to 60 000 rpm. The used turbine was a nozzled radial turbine with twin entries. The results showed also that the efficiency increased up to a pulse frequency of 60 Hz, and then decreased with further increase in pulse frequency.

Dale & Watson (1986) measured the shaft power of a twin entry turbine working in pulsatile flow. They concluded that the efficiency varied with varying admissions in the two entries, where the lowest efficiency occurred when the flow entered only one of the two entries. For an operation point with a pulse frequency of 40 Hz, the maximum deviation of the instantaneous efficiency from the quasi-stationary assumption was up to 10%, with both higher and lower values than the efficiency from the quasi-stationary assumption. Karamanis *et al.* (2001) concluded from an experimental study, that the deviation of isentropic efficiency from the quasi-stationary assumption was reduced as the pulse frequency was increased for a mixed flow turbine. The frequency of the pulsatile flow was 40 Hz and 60 Hz, respectively. When they computed the isentropic efficiency, they applied a correction for the phase lag, which corresponded to the sonic travel time from the inlet to the wheel. The cycle-averaged efficiency was lower than the corresponding steady-state efficiency, due to the large variation of flow conditions. The incidence angle varied from -80° to 40° during the pulse. Iwasaki *et al.* (1994) compared results from measurements on two different engines (a six cylinder engine with twin entry and four cylinder engine with single entry turbine) and showed that the pulsation factor, defined as the ratio of the fluctuating pressure amplitude and the mean pressure, was larger for low engine speed compared to high engine speeds, and concluded that at higher engine speed (or frequency), the turbine acts more as an steady state flow device. The same behavior has been reported in other studies, c.f. Copeland *et al.* (2009) and Capobianco & Marelli (2006).

In the experiment conducted by Arcoumanis *et al.* (1999) the steady and unsteady performance of a mixed flow turbine was investigated for different rotational speeds of the wheel and with pulse frequencies of 40 Hz and 60 Hz. The results showed that the cycle averaged isentropic efficiencies were higher for a mixed flow turbine compared to a radial turbine. By using cycle averaged efficiency, no phase shifting of the shaft torque is needed, which is beneficial, since the time-resolved isentropic efficiency is strongly affected by the size of the phase shift.

Lam *et al.* (2002) performed a time resolved 3-dimensional numerical study of the pulsatile flow in a radial nozzled turbine. They used the frozen rotor technique to model the rotation of the wheel. The results showed that instantaneous performance of the rotor under pulsatile conditions did not vary significantly from the non-pulsatile conditions, and Lam et al. concluded that the wheel can be treated as a quasi-steady device, while the volute must be treated as a non quasi-stationary flow device. Chen *et al.* (2008) performed unsteady RANS computations to assess the flow in a mixed flow turbine wheel. The volute and diffuser was not considered, only the wheel with short extension at the entrance and exit region. At the inlet, a pulsatile inlet condition was applied, while at the outlet, a in time constant pressure was specified. The results show that the instantaneous shaft power varied during the pulse and for the same mass flow rate at the inlet, the shaft power was higher during the acceleration phase compared to the same mass flow rate during the deceleration phase. This is due to that the flow field in the wheel differs significantly at these different instants. Since only the flow field in the wheel is computed, the difference in the delivered shaft power and the varying flow field indicates that the wheel cannot be treated as being a quasi-stationary flow device. But, this might be an effect of a varying inflow angle as well, and unfortunately, the inlet angle is not reported in the paper.

Palfreyman & Martinez-Botas (2005) investigated the pulsatile flow in a mixed flow turbocharger with numerical methods. They used a medium sized mixed flow nozzle-less turbine. They concluded that the used method with explicit rotation of the wheel, better captures the non quasi-stationary behavior of the turbine than the method used by Lam *et al.* (2002). But, this might also be an affect of that Palfreyman and Martinez-Botas used a nozzle-less turbine, without the damping the nozzles can introduce, leading to a more uniform flow into the rotor. At the inlet to the rotor, the incidence angle varied from $-92°$ to $+60°$, which will give raise to losses, due to strong tip vortices at the leading edge of the blades. The blade torque and the work output fluctuated substantially and with the frequency of the pulse. A perturbation with same frequency as the blade passage frequency was also superimposed on the shaft torque trace, which is an effect of the blades passing the tongue. The velocity field within the turbine wheel also varied substantially during the pulse due to poor flow guidance at the entrance to the turbine wheel. The trajectory of the mass flow versus efficiency showed a hysteresis loop, which encapsulates the quasi-steady values. This is, according to Palfreyman and Martinez-Botas, due to the imbalance between inlet and outlet mass flow during the pulse and the "filling and emptying" of the volute as the turbine acts as a restriction. They also reported a phase lag between the computed isentropic work and the actual work.

Heat losses will of course affect the performance of the turbine. The heat transfer or heat losses from the turbine can be divided into two major categories, the internal heat losses and external heat losses. The internal heat losses is the heat that is going into the bearing house, and then transferred to the oil, cooling water and some amount of the heat will go into the compressor. The external losses are the heat that is transferred to the surroundings due to convection and thermal radiation from the turbine house. Baines *et al.* (2009) assessed in an experimental work the heat transfer in turbochargers (working under non-pulsatile flow conditions) with the objective to develop a 1-D heat transfer model. They concluded that the internal losses are much greater than the external heat losses and that the heat losses are strongly dependent on the turbine inlet temperature and the Reynolds number. Romagnoli & Martinez-Botas (2009) conducted experiments on a turbocharger mounted on an IC-engine, with the objective to assess the heat transfer processes in a turbocharger and to develop a simplified 1-D heat transfer model. The measurements show that the radiated heat from the engine strongly affects the temperature distribution at the turbocharger casing, and this must be taken into account when using heat transfer models for turbochargers mounted on engines. Other investigations on heat transfer effects on the turbocharger performance, (c.f. by Shaaban & Seume (2006), Shaaban *et al.* (2006) and Bohn *et al.* (2005)) more focus on how the heat transfer from the turbine affect the performance of the compressor and how the heat transfer affects the results in 1-D simulations.

One way to increase the work output of a turbine working in pulsatile flow is to use some type of active control of the turbine. This can be done by controlling the throat inlet area to the wheel in accordance to the exhaust pulse. This improves the pressure ratio, especially at low mass flow. Pesiridis & Martinez-Botas (2006) tested a mixed flow turbine with a nozzle that was able to alter to the throat inlet area to the turbine wheel. The variable nozzle was of a sliding-wall type restrictor and it was possible to control the throat area in phase and out of phase with the incoming pulses. The actuator was an electrodynamic shaker. Tests were performed at two different frequencies of the pulsatile flow. Different phase settings between the pressure pulse and the movement of the nozzle were also tested. An increase in shaft power output with up to 7% was achieved with the active control system, but the efficiency was lower for the turbine fitted with this type of active control system. A better design is to active control the incidence angle of the vanes in a vaned nozzle. Rajoo & Martinez-Botas (2007) studied the performance of mixed flow turbines with moveable nozzle vanes. The movement of the nozzle vanes was controlled in both a passive way and in an active way with an actuator. In the passive system, an increasing pressure in the volute opened the vanes against a pre-loaded spring, and when the pressure decreased, the vanes were retracted. In this way, an increased area is obtained at high pressure, while the area is decreased at lower pressure. The passive system increased the shaft power output (with 36% for the best case) during the period of the pulse when the mass flow was low, but reduced the maximum power. The cycle averaged power was lower compared to a turbine with fixed vanes. Still the efficiency was better for the turbine with a passive control system. For the active system, with a forced movement of the vanes, a small improvement of the efficiency was achieved. The authors also concluded that of the tested control systems, a passive system with moveable nozzle vanes is probably the most beneficial system, especially for IC engines working with a narrow speed range.

Another way of improving the performance of the turbocharger is to use an electric motor to assist the turbine at operational conditions where the efficiency is low or the available energy is large enough. Panting *et al.* (2001) designed an electrically assisted turbocharger and tested it in a gas-stand and on a 1.7 l engine. The electrical motor is mounted on the shaft in between the turbine and compressor. The motor can also act as a generator and deliver electrical power at operational conditions when the waste gate vale is usually open. The system with an electrically motor increased the boost pressure at low engine speed, which enhanced the engine torque and improved the response of the engine but the drawback is that the system is complicated and bulky. Also, Panting *et al.* (2001) showed with a 1-D numerical study of a four cylinder diesel engine fitted with electrical assisted turbocharger that a reduction of the engine fuel consumption can be achieved at an engine steady state operational conditions when an electrical assisted turbocharger was used.

When computing the isentropic efficiency and U/C_s, it is common to assume that the pressure at the outlet of the turbine is constant during the pulse. This assumption can be doubted; special for small turbines with a size that is common for automotive applications. Capobianco & Marelli (2005) investigated the unsteady pulsatile flow in a four to one exhaust manifold and a nozzle-less radial turbine, and one of the conclusions was that the flow unsteadiness at the turbine outlet cannot be neglected due to the fact that the measured pressure downstream of the turbine was not constant over a pulse period. The amplitude of the pressure variations was approximately 0.3 bar, and the amplitude of the pulse at the inlet to the turbine was for this case approximately 1.0 bar. The amplitude of the pressure variations downstream of the turbine also increased when the waste-gate valve was opened, since the maximum pressure before the turbine was higher, due to an increased mass flow through the system. Capobianco & Gambarotta (1990) also studied the effects of different waste-gate valve opening areas on the pressure pulses upstream and downstream of the turbine, and the results showed that the pressure pulses at the turbine inlet were unaffected by the waste-gate valve opening, while the pressure at the outlet of the turbine had a high frequency oscillation superimposed. The frequency was about 3 kHz, but since neither the blade number nor the rotational speed of the wheel was specified in the report, no conclusion of the source can be made. Benson (1974) also noticed pressure fluctuations downstream of the turbine diffuser for pulsatile inlet conditions. He also concluded that the non-steady performance of the turbine deviates from the quasi-steady assumption. He based his result on measurements of the turbine performance from both non-pulsatile and pulsatile inlet conditions.

The only time resolved three-dimensional numerical investigation of the flow field and the performance of radial turbines working at rotational speeds that are common for small automotive IC engines that has been found in the available literature has been performed by Lam *et al.* (2002). In their study, they used time resolved three-dimensional numerical computations to investigate the performance of a nozzled radial turbine with a rotor tip diameter of 47.04 mm. They only investigated one operational point, where the frequency of the pulsatile inlet flow corresponded to engine speed of 1600 rpm and the turbine rotational speed was set to 136 000 rpm. The tip gaps between the blades and the shroud was neglected, which of course affects the accuracy of the results. They also used the "frozen rotor" wheel modeling approach, which imply that blade passage effects are not taken into account.

No investigations of the influence of different frequencies, amplitudes and perturbations on the time-resolved three-dimensional flow field and the performance of radial turbines working at rotational speed in the range of approximately 80 000-300 000 rpm has been found. Therefore, numerical studies has been performed to investigate the effects of different frequencies, inflow conditions and amplitudes of the pulsatile flow at the turbine inlet. The results from the time-resolved three-dimensional computations have been analyzed with focus on the turbine performance and the flow field. For some of these computations, the secondary flow at the inlet was neglected. To assess the effects of secondary flow at the inlet, a numerical study has also been performed with different perturbations applied at the inlet to the turbine. Also, one case where an exhaust manifold is situated upstream of the turbine is considered. The effects of external heat-transfer at the turbine housing on the turbine performance have also been assessed. The different cases and the results are presented in Chapter 5.

CHAPTER 4

Methods

This chapter will start with a very brief overview of the governing equations; the continuity equation, the momentum equation and the energy equation. These equations form a model of the compressible flow of gases. These equations are non-linear, and there exist only a few laminar flow cases where these equations can be solved analytically. Additionally, turbulent flows imply that additional modeling is needed. Hence, one has to use numerical techniques to solve the governing equations. The most relevant methods that have been used in this thesis are also briefly discussed in this chapter.

4.1. Governing equations

The governing equations that describe the conservation of mass (4.1), momentum (4.2) and energy (4.3) are the Navier-Stokes (NS) equations and the energy equation complemented with the equation of state (4.4):

$$\frac{\partial \rho}{\partial t} + \frac{\partial}{\partial x_j}(\rho u_j) = 0 \tag{4.1}$$

$$\frac{\partial}{\partial t}(\rho u_i) + \frac{\partial}{\partial x_j}(\rho u_i u_j) = -\frac{\partial p}{\partial x_i} + \frac{\partial \tau_{ij}}{\partial x_j} + \rho f_i \tag{4.2}$$

$$\frac{\partial}{\partial t}(\rho h) + \frac{\partial}{\partial x_j}(\rho u_j h) = \frac{\partial p}{\partial t} + u_j \frac{\partial p}{\partial x_j} + \tau_{ij}\frac{\partial u_i}{\partial x_j} - \frac{\partial q_j}{\partial x_j} + W_{ext} + q_H \tag{4.3}$$

$$p = \rho\, TR \tag{4.4}$$

where ρ is the density, p the pressure, T the temperature, x_i the Cartesian coordinate in the i-direction, t the time, $\mathbf{U} = u_i$, i=1,3 is the velocity component in the i-direction, f_i the specific force, τ_{ij} is the viscous shear stress tensor, h is the specific enthalpy, defined as $h = c_p T$, R is the gas constant and q_i is the heat flux. W_{ext} is the work of external volume forces and q_H is the heat source. The heat flux q_i is modeled through Fourier's law. The viscous shear stress tensor, τ_{ij} is defined as:

$$\tau_{ij} = \mu(\frac{\partial u_i}{\partial x_j} + \frac{\partial u_j}{\partial x_i} - \frac{2}{3}\delta_{ij}\frac{\partial u_k}{\partial x_k}) \tag{4.5}$$

4.2. Turbulence

When the flow reach above a certain Reynolds number the laminar flow becomes turbulent. The Reynolds number is defined as

$$Re = \frac{U \cdot L}{\upsilon} \tag{4.6}$$

where U is a characteristic velocity, L is a characteristic length and υ is the kinematic viscosity. Reynolds number is a dimensionless number that describes the ratio between the inertial forces and the viscous forces. This means that for low Re-number, the viscous forces dominate over the inertial forces, whereas for high Re-flows the situation is the opposite. For pipe flows, the characteristic velocity is the bulk velocity and a typical length scale is the pipe diameter. With these characteristic quantities, a laminar pipe flow will become turbulent when the Re-number exceeds a certain value which depends on the particular set-up (such as perturbations, wall friction). Experimentally, one could show that the flow can become turbulent already at Re about 2000 or larger, c.f. Carpinlioglu & Gundogdu (2001). Flows with Re-number larger than the critical Re-number, do not necessarily imply that it is a fully developed turbulent flow. Turbulent flows are characterized by being time dependent, 3-dimensional and chaotic where the flow at each location can be described by a mean velocity and a fluctuating part. Since the fluctuating part is irregular, only statistical methods can be used to characterize and quantify the flow properties. Another feature of turbulent flow is that the viscous forces dissipate the turbulent kinetic energy into heat. The turbulent flow consists of eddies with different length scales, where the largest eddies are the most energetic ones. The large eddies have velocity and length scales of the same order as the mean flow. The large eddies extract energy from the mean flow and in average transfer their energy into smaller eddies. These smaller eddies in turn drive even smaller eddies, until the scales of the smallest one is such that viscous dissipation becomes dominant. In this way, energy is transferred from the larger scales to the smaller scales. Small eddies, not too close to the boundary, are by nature independent of the boundary conditions and therefore have a universal and isotropic character. The larger eddies are characterized by the particular flow and these eddies carry most of the turbulent kinetic energy. In the range between the energy bearing eddies and the small eddies, in the dissipative range, one finds a range of eddies (scales) that are dependent only of inertia and therefore one talks about the inertial subrange. The dominating part of turbulence production takes place in the energy containing range where the mean velocity gradients are not small, while almost all dissipation occurs in the dissipation range. The transfer of energy from larger to smaller scales occurs mainly in the inertial subrange.

4.3. Numerical methods

Since the NS equations are non-linear, no general analytic solution exists; instead, numerical techniques can be used. By using a discretization practice, the NS equations are approximated by a system of non-linear algebraic equations which than can be solved numerically. There are three main discretization methods that are used for fluid problems; the finite difference (FD) method, the finite element (FE) method and the finite volume method (FV). All these discretization schemes employ local polynomials for approximating the dependent variables. For detailed calculations of transitional and low-Re turbulent flows one may also use spectral methods where global ortho-normal functions are used to approximate the dependent variables. The advantage of local polynomials is that one obtains sparse matrices to solve whereas spectral methods have better asymptotic (exponential) convergence rate. In all numerical studies presented in this thesis, a commercial general CFD solver (STAR-CD ver. 3.26) has been used. This code is based on the FV methods.

For temporal discretization, two different schemes have been used, a first order implicit scheme and the Crank-Nicholson scheme. The implicit scheme has in principle no restrictions on the time step δt, but it must be small enough so as to resolve the fluctuations and additionally to limit the temporal approximation errors. The Crank-Nicholson scheme is of formal second order accuracy, but as for all central second-orders schemes, it is liable to introducing non-physical oscillations when the viscous smallest scales are not fully resolved. The Crank-Nicholson scheme can be blended with an implicit scheme. This implies a reduction in the formal order of accuracy of the numerical scheme but with the gain of enhanced stability. When determining the size of the time step it is important to consider the coupling to the spatial discretization and the speed which the information is propagating with (i.e. the local physical properties of the flow). This means that time step must be small enough to ensure that information cannot propagate no more than over a computational cell δx during a time step δt. This condition allows the numerical scheme to track the propagation of physical information and it is expressed in numerical analysis in form of the Courant number and the Courant Friedrichs Lewy (CFL) conditions that states that the Courant number must be less than 1:

$$CFL = \frac{|U|\,\delta t}{\delta x} \leq 1 \tag{4.7}$$

where $U = u \pm c$ is the physical propagation speed, with c being the speed of sound and u the convection velocity.

For the approximation of the spatial discretization of the convection terms, different schemes are available in the used code. Three of them have been used, the first order Upwind Differencing (UD) scheme, the formal second order Monotone Advection and Reconstruction Scheme (MARS) and a blended Central Differencing (CD) scheme. The UD scheme is known to preserve the physical bounds of the fluxes, but can in many cases lead to excessive numerical diffusion. A second order scheme will better preserve steep gradients, but can also introduce non-physical oscillations (alike the Gibbs phenomenon). Additionally, all numerical schemes may be dispersive in the sense that the numerical propagation speed of waves is frequency dependent. The MARS scheme employs a Total Variation Diminishing (TVD) scheme, making it particularly well suited to capture the strong gradients, without overshoots. Such strong gradients are expected for the flows that we consider both in the turbine and the compressor. Since the MARS scheme is proprietary to CD-adapco, no details of the scheme can be found in the open literature. According to CD-adapco (2005) this scheme is the scheme that is least sensitive to solution accuracy to mesh structure and skewness of the available schemes in the used code. Since the details of the scheme are not known, extensive tests have been made to assess its accuracy for problems of relevance to engine flows.

A modified version of the Pressure-Implicit with Splitting of Operators (PISO) method proposed in Issa (1986), Issa *et al.* (1986) and Issa *et al.* (1991) is implemented in the used code to solve the discretized governing equations at each time step. One of the major differences as compared to the standard PISO scheme is that the number of corrector stages is not limited to two, as being proposed in the original version; instead, the number of corrector stages is determined by the splitting error, which according to CD-adapco (2005), increases the accuracy and reliability of the method.

4.3.1. *Turbulence modeling*

To resolve all scales of the turbulent flow the grid size and the time step must be smaller than the smallest length and time scale of the flow. This can be done by fully resolved simulations, Direct Numerical Simulation (DNS), and in general, the computation cost is proportional to Re^3. This approach is not feasible for the applications studied in this work, since the required computational resources are not available yet. Instead, the governing equations can be handled by two other methods, the Reynolds Averaged Navier Stokes (RANS) approach and the Large Eddy Simulation (LES) approach. In the RANS approach, the governing equations are expressed in terms of the mean quantities. The base line of the RANS equations is that the instantaneous flow field can be divided into a time averaged part and a fluctuating part. With this inserted in the governing equations and averaged over time, the RANS equations are obtained, which describes the time averaged flow field. Due to the non-linearity of the NS equations, additional terms appear in the RANS equations; the Reynolds stresses, $\bar{u'_i u'_j}$. These terms represent the effect of the fluctuations on the mean field. The Reynolds stresses cannot be expressed analytically in terms of the mean variables and hence they have to be modeled in order to close the equations. Turbulence models can be divided in several major categories, such as Eddy viscosity models and Reynolds stress based models. The eddy viscosity models are based on the turbulent-viscosity hypothesis which relates the Reynolds stresses to the mean velocity field as:

$$\bar{u'_i u'_j} = \frac{2}{3}k\delta_{ij} - \upsilon_T \left(\frac{\partial U_i}{\partial x_j} + \frac{\partial U_j}{\partial x_i} \right) \tag{4.8}$$

where k is the turbulent kinetic energy and U_i is the mean flow velocity components. To close this equation the turbulent viscosity, υ_T has to be expressed in terms of the mean quantities. The most common turbulence models are the two equations models, which are based on transport equations. One of these models is the k-ϵ model, and in this model, the transport equations are solved for the turbulent kinetic energy and its dissipation ϵ. From these two quantities, the turbulent viscosity can be determined by the relation:

$$\upsilon_T = C_\mu \frac{k^2}{\epsilon} \tag{4.9}$$

where C_μ is a model constant. There are also other alternatives of the standard k-ϵ model, for example the Renormalisation Group (RNG) k-ϵ models, which has an additional term in the ϵ-equation to take into account the effects of the mean flow on the distortion of the turbulence. This model has been used for all the RANS computations presented in this thesis. In the Reynolds-stress models, model transport equations are solved for the Reynolds stresses, u_iu_j and for the dissipation, ϵ. Since the Reynolds stresses are computed, the turbulent-viscosity hypothesis is not needed. This has the advantage that effects of anisotropy of the turbulence, streamline curvature, swirling motions and high rate of strains are taken into account. Still, some terms in the Reynolds stress transport equations have to be modeled, with some more or less realistic assumptions. Unfortunately, there are no generally valid turbulence models. For plane boundary layer flow, most turbulence models work more or less well, simply since such simple flows are used for model calibration. On the other hand, the flow near a solid wall depends strongly on the shape of the boundary and the flow outside of the boundary layer. These effects make it difficult to have generally valid models. Treatment of the near wall turbulence is often done by using certain wall models. These models may work when the local flow conditions resemble those for which the model is calibrated for. The most common wall model is the so called (standard) wall function, which is based on the log-law behavior of the turbulent boundary layer on a plane wall at zero pressure gradient. Modifications to the logarithmic law of the wall to take into account effects of wall curvature and adverse pressure gradients have also been proposed. A more advanced wall model is the so called two-layer model, where simplified turbulence models are used in the viscous region close to walls whereas high Re turbulence model is used further away from the wall.

In LES, the large scales of the turbulent flow are resolved while the smaller scales are modeled. This implies that the resolved flow field is, in general, 3-dimensional and time dependent. These properties of LES make it a natural candidate for handling the pulsatile flow in the turbine. In LES, the dependent variables are low-pass filtered with a spatial filter. The filter width is defined through the smallest spatial resolution which can be related to the volume of the computational cell, $V_{cell}^{1/3}$, i.e. $\Delta = V_{cell}^{1/3}$. The governing equations for the filtered variables have additional terms as compared to the original equations. These terms have to be expressed in terms of the filtered variables in order to close the equations. In the momentum equation, the term that has to be modeled is called the subgrid scale stress (SGS-model). As for the RANS approach, different SGS-models exist, and the first proposed is the Smagorinsky model. In the Smagorinsky model, as in the RANS framework one introduces a modified viscosity and assumes that the effects of unresolved turbulence can be accounted for in analogy with the molecular viscosity. Thus, the total viscosity is the sum of molecular and SGS-viscosities: $\upsilon = \upsilon_{Physical} + \upsilon_{SGS}$. υ_{SGS} is assumed to be proportional to the absolute value of the rate of strain tensor $\bar{S}_{ij}$ and the filter width:

$$\upsilon_{SGS} = (C_s \Delta)^2 \left| \bar{S}_{ij} \right| \tag{4.10}$$

where C_s is a model constant. It has long been known that the Smagorinsky model is too dissipative, especially in the near wall regions and when rotational effects are present. In analogy with the RANS-approach, one has also proposed a one equation eddy viscosity model, where a transport equation for the unresolved turbulent kinetic energy is solved. In this model, υ_{SGS} is assumed to be proportional to the filter width and the unresolved turbulent kinetic energy:

$$\upsilon_{SGS} = C_k \Delta \sqrt{k_{SGS}} \tag{4.11}$$

One may argue against this model in addition to the simple fact that it has similar limitations as the Smagorinsky model. The small scales of turbulence are of local and universal character (i.e. independent on the particular problem due to their small scale, except close to the wall). Therefore the SGS effects should be expressed by local variables and not through an elliptic partial differential equation. Additionally, one may argue that eddies of different scales interact with each other similarly if the scale ratio is similar. This is the foundation of several SGS models such as the scale similarity and dynamic models. In the SGS models based on the scale similarity hypothesis, the subgrid tensor is approximated by an analogous tensor computed from the smallest resolved scales, c.f. Bardina *et al.* (1980). In the dynamic models, the SGS model coefficients are based on the local properties of the flow field, which implies that the coefficients are functions of space and time, c.f. Germano *et al.* (1991) and Ghosal *et al.* (1995). Based on the same argument one may also claim that the error in neglecting the SGS terms is of second order in the filter size. Thus, if the spatial resolution of the flow is high enough the SGS terms are small. In fact as the resolution is improved LES becomes DNS. With this in mind one may claim that for adequate resolution one may refrain from using an explicit expression for the SGS terms. This is the foundation for the so called Implicit LES, sometimes called ILES or MILES (Monotone Implicit LES). The size of the SGS term is only one factor in the considerations related to the modeling of the SGS terms. The SGS terms represent the effect of the small scales on the large ones and they should account for a net energy transfer from the resolved scales to the unresolved dissipative ones. Instantaneously, they also act to transfer energy in the other direction, an effect that is known and backscatter and which has not been quantified. Since the smallest scales are unresolved the SGS model should account for the dissipation. When no explicit SGS model is used, one may utilize the inherent dissipative properties of the numerical scheme, provided that the dissipation of the larger scales is negligible. It should be, however, emphasized that the accuracy of these methods depends of the grid size and numerical schemes. A first order scheme implies that the cut-off frequency will be lower compared to a higher order scheme since the artificial viscosity (dissipation) is higher for first order schemes compared to second order schemes. But, for seconds order schemes, such as the central difference scheme, the even derivate of the truncation error may introduce dispersion. Additionally, the scheme may not be dissipative enough which can result in non-physical oscillations in the flow field. The effect of these factors on the resolved scales is often small provided that the grid resolution is fine as compared to the resolved scales that are of interest. Marginally resolved flows may of course suffer from lack of accuracy since the numerical dissipation is proportional to the grid spacing. A measure of the local resolution can be assessed by considering the local turbulent energy spectrum and the extent of the resolved inertial subrange.

A disadvantage with LES is that the boundary layers have to be resolved to capture the dynamics in the near-wall regions. To be able to do this, the near-wall region must be resolved which results in a very large number of grid points. As in the RANS case, different wall models have been proposed and these can be divided into two categories:

- Modifying the SGS eddy viscosity in the region closest to the wall, for example a damping function of the viscosity or compute the eddy viscosity based on the logarithmic law of wall.
- Solve the one-dimensional boundary layer NS equations on a fine grid in the near-wall region. The fine grid can also be a "grid-within-the grid", where a one-dimensional grid is included in the cell layer closest to the wall.

For the LES-computations, the near-wall treatment is done by first inverting a third-order Spalding law to obtain u_τ and then compute the relevant fluxes on the basis of the estimated u_τ. For the case where the Smagorinsky model is used, a damping function is applied at the cell layer adjacent to the wall, where the filter width in this cell layer is defined as:

$$\Delta = min(\kappa y, \sqrt[3]{Cell\,volume}) \tag{4.12}$$

y is defined as the distance from the wall to the adjacent cell center and κ is a constant.

4.3.2. *Wheel modeling*

In the turbine, the turbine wheel is rotating in relative to the stationary turbine house. This can be modeled by two different approaches:

- The Rotating Reference Frame technique (RRF)
- Moving mesh technique.

In the RRF concept one uses a coordinate system that rotates with the turbine. Therefore, source terms to take the Coriolis and centrifugal forces are added to the Navier-Stokes equation. Since the housing of the turbine is not rotating, the computational domain contains also regions which are described in non-rotating coordinates. Hence the source terms are activated only in the region where rotation of the geometry occurs.

In the moving mesh technique, also called the Sliding Mesh (SM) technique, one part of the mesh is moving or rotating in relative to the stationary part. At the interface between the moving and the stationary part, the moving mesh is made to slide past the stationary part. At the sliding interface, the connectivity for cells on either side of the interface change at each time step. This is implemented in a way that there are no restrictions on the relative position of the cell faces on either side of the sliding interface, i.e. cell faces across the sliding interface do not to have a one-to-one correspondence. In order to preserve flux of mass, momentum and energy across the sliding interface and to avoid introducing non-physical perturbations, the interpolation over the sliding interface must be done in an appropriate way. The rotational speed of the wheel and cell sizes at the sliding interface will also determine the time step; the time step must be small enough to ensure that cells on both sides of the sliding interface do not pass each other completely during one time step.

4.4. Numerical accuracy and uncertainty

All numerical techniques are based on discrete approximations of the dependent variables and thereby a discrete approximation to the governing equations. The discretization steps in both the time and space introduce errors. The errors can be divided in four groups:

- Errors due to modeling errors in the governing equations.
- Discretization errors, due to time and space discretization and the used discretized representation of the dependent variables.
- Errors in computing the discrete solution i.e. convergence errors in solving the system of non-linear algebraic (discretized) equations.
- Errors due to machine round-off error; i.e. the limited number of significant digits of the computer and the accumulation of these errors during the computations.

The influence of these different errors can be examined by performing numerical accuracy studies (using successively refined grids) and comparing the results from the computations against measured or computed data. Modeling errors at relatively low Re and simpler geometries can be also assessed using DNS data. However, DNS is not an option for the turbo-charger geometries under consideration in this thesis.

The purpose of numerical accuracy studies is to state the order of accuracy of the used schemes. The numerical accuracy studies can also be used to compute the uncertainty of the results. To investigate the numerical accuracy and the uncertainty, the Grid Convergence Index (GCI) approach proposed by Celik (2005) was used. The results from these studies show that the order of accuracy for the used code is between 1 and 2, depending on the flow case and the used turbulence modeling approach, see Paper 1. This order accuracy reflects the order of accuracy of the used schemes, where the formal second order MARS scheme is used for spatial discretization of the convection terms and a blended central difference scheme for the viscous terms. A blended Crank-Nicholson scheme was used for temporal discretization of the LES computations for the pipe cases and the first order Euler implicit temporal discretization and was used for the turbine computations and for the RANS computations. The GCI-method can also be used to estimate the uncertainty of the results. For the pipe-flow cases, the uncertainty of the computed velocity field at the finest grid was below 4% for the LES computations for the single bend case, and for the RANS computations on the double bend case the uncertainty was below 9.6% for the finest grid.

For pulsatile flow, the evaluated quantity must be phase averaged. The total number of (statistically independent) samples can be computed with a formula given in Johansson & Alfredsson (1988) for a given a given sampling error ϵ:

$$\epsilon(X) = \frac{1}{\sqrt{N}} \frac{x_{rms}}{X_m} \tag{4.13}$$

where N is the total number statistically independent samples, X_m is the mean value and x_{rms} is the standard deviation (i.e. rms) of the variable X. Since the inflow conditions for the double bend pipe was pulsating, the velocities must be phase averaged in the LES computations, which implies that 400 cycles had to be computed if the sampling error should be below 1%. This figure requires too long computations and hence the sampling error is larger than this figure.

For the turbine computations, the numerical accuracy study was performed on simplified turbine geometry, where the complete wheel and only parts of the volute and the diffuser were modeled to reduce the computational time. The rotational speed for the rotor was 97 897 rpm and a fixed mass flow was specified at the inlet. In this numerical accuracy study, the SM-technique was used to handle the rotation of the wheel.

TABLE 1. Computational accuracy study

Grid number	Number of cells in the rotor	Averaged cell size (mm)	Shaft torque (Nm)	Pressure drop (kPa)
1	76 662	0.65	0.362	30.90
2	297 648	0.42	0.276	30.28
3	541 008	0.34	0.287	29.86
4	968 229	0.28	0.290	29.83

As can be seen in Table 1, the convergence for Grid 2, Grid 3, and Grid 4 is monotone and the uncertainty for the shaft torque for the finest grid is about seven percent and for the pressure drop 0.3%. The resolution for the computations for the complete turbine cannot be as fine as it was for Grid 4 in the accuracy study, due to the too long computational time.

4.5. Comparison of computed and measured data

The numerical accuracy studies do not reveal whether the numerical methods compute an approximate solution to the physical problem itself. Such information requires a direct comparison between the numerical results to measure or very accurate computational data (DNS) when it is possible to compute such data. In Paper 1, the computed results were compared to measured data for the flow in a single bent pipe. The measurements were performed by Sudo *et al.* (1998), and the same geometry and bulk velocity was used in the computations. Three different turbulence models were tested, a $k-\epsilon$-RNG RANS turbulence model, Smagorinsky LES turbulence model and Implicit LES and the results show that the Implicit LES gave the best agreement with measured data, see Figure 5.3.

Since no measurements of the flow field for the used turbine were available, the computed performance for the turbine was compared to global data measured in the gas-stand at SAAB Automobile, Trollhattan. Keeping in mind the used wall boundary conditions, the uncertainty of the inlet conditions and the numerical uncertainty, the results show fairly good agreement, especially for the case where the LES turbulence modeling approached is used in combination with the Sliding Mesh technique. In Paper 7 different causes for the differences in the results are discussed. Also, the agreement between measured and computed global data, such as pressure ratio, temperature and mass flow rate for the compressor are fairly good, see Paper 8.

The computer code used here have also been used to investigate the performance and the flow field in turbines by Palfreyman & Martinez-Botas (2005), who investigated the flow field in a medium sized mixed flow turbocharger turbine for a pulsating operating condition. The unsteady RANS computations with the Sliding Mesh technique were compared to experimental data and flow field measurements by Laser Doppler Velocimetry (LDV). They concluded that the agreement for both phase averaged and instantaneous data was reasonable, but there remained some uncertainty over the used inlet conditions. Palfreyman *et al.* (2002) used the same code with a RNG k-ϵ turbulence model to compute the non-pulsatile flow field in a mixed flow turbine. They concluded that the computed flow field agreed well with measured LDV data at the turbine exit. The turbine efficiency also agrees well with measured efficiency over the test range.

All this together indicates that the CFD code can be used to predict the performance of the turbine and that the code predicts the time resolved three-dimensional flow field in a reasonable way.

CHAPTER 5

Results

In this chapter, the most important and interesting results from the performed studies will be discussed. To start with, the results from the pipe flow study are presented, followed by the results from the investigations of the unsteady flow in the turbine and the compressor.

5.1. Non-pulsatile and pulsatile flow in curved pipes

The objective with this study has been to assess the unsteady flow in curved pipes. The two different geometries that have been used in this study are depicted in Figure 5.1. One of the considered geometries is similar to a runner on an exhaust manifold and the results from the investigation are used to assess the physics of pulsatile flow. The results from the computations for the other geometry are compared with measured data from the experiments performed by Sudo *et al.* (1998). When verifying computations against measured data, there is always an uncertainty about the experimental boundary conditions and in particular the inlet conditions. For example, the decay of vortices and swirl in pipes is slow, which has been shown in different studies, see for example Anwer & Lai (1989), Mattingly & Yeh (1991), Steenbergen & Voskamp (1998) and Najafi *et al.* (2005). Therefore, an investigation of the influence of the inlet conditions on the flow field has also been carried out.

5.1.1. *Method and computed cases*

The Navier-Stokes equations have been solved numerically and different turbulence modeling approaches have been considered; the RANS and the LES approach. In the RANS computations, the k- ϵ *RNG* (Yakhot *et al.* (1992)) turbulence model has been used. The second order MARS scheme has been used for spatial discretization of the non-linear terms. Euler implicit temporal discretization is employed for integration of the momentum equations in time. The pressure is updated in each time-step, through the PISO procedure.

For the LES computations, two different subgrid scale modeling approaches have been used; the Smagorinsky model and Implicit LES. Different spatial discretization schemes have been tested, where the central difference scheme gives oscillations. Even a blended central difference scheme introduced wiggles.

The MARS scheme is a second order scheme that gives a solution without non-physical oscillations. A blended Crank-Nicholson scheme has been used for temporal discretization.

The computational domain for the single bent pipe consists of three parts, a straight section, a bend section and a second straight section, see Figure 5.1. The pipe diameter is 104 mm and the bend has a curvature radius of 208 mm, which gives a radius ratio of 4. The first section has a length of 14.5 diameters and the second straight section has a length of 12.5 diameters. For this case, a velocity profile is applied at the inlet.

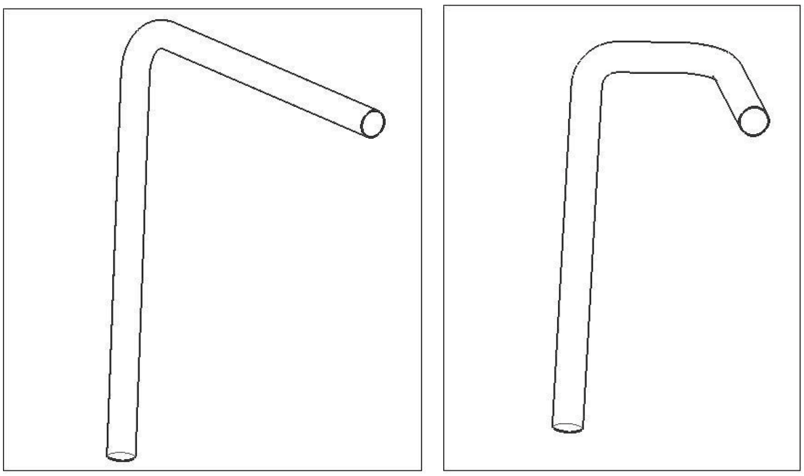

FIGURE 5.1. Computation domains.

The diameter for the double bent pipe is 10 mm. The pipe has two bends with radius r_1=10 mm and r_2=15 mm, respectively. The inlet section is 12 diameters long, the section between the two bends is 2.5 diameters long and the outlet section is 6 diameters long. This pipe has a similar shape as one of the runners of an exhaust manifold found on a turbocharged IC-engine. At the pipe inlet, a time resolved mass flow pulse and temperature are specified and at the outlet a constant pressure is applied. The walls are assumed to be smooth and adiabatic. The time averaged bulk velocity is 110 m/s, which corresponds to a Reynolds number of 8900. The maximal velocity is 250 m/s, which corresponds to a Reynolds number of 20 200. The frequency is 50 Hz which gives a Womersley number of 8.

5.1.2. *Non-pulsatile flow in a single bent pipe*

The time mean flow obtained from the LES computation shows that the Dean vortices are created in the inlet region of the bend ($\varphi \approx 30^\circ$) , which is about the same location as reported in the experiment performed by Sudo *et al.* (1998). At the exit of the bend, the time mean secondary flow consists of the counter-rotating Dean vortices with the centers located in the lower part of the pipe, as shown in Figure 5.2. The axial velocity has a C-shaped distribution in the cross-stream plane, with its maximum at the outer part of the bend. The Dean vortices dominate the secondary flow at the region downstream of the bend and the vortex cores are moving up against the center of the pipe when they are convected downstream. Ten pipe diameters downstream of the bend, the vortices have almost dissipated and the axial velocity distribution is still C-shaped at this location. The instantaneous secondary flow at the exit plane of the bend is not symmetric and at certain instants up to six vortices, where two of them are counter-rotating with respect to the Dean vortices, is observed. These vortices are meandering in the cross-stream plane and the C-shaped axial velocity contour is meandering from one side of the pipe to the other side and the Dean vortices at each side move up and down with varying strength. The axial velocity and the location of the Dean vortices is varying with a Strouhal number of approximately 2, where the Strouhal number here is based on the bulk velocity and the pipe radius.

The comparison of the computed velocity profiles with the measured profiles has been conducted at three different locations; half a diameter upstream of the bend, at the exit of the bend and half a diameter downstream of the bend. Half a diameter upstream of the bend, the deviations between the computed and measured velocity profiles are smaller than the measurement error. At the evaluation stations downstream the bend, the deviation is larger and the RANS computation could not capture the behavior of the flow field, especially at the inner wall, where the computed streamwise velocity is lower for all cases than it is in the measurement, see Figure 5.3. The time mean velocity profiles from the LES computation gives better agreement with the measured velocity profiles at all evaluation stations, but the LES computations over-predict the axial velocity at the outer part of the bend and under-predict the velocity in the center part of the cross-section of the bend.

Despite the fact that the results from the RANS method gave the largest deviation from the measured velocities, this model is used to investigate the effects of perturbations at the inlet. The reason is the long computation times that are required for the LES approach. Different inlet velocity profiles are applied at the inlet to the single bend pipe. The imposed eccentricity and swirl are used to assess the sensitivity of the results to inlet perturbations. These types of perturbations are often found in experiments where the inlet pipe is

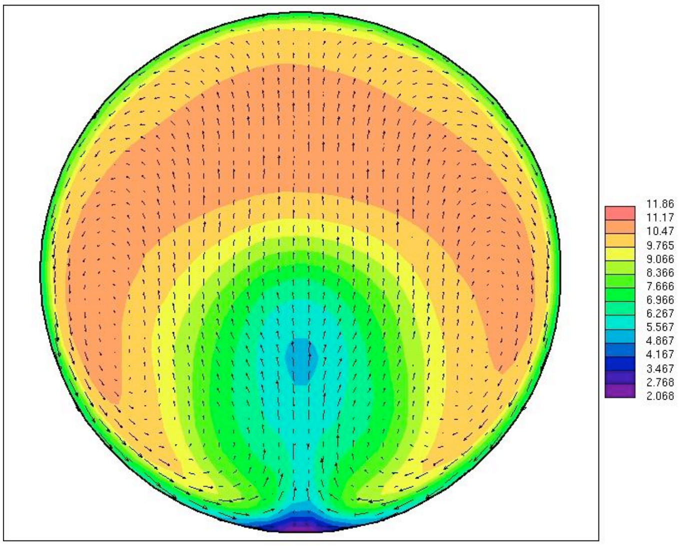

FIGURE 5.2. The counter-rotating Dean vortices at the outlet of the bend. Contour: mean axial velocity component, vector: In-plane mean velocity components.

short and no fully developed turbulent pipe flow can develop. When comparing the velocity profiles for the different cases with measured velocity profiles, it is clear that the case with the swirling motion gives the best agreement at the exit of the bend. One way to give a measure of the inlet effects is to compare the Root Mean Square (RMS) value of the $\Delta U/\Delta\zeta$, where ΔU is the difference between the velocity profile obtained with a symmetric velocity profile and a non-symmetric or swirling velocity profile at a certain station. $\Delta\zeta$ is the difference in kinetic energy at the inlet for the symmetric inlet profile and a non-symmetric or swirling inlet profile. Table 1 shows the results from the analysis at the exit of the bend and it is clear that inlet condition with swirling flow gives the largest effect. In this case the flow field is rotated due to the swirling motion before the bend and hence, the low velocity region is turned a few degrees in the clockwise direction. This is also the inlet profile which gives the best agreement with the measured velocity profiles downstream of the bend, which indicates that there probably is a swirling secondary flow component in the experimental case too.

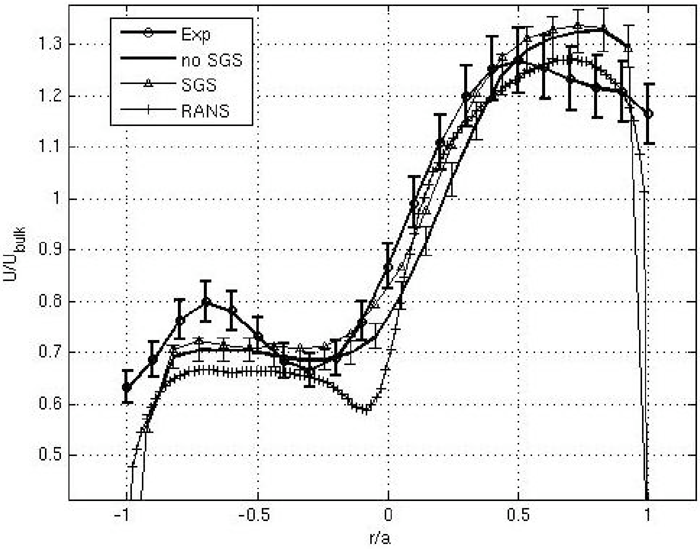

FIGURE 5.3. Results from RANS and LES computations. Streamwise component half a diameter downstream of the bend. The error bars are related to the experiments of Sudo *et al.* (1998).

TABLE 1. RMS value of $\partial U/\partial\zeta$ at the exit of the bend

Inlet profile	Eccentric 1	Eccentric 2	Eccentric 3	Swirl
RMS ($\partial U/\partial\epsilon$)	0.093	0.046	0.16	0.55

5.1.3. *Pulsatile flow in a double bent pipe*

The pulsatile flow in the double bent pipe has been computed with both the RANS and the LES approach. In this section, the results from the LES computations are presented.

During the acceleration phase of the inlet velocity, the Dean vortices are created in the first bend. At the outer part of the entrance to the first bend a recirculation zone is located during the whole pulse period, except when flow reversal occurs. The recirculation is an effect of the adverse pressure gradient in the streamwise direction at the outer wall. At the entrance to the second bend, the maximum velocity region is located at the inner wall, which means that the region of maximum velocity is rotated 90° from the exit of the first bend. The secondary flow downstream of the second bend is dominated by

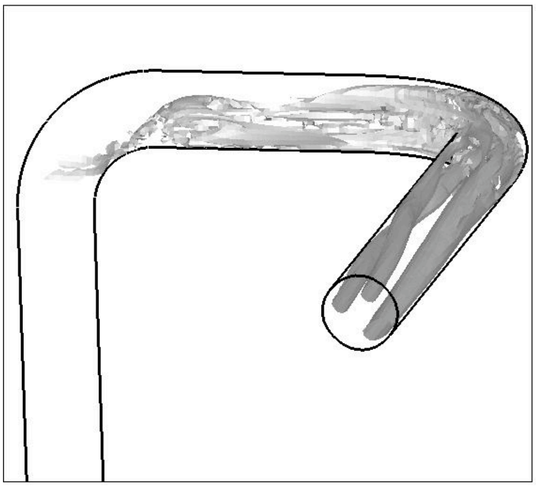

FIGURE 5.4. λ_2 showing the different structures in the pipe.

a swirling motion and the Dean vortices formed in the second bend. One of the Dean vortices from the first bend interacts with the swirling motion. Further downstream, the strength of the Dean vortices from the second bend are decaying, but they still have an influence on the main secondary swirling motion, which is not symmetric, as shown in Figure 5.4. The figure depicts the iso-surface of the vortices using the λ_2 criterion for defining a vortex (Jeong & Hussain (1995)). The location of the center of the swirling motion is not stationary in the cross-stream plane during one pulse and the strength of the swirling motion at the outlet varies with the amplitude of the axial flow. During the last part of the deceleration phase at the inlet, flow reversal occurs in the boundary layer at the walls of the pipe, while the flow in the center part of the pipe is not reversed, as shown in Figure 5.5.

As mentioned in a previous section, pulsating flow results in a time-dependent phase shift between the bulk flow and the pressure. For the LES computation the corresponding range of phase lag is between 19° and 52°. The maximum phase shift occurs when the inlet flow changes direction, and the minimum phase shift occurs when the mass flow reaches its maximum at the inlet. At minimum phase shift, the turbulent energy is much higher than it is when maximum phase shift occurs, which is in agreement with the conclusions by Ramaprian & Tu (1983).

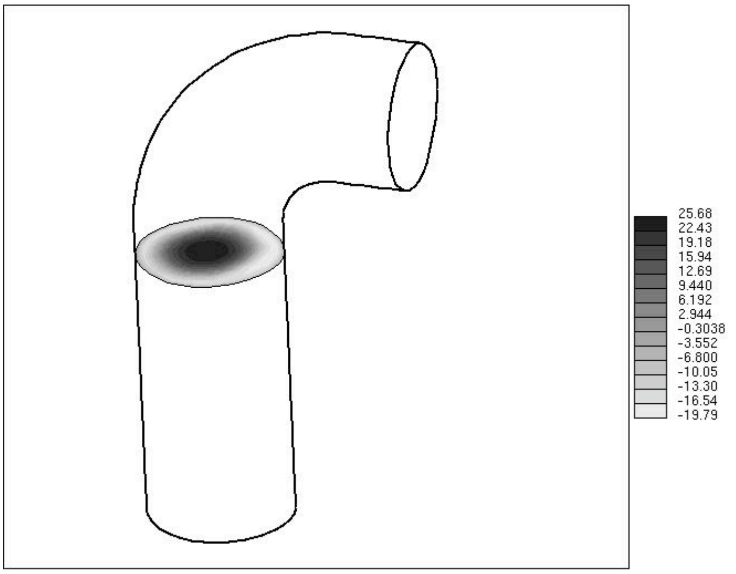

Figure 5.5. Instantaneous axial velocity component, showing the effect of pulsating flow with reversed flow near the wall.

5.2. Unsteady flow in a radial turbine

5.2.1. *Method and geometry*

For the turbine computations, the LES approach has been used, since the comparison with measured data showed that this approach gave the best agreement, as will be discussed later. This approach is much more computationally expensive as compared to solving the RANS equations. However, with LES the most energetic turbulent scales are resolved and thereby one gets more information about the character of the flow in the turbine. The results from the LES computations can also be used to extract the acoustical source terms that can be used to compute the noise generation in the turbine. As in the pipe cases, the second order MARS scheme has been used for spatial discretization of the convection terms. For the temporal discretization the first order implicit Euler scheme has been employed. The pressure has been updated using the PISO algorithm at each time-step. The wheel is modeled by the sliding mesh technique, which implies that the mesh which represents the turbine wheel is rotating relative to the stationary turbine house.

The turbine under consideration is a commercially available turbine with a size that is typical for a turbocharger mounted on a 2.0 liter IC engine of a passenger car. The turbine is a nozzle-less, nine bladed radial turbine with the waste-gate valve closed. The complete turbine and the turbine wheel are shown in Figure 5.6. The leading edge tip radius of the wheel is 22.10 mm and the trailing edge tip radius is 18.75 mm.

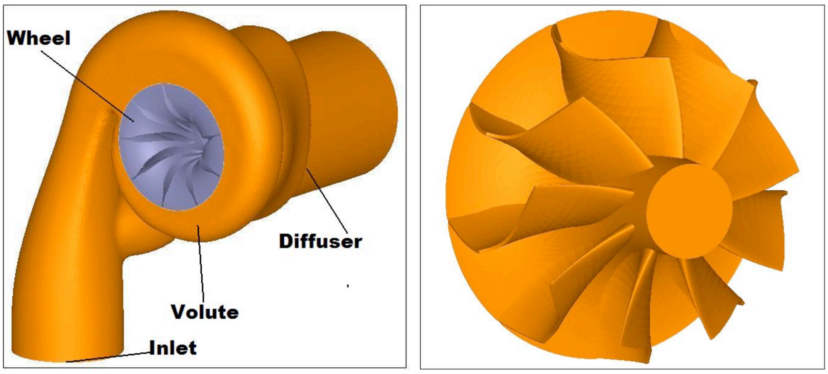

FIGURE 5.6. The complete turbine geometry and the wheel.

5.2.2. *Non-pulsatile inflow conditions*

In this section, results from two different studies are presented. The first part is from a study (Paper 7) with the objective to assess how different modeling strategies affect the computed results. The computed performance with the different modeling strategies are also compared with measured data. The second part discusses the results from a study (Paper 3) where the effects of different perturbations at the inlet on the performance of a radial nozzle-less turbine have been assessed.

5.2.2a. *Assessment of modeling techniques.* The different modeling strategies that are considered are two different turbulence modeling approaches; RANS (with k-ϵ turbulence model Yakhot *et al.* (1992)) and implicit LES and two different ways of modeling the rotation of the wheel; Rotating Reference Technique (RRF, also known as the frozen rotor technique) and Sliding Mesh (SM) technique, respectively. The computed performance is also compared to measured turbine performance, where the measurement was carried out in the new gas stand at SAAB Automobile in Trollhattan, Sweden. A numerical study performed by Hellstrom & Fuchs (2008*a*) showed that the flow into turbine affected the performance of turbine, and therefore, Particle Imaging Velocimetry (PIV) measurements were performed of the flow in a test section upstream of the turbine to get proper flow conditions into the turbine. To resemble the conditions in the gas stand and the locations of the measurement points, the inlet and outlet pipes to the turbine were extended.

As can be seen in Table 2, different boundary conditions for the walls and the inlet are also considered. At the inlet, two different inlet conditions are used, but for both inlet conditions, a constant mass flow rate of 0.125 kg/sec is specified and the temperature is set to 25°C. The differences between the cases are that for the *top hat* inlet condition, the velocity profile is a top hat profile (constant velocity over the cross section), while for the so called *profile* case, the measured velocity profile is used. To assess the influence of heat transfer effects at the walls, one case with fixed wall temperatures is considered. For this case, the wall temperature at the inlet pipe is specified to 50°C (due to heating of the PIV-measurement section), the temperature of the turbine house is set to 30°C and the temperature of the outlet pipe is set to 10°C. For the other cases, all walls are treated as being adiabatic.

At the outlet of the domain, a constant pressure of 101.3 kPa is applied for all cases. The rotational speed of the wheel is set to 98 000 rpm, which is the same as in the measurements.

TABLE 2. Computed cases

Case number	Turbulence modeling approach	Wheel modeling	Inlet condition profile	Wall temperature modeling
1	RANS	RRF	Top hat	Adiabatic
2	RANS	RRF	Profile	Adiabatic
3	RANS	RRF	Top hat	Fixed temp.
4	LES	RRF	Top hat	Adiabatic
5	LES	SM	Top hat	Adiabatic
6	URANS	SM	Top hat	Adiabatic

In Table 3, the different performance data are reported for the different cases. As can be seen, the LES together with the SM technique gives the best agreement with measured data. As also can be seen, data from the URANS case with SM (Case 6) is not reported. The reason is that for this case the shaft power fluctuates with an amplitude that is almost as large as the time mean shaft power for Case 5. The frequency of the fluctuations together with speed of sound gives a wave length that corresponds to length scale that is in the order of blade passage length and in the results one can clearly see that pressure waves are propagating between the blades and the inlet region of the wheel. Since the perturbation at the tongue is of high frequency (with the frequency in same order as the turbulent fluctuations), it interacts with the modeled turbulence, which then amplifies the perturbation. This interaction results in strong pressure fluctuations in the wheel.

TABLE 3. Measured and computed performance

Case	Inlet pressure (kPa)	Outlet temperature °C	Shaft power (kW)	Isentropic efficiency (%)
Measured	185.5	1.5	3.4	56
1	182.1	-11.2	4.4	74
2	181.8	-10.5	4.4	74
3	182.0	-9.1	4.4	74
4	181.3	-10.1	4.3	73
5	186.0	0.1	3.6	59

The two different inlet velocity profiles used in the RANS-computations do not affect the performance of the turbine, and this is due to the long pipe that is mounted upstream of the turbine, which implies that the any skewness in the inlet velocity profile will disappear before the inlet to the volute. Since the temperature of the gas is almost the same as the room temperature, the assumption of adiabatic walls also seems to be fair. Even though Case 5 shows the best agreement with measured data, there are deviations between the measured data and the computed data of Case 5. This discrepancy is due to the uncertainty in the boundary data taken from the measurements and used in the numerical computation. Additionally, there are uncertainties in the shaft power and efficiency which is obtained in the measurements. Since no dynamometer has been used, the turbine power is calculated from a measurement of temperature rise over the compressor, and therefore the bearing losses are included in the computed turbine efficiency. The bearing losses can at certain operation points (low PR and mass flow) not be neglected, which is a problem when comparing measured data with data CFD-computed data.

The computations with the rotating reference frame technique, regardless of turbulence model, over-predict the shaft power, which also results in a too low temperature at the outlet. The main difference in the RRF and SM approaches is that the wheel is actually rotating in the SM approach, while it is stationary in the RRF approach. This implies that the effects of blade passage at the tongue can be either be stronger or weaker, depending on how the blades in the stationary grid is located in relative to the tongue. With the sliding mesh technique the blade passage effects are captured, which gives pressure fluctuations which propagate both upstream and downstream. These pressure waves will increase time averaged pressure upstream of the turbine, but they will also introduce viscous losses, but this is most probably a secondary effect. For the RRF cases, where the wheel is stationary, the dynamics of the blade passage effects are of course not captured. With the RRF-technique the flow field in between the blades is much smoother and uniform compared to the flow field computed with the SM technique. For Case 1, one can observe that the velocity in between the blades is perturbed at the tongue, but this perturbation does not affect the flow in between the other blades, since the wheel is stationary. For the SM-technique, the rotation of the wheel implies that the tip vortex, which is formed after the blade has passed the tongue, is stronger during the first half part of the revolution and then becomes weaker in strength, but the spatial extent of it is getting bigger. This non-uniform flow will then affect the pressure distribution at the blades, and the shaft power output. In Figure 5.7, the pressure fields for Case 1 and Case 5 is plotted at a plane that intersects the leading edge of the blades and the pressure distribution is more uniform and smoother for Case 1 compared to Case 5, which is a result of the stationary wheel. The more uniform and smoother pressure distribution for the RRF case in the wheel implies that the turbine wheel can extract more energy out of the gas, which also results in a lower temperature after the wheel, which is reported in Table 3.

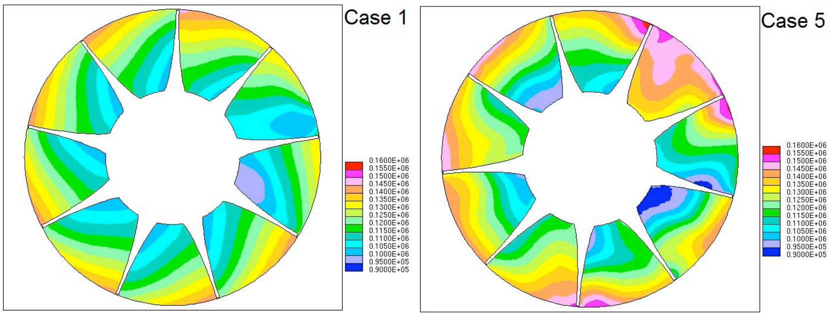

FIGURE 5.7. Pressure distribution in the wheel for Case 1 (time averaged) and Case 5 (snapshot).

5.2.2b. *Inlet perturbation study.* In the inlet perturbation study, five different inlet conditions have been considered and these are given in Table 4. For all cases, a turbulent velocity profile and the temperature are specified at the inlet boundary and different perturbations are added to this velocity profile. The mass flow at the inlet to the turbine has been kept constant (equal to 0.08144 kg/s) by varying the velocity. The temperature at the inlet has been set to 1000°C for all cases. At the outlet, a non-reflective boundary condition is applied. The walls are assumed to be smooth and adiabatic.

TABLE 4. Computed cases

Case	Turbulence intensity	Secondary flow	Strength of secondary flow
1	0%	-	-
2	5%	-	-
3	5%	Dean	0.10
4	5%	Swirl	0.28
5	5%	Swirl	1.5

In Figure 5.8 the axial and azimuthal velocity components at the inlet to the turbine are plotted for the different cases. For Case 1, no perturbations are added. Case 2 had an inlet profile with turbulent fluctuations. The turbulence intensity for Cases 2-5 is 5% and the turbulent fluctuations at the inlet boundary are created by the method proposed by Klein *et al.* (2003). Case 3 has both turbulent fluctuations and secondary flow in the velocity profile, where the secondary flow consists of a pair of counter-rotating Dean vortices, see Figure 5.9. Cases 4 and 5 have, in addition to the turbulent fluctuations, a swirling motion added, where Case 5 has the stronger swirl. The strength of the swirl at the inlet is defined as the azimuthal velocity at the edge of the inlet boundary divided by the axial bulk velocity. The strength of the Dean vortices is defined as the area averaged value of the secondary component divided by the

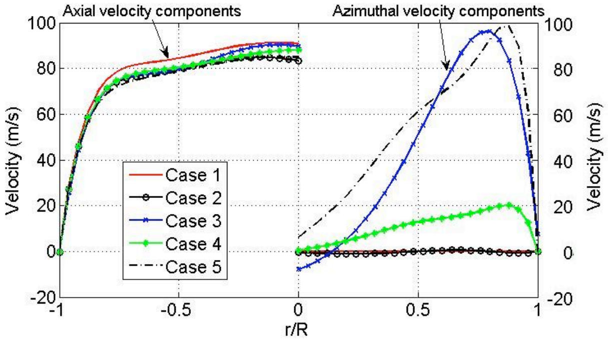

FIGURE 5.8. Axial and secondary velocity components at the inlet.

axial component at the inlet. The strength of the secondary flow is obtained from LES-computations of the pulsatile flow in a four to one exhaust manifold.

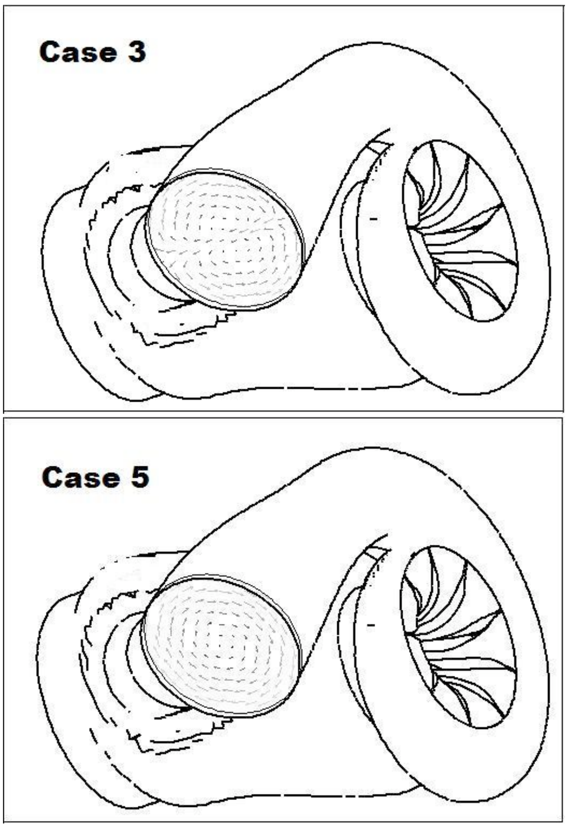

FIGURE 5.9. The secondary flow at the inlet plane for Case 3 and 5, respectively.

The evaluated time averaged data has been gathered for the last 4 of 20 revolutions of the turbine, which corresponds to 36 blade passages. In Figure 5.10 the time resolved shaft power for the different cases are shown. The shaft power fluctuates with a frequency that corresponds to the blade passage frequency. Fluctuations with lower frequencies are also present for all cases, depending on flow unsteadiness in the volute. In Table 5 the time averaged shaft power and two different ways of expressing the efficiency are given. For the time mean value of the shaft power, there are differences between the cases. The time mean shaft power for Case 5 is 19% lower than for Case 1, which is greater than the estimated numerical uncertainty. For Cases 2-4, the differences in the shaft power as compared to Cases 1 or 5 are of the same order as the

Table 5. Shaft power, available power at the inlet, isentropic efficiency, utility factor and pressure ratio

Case	P_{SHAFT} (kW)	P_{INLET} (kW)	η_{is}	κ	PR
1	5.02	82.18	0.66	0.061	1.41
2	4.34	82.14	0.66	0.053	1.34
3	4.41	82.26	0.64	0.054	1.36
4	4.40	82.12	0.66	0.053	1.35
5	4.05	82.35	0.64	0.048	1.32

numerical uncertainty (see Chapter 4). Altogether, the computations show that different perturbations at the inlet do affect the performance of the turbine. As can be seen in Table 5, the isentropic efficiency does not reflect the fact that the shaft power is almost 20% lower for Case 5 as compared to Case 1. This is so since the isentropic efficiency also takes into account the energy content of the flow after the turbine, which can be used to drive a second turbo-charger. A better definition of the efficiency is the utility factor, κ. The utility factor is defined as:

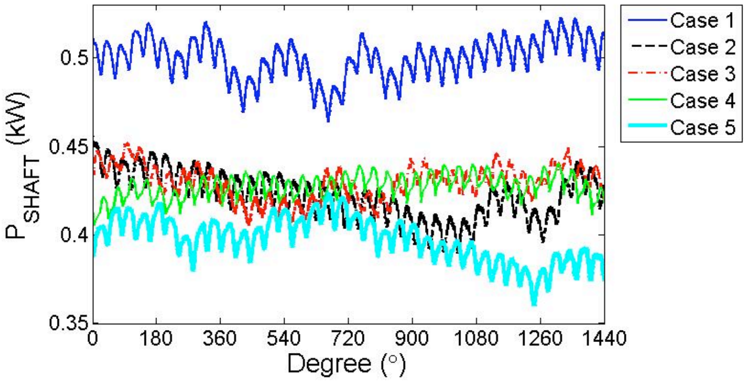

Figure 5.10. The time resolved shaft power for the different cases during 3 turbine wheel revolutions.

$$\kappa = \frac{P_{SHAFT}}{P_{INLET}} \tag{5.1}$$

where P_{SHAFT} is the shaft power and P_{INLET} is the available power at the inlet boundary, and is defined as:

$$P_{INLET} = \int_{Inlet} \left(\frac{1}{2} \cdot u_i \cdot u_i + h \right) \rho U_n dA \tag{5.2}$$

where the velocity u_i, density ρ and the specific enthalpy h is at the inlet boundary. U_n is the normal velocity component. This definition better reflect the effects of the perturbation at the inlet. The utility factor can also be viewed as an efficiency parameter which reflects the ability of the turbine to extract power from the provided power. A result from the different perturbations at the inlet is that the axial inlet velocity component is different for the different cases, as seen Figure 5.8. This is so due to different absolute pressure at the inlet. Although Case 1 has the largest pressure ratio over the turbine it has the lowest absolute pressure at the inlet and the outlet, since the turbine extracts most energy from the gas for this case. The lowest pressure for Case 1 results in the highest perpendicular velocity at the inlet, and hence, the highest velocity in the volute and into the turbine wheel, as depicted in Figure 5.11.

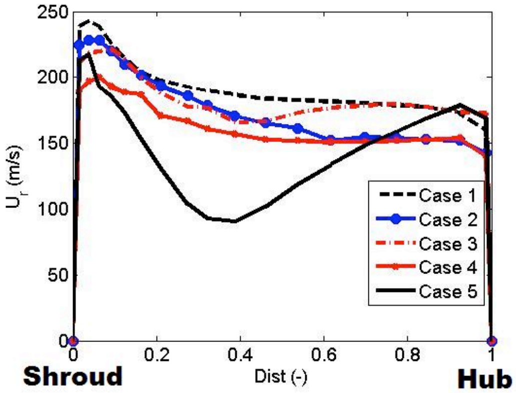

FIGURE 5.11. The radial velocity component for the different cases at the inlet to wheel at a location that corresponds to an azimuthal angle of 90°. Positive velocity is defined as being directed inwards.

For all cases, a coherent structure is created at the inlet to the waste gate channel and it is convected downstream. For Cases 1-4 the vortex from the waste gate channel interacts with the wake downstream of the tongue. For Case 5 the vortex that is created at the inlet to waste gate channel does not interact with the wake downstream of tongue since it is convected downstream at the side of the tongue, as seen in Figure 5.12. In the volute, the strength of this vortex increases due to the radial pressure gradient. These two counter-rotating vortices, shown in Figure 5.13, are meandering in the cross-stream

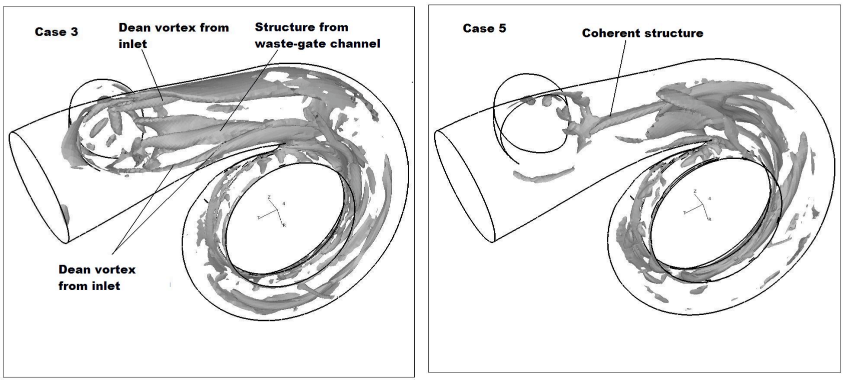

FIGURE 5.12. λ_2 for Case 3 (left) and Case 5 (right), showing the coherent structures created at the inlet to waste-gate channel.

plane which create a non-uniform velocity distribution into the turbine wheel in space and time. The highly swirling motion at the inlet also feeds the wake behind the tongue. This effect can be seen in the energy spectra at a location just downstream of the tongue. Case 3 has the highest fluctuating energy at a point downstream of the tongue, whereas Case 1 has the lowest fluctuating energy.

The non-uniform and in time varying axial velocity distribution in between the blades affects the pressure distribution at the blades. In Figure 5.14 the instantaneous pressure coefficients C_p are plotted for both the suction and the pressure side of a blade for the five cases along the chord between the tip and the hub. C_p is computed for the same blade and the phase angle for the different cases. Case 1 has the best pressure distribution. This is also the case with the highest axial velocity in between the blades. Case 5 has the lowest axial velocity in between the blades, which is also reflected in C_p. Since the flow for all cases is unsteady, the pressure distribution varies depending on where the blade is located during the revolution. The largest differences among the different cases are on the suction side, since this blade side is the most sensitive to changes of the relative incidence angle.

The highest velocity for Case 1 in between the blades implies that this case has the strongest azimuthal pressure gradient. This results in the strongest tip vortices at the leading edge of the blades. Case 5, which has the lowest velocity in between the blades, has the weakest tip vortices. The secondary flow structures in between the blades seem to have a secondary effect on the shaft power output.

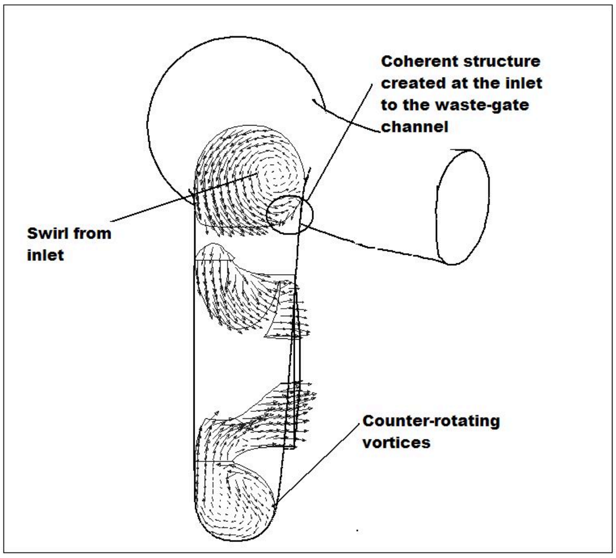

FIGURE 5.13. In-plane velocity components for Case 5, showing the coherent structure created at the inlet to waste-gate channel.

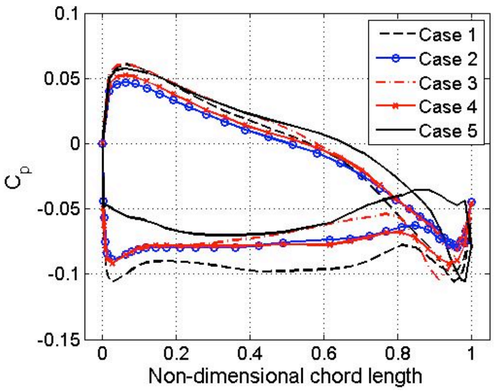

FIGURE 5.14. The instantaneous pressure coefficient along the chord of a blade at the pressure and suction side.

5.2.3. *Pulsatile flow in turbocharger*

Three different studies have been performed to assess the flow field and the performance of the turbine under pulsatile flow conditions. In one of the studies (Paper 2), the effects of different amplitudes and frequencies on the performance and the flow field were assessed. In another study (Paper 4), the combined effect of different secondary perturbations at the turbine inlet and the pulsatile flow on the turbine performance was assessed and quantified. The considered geometry in this study consisted of an exhaust manifold and a radial turbine. Also, the effects of heat transfer at the housing walls on the turbine performance have been assessed (Paper 5 and Paper 6). The performance data from the 3-D simulations have also been used to compute the turbine performance with a 1-D code and the results are compared (Hellstrom *et al.* (2010)).

5.2.3a. *Effects of different amplitude and frequencies.* Three different cases have been computed, where Case 1 has a frequency, mass flow and temperature corresponding to an engine working with wide open throttle at a speed of 1500 rpm, see Figure 5.15. The rotational speed of the turbine is 97 897 rpm. Case 2 has the same mass flow and temperature profile as for Case 1, but the frequency of the pulsations is ten times higher. This is not a realistic case for a turbocharger of a passenger car, but this case is used to investigate the effects of a higher frequency of the pulsatile inlet conditions. For Case 3, the inlet conditions and the rotational speed of the turbine corresponds to an IC-engine working at 3000 rpm. The rotational speed of the turbine for this case is 150 000 rpm. The inlet conditions are shown in Figure 5.15. At the outlet, a minimal reflecting pressure condition is applied to ensure that no reflected pressure waves contaminate the numerical solution.

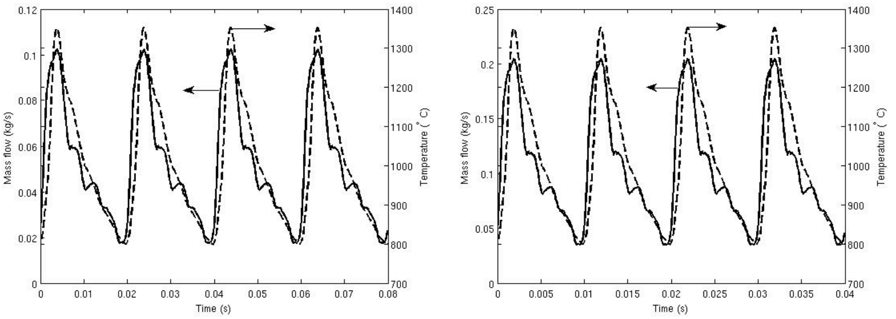

FIGURE 5.15. Specified mass flow and temperature at the inlet to the turbine for Case 1 (left) and Case 3 (right), respectively.

The shaft power varies during the pulse, as shown in Figure 5.16. As can be seen, the shaft power is higher when the mass flow at the inlet is decreasing. The isentropic efficiency, η_{is} also varies during the pulse. At certain times the nominal efficiency is negative since at these instances the shaft torque is itself negative due to a fixed rotational speed of the turbine wheel. The same behavior for a mixed flow turbine at pulsatile flow conditions at the inlet was reported by Palfreyman & Martinez-Botas (2005) who conducted both numerical computations and experiments to investigate the performance of mixed flow turbine working under pulsatile flow conditions. As also can be seen in the plots of the shaft power, an oscillation with a frequency corresponding to the blade passage is superimposed on the shaft power. The local minimum of the shaft torque occurs when the blade passes the tongue which gives a disturbance of the pressure distribution on the blade, resulting in a disturbance if the shaft torque.

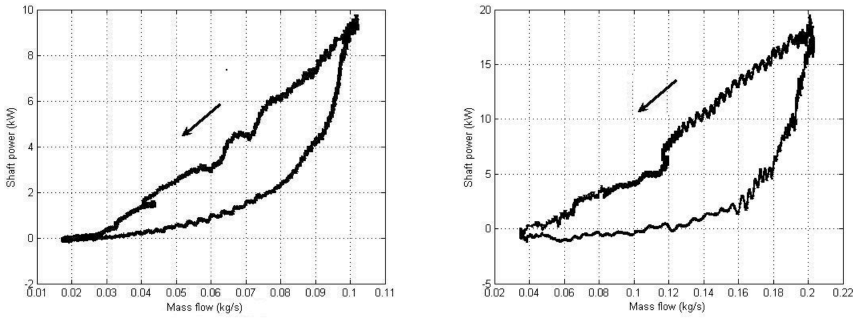

FIGURE 5.16. Computed shaft power vs. mass flow at inlet for Case 1 (left) and Case 3 (right), respectively.

The flow field has only been investigated in detail for Case 1 and Case 3, since the conditions of Case 2 is not encountered in engines for passenger cars. The major difference between the flow fields in the volute for Case 1 and Case 2 is that Case 2 has higher velocity in the volute due to the phase shift between pressure and mass flow. The higher velocity in the volute for Case 2 implies that the inlet angle to the turbine wheel is different, which gives incidence losses, and hence, affects the shaft power in a negative way.

The incidence angle of the flow into the wheel varies during the pulse, due to the varying mass flow at the inlet. In Figure 5.17, the relative inlet angle for 90° azimuthal angle is plotted for Case 1 and Case 3. As can be seen, the inlet angle for Case 1 varies from approximately -85° to 60°. For Case 3, the inlet angle varies from approximately -67° to -25°, which is more favorable. For Case 1 only a small phase shift occurs between the mass flow and the pressure at the inlet. The shaft torque is also almost in phase with the mass flow and pressure at the inlet. When the frequency increases, the phase shift is significant. This implies that an isentropic efficiency does not represent the real efficiency in an accurate manner. For Case 1, the maximum phase shift between the mass flow

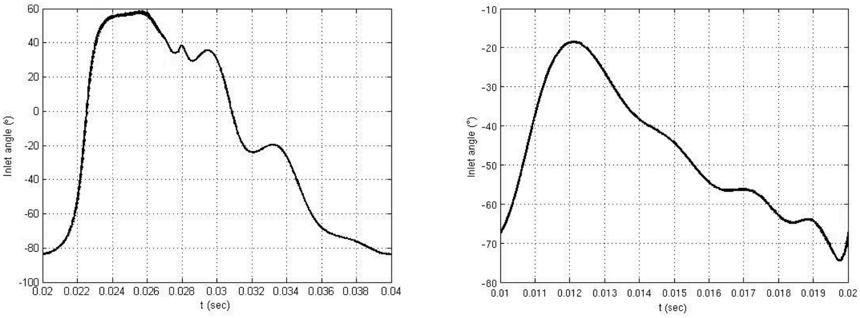

FIGURE 5.17. Relative incidence angle to the wheel for 90° azimuthal angle during one pulse. Case 1 to the left, Case 3 to right.

and the pressure is approximately 20° which occurs when the mass flow into the domain is low. When the mass flow reaches its peak, the phase shift is below 4°. For Case 3, the phase shift between the mass flow pulse and pressure at the inlet when maximum mass flow occurs is approximately 20°, which is significantly higher than for Case 1. This implies that the quasi-stationary assumption is not valid for a turbine working in pulsatile flow. The deviation from the quasi-stationary assumption also depends on that the flow separation from the turbine wheel blades is more severe during the acceleration phase as compared to the same mass flow during the deceleration phase. The deviation from the quasi-stationary approach increases with increasing frequency, which has also been reported by Wallace & Blair (1965).

When the mass flow through the turbine is low, the relative inlet angle is below -40°. This implies that the pressure is higher at the suction side of the blade tip at the leading edge, which drives the flow over the tip from the suction side towards the pressure side. This leads also to the role-up of the tip vortex at the pressure side, as shown in Figure 5.18. When the mass flow increases during the pulse, the inlet angle increases and flow separation occurs at the suction side of the blade. The vortex due to the flow separation is much stronger than the tip vortex formed at the pressure side of the blade. The tip vortex formed at the leading edge detaches and is convected downstream between the blades. Downstream between the blades, the secondary flow at high mass flow contains three different structures; the detached tip vortex from the leading edge that is convected downstream, the tip vortex that is created between the blade tip and the shroud and a vortex that is counter-rotating as compared to the tip vortices, as depicted in Figure 5.19. Between the blades, the pressure gradient drives the flow in the boundary-layer at the shroud from the pressure side

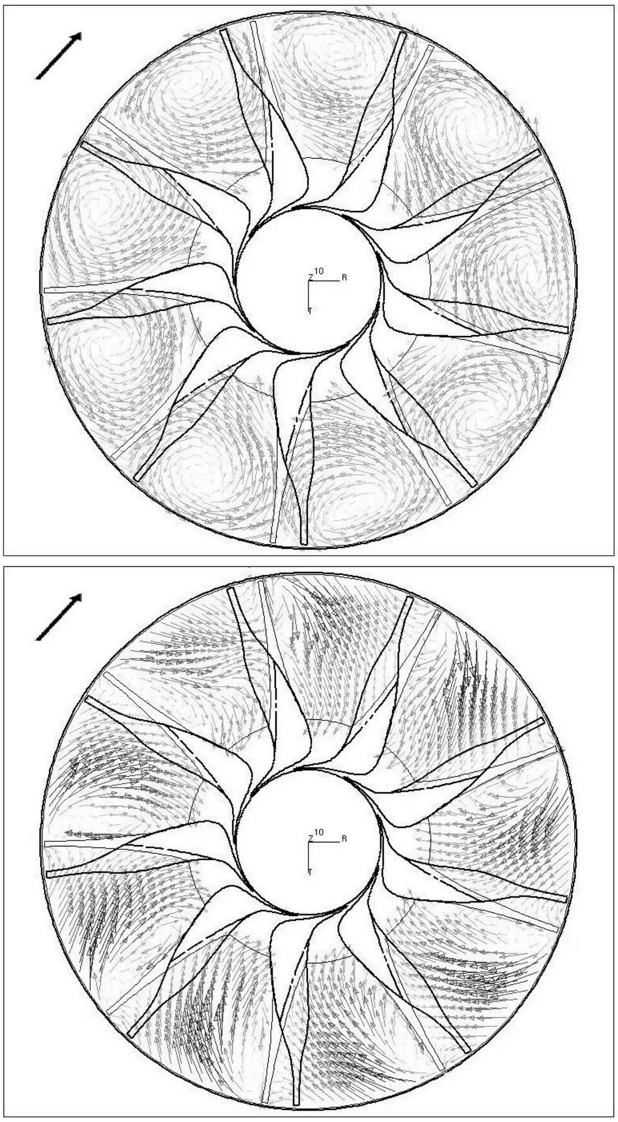

FIGURE 5.18. Snapshot of the in-plane relative velocity field at the inlet plane to the wheel, Case 1. The arrow shows the direction of rotation. The top figure shows the flow field with low mass flow through the turbine. The bottom figure shows the flow field when the mass flow through the turbine is high.

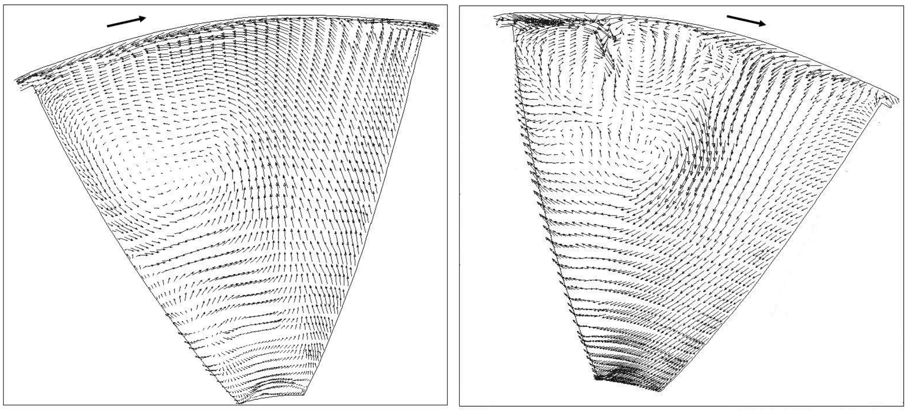

FIGURE 5.19. Snapshot of the in-plane relative velocity at a plane between the leading and trailing edge of the wheel, Case 1. The left figure shows the flow field with low mass flow through the turbine. The right figure shows the flow field when the mass flow through the turbine is high.

towards the suction side. When the flow in the boundary-layer at the shroud is affected by the strong jet that is formed at the tip, it is deflected inwards between the blades and a vortex starts to roll up.

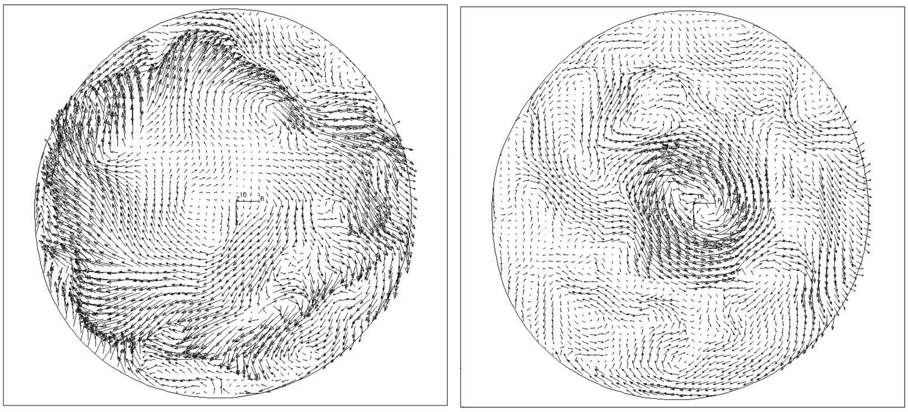

FIGURE 5.20. Snapshot of the velocity field in the diffuser, half a wheel diameter downstream of the trailing edge of the wheel, Case 1. The left figure shows the flow field with low mass flow through the turbine. The right figure shows the flow field when the mass flow through the turbine is high.

The higher mass flow at the inlet for Case 3 implies that the Mach number is higher. When the mass flow through the wheel reaches its maximum, a shock wave is formed between the leading edge of the blade and the wall at the tongue. The shock disturbs the flow, and the tip vortex at the suction side at the leading edge where the shock occurs is very strong. Since the interval when supersonic flow occurs in the volute only corresponded to a few blade passages, it does not deteriorate the shaft torque. The higher mass flow for Case 3 also results in a stronger pressure gradient between the blades which gives a higher power output. Despite the stronger pressure gradient, the tip vortices for Case 3 are not as strong as for Case 1, depending on a more optimal inlet flow angle into the wheel. Downstream of the wheel, the center line vortex has the direction of rotation opposite to direction of the rotation of the wheel when the mass flow through the turbine is high. For Case 3, this vortex is weaker as compared to the center line vortex for Case 1, due to a more favorable flow outlet angle for Case 3. When the mass flow is low for both cases, no coherent structures are observed at the center-line down-stream of the wheel, as shown Figure 5.20.

5.2.3b. *Turbine performance with realistic inflow conditions.* To assess the combined effects of pulsatile flow with strong secondary flows and skew axial velocity distribution at the inlet to the turbine, computations with a geometrical configuration consisting of an exhaust manifold and a nine-bladed radial vaneless turbine was performed. The size of the geometry is typical for an exhaust manifold and turbocharger mounted on a 2.0 liter IC engine of a passenger car.

The mass flow and temperature traces that are applied at the inlets to the exhaust manifold are taken from simulations from a one-dimensional IC engine simulation tool. In order to investigate the effects of perturbations at the inlet to turbine, the same mass flow and temperature field with a phase shift corresponding to the firing order of the engine is applied at the inlet of the exhaust manifold. The frequency of the mass flow pulses and temperature corresponding to a engine working with wide open throttle at a speed of 1500 rpm, as shown in Figure 5.21 where the mass flow traces at the respectively inlet to the manifold are plotted. Since the mass flow and the pressure at both the inlet and outlet to the turbine is highly pulsatile, the shaft torque, and hence the shaft power varies in time, see Figure 5.22. As can be seen, the maximum shaft power for each mass flow pulse is not equal, despite the fact that the same mass flow and temperature traces were applied at the inlet to the runners. This is the results of the fact that the different runners have different geometrical shapes, which create different inflow conditions to the turbine. The losses in the different runners also differ, since the lengths are not equal and the number of bends and the curvature radius of the bends differ for the different runners.

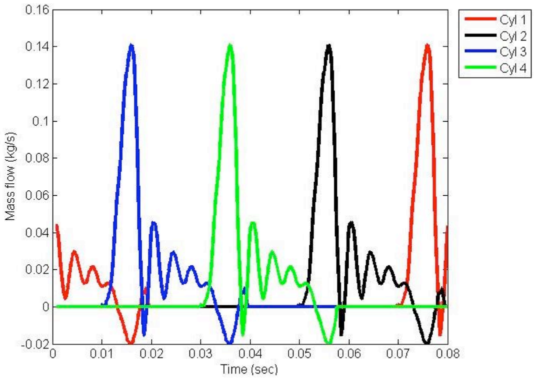

FIGURE 5.21. Mass flow at inlets to the respectively runner of the manifold.

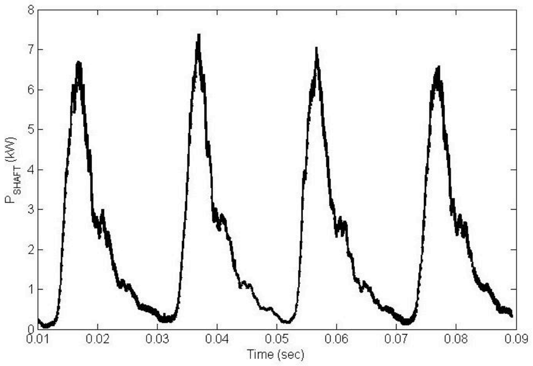

FIGURE 5.22. Shaft power during four pulses.

The peak shaft power occurs when the mass flow comes from cylinder 4, which is the runner with the longest straight section. The second highest shaft power is obtained for runner 2, which compared to runners 1 and 3, has one bend less. The lowest shaft power is obtained for runner 1, which is the runner with sharpest bends. The deviation between the lowest and highest peak in shaft power is about 11%, while the difference between the peak of the inlet pressure is about 3% and mass flow is about 4%, respectively. In Figure 5.23, the shaft power is plotted versus the mass flow and pressure respectively. As can be seen, the pressure and the shaft power are almost in phase, and from this point of view, the turbine can be treated as a quasi-stationery flow device. When plotting the mass flow versus the shaft power, one can see that the curve forms a closed envelope. The enclosed area for the operational point and geometrical configuration used in this study is smaller than the enclosed area for the corresponding case used in previous study. The phase shift, and hence the degree of quasi-stationary behavior of the turbine with respect to the mass flow, pressure and temperature at the inlet to the turbine, do not only depend on the frequency of the pulses, but also of the geometrical configuration upstream of the turbine.

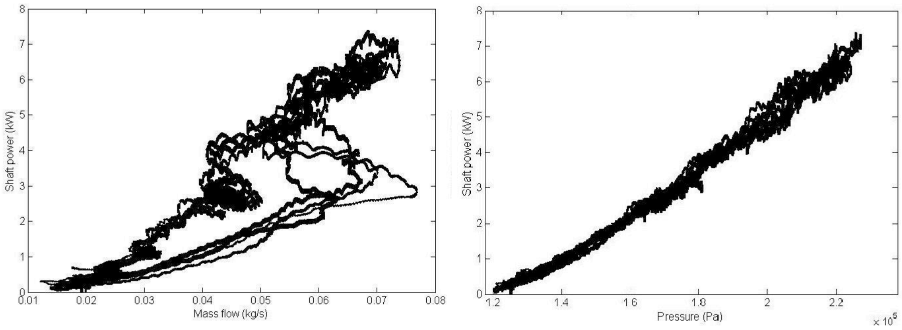

FIGURE 5.23. Shaft power plotted versus mass flow (left) and pressure (right) at turbine inlet, respectively.

It is clear that the inflow conditions into the turbine affect the performance of the turbine. One way to give a measure of the level of the disturbances of the inflow conditions is to use two different dimensionless numbers, the secondary flow index and the uniformity index. The secondary flow index is defined here as:

$$Sw = \sum_{i}^{n} \sqrt{\frac{V_i^2 + W_i^2}{U_i^2 + V_i^2 + W_i^2}} / n \tag{5.3}$$

where V and W denote the in plane velocity components and the summation is taken over the whole plane. Sw is thus a measure for the strength of the in-plane kinetic energy as compared to the total kinetic energy of the fluid. Here, we apply this definition for the inlet plane to the turbine.

The uniformity index (UI) is defined here as

$$UI = \sum_{i}^{n} \sqrt{\left[\frac{[U_i - U_{Pi}]^2}{U_{Pi}^2} \right]} / n \tag{5.4}$$

where U_P is an approximation of a velocity profile commonly used for a fully developed turbulent pipe flow. For such flows one often uses the following expression:

$$U_P = V \cdot \left[1 - \frac{r}{R}\right]^{1/N} \tag{5.5}$$

Here we take N=8 and V is the maximum velocity. V is computed so that the mass flow at the inlet to the turbine is the same for the real case and the approximated velocity profile for the pipe flow.

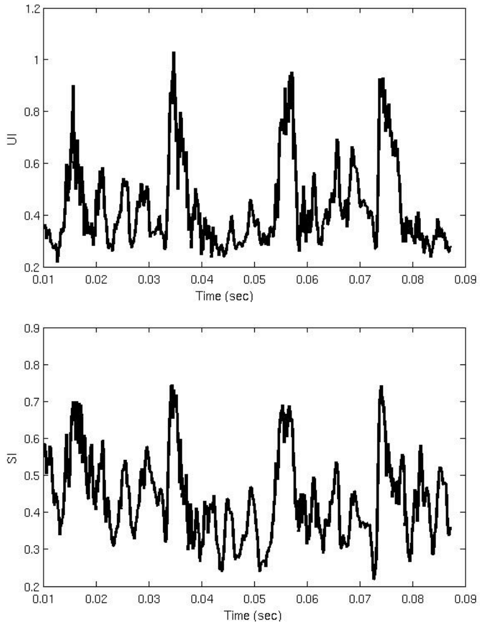

FIGURE 5.24. Upper figure: Uniformity index computed at the inlet plane to the turbine. Lower figure: Secondary flow index computed at the inlet plane to the turbine.

In Figure 5.24 the secondary flow index and the uniformity index are plotted versus time. As clearly seen, the deviation from a pure axial flow increases with increasing mass flow. It can also be noted that the different runners give different strength of secondary flow structures. The strongest secondary flow index is obtained for runners 1 and 4, which are the runners with the most curved bend upstream of the turbine inlet. These secondary flow structures are combinations of Dean vortices and a swirling motion which are created in the bends of the manifold. The strength of these structures varies during the pulse. The width of the peaks in secondary flow index for runners 2 and 3 is broader as compared to runners 1 and 4. This aspect is due to the fact that these runners are shorter, which leads to less dissipation of secondary flow structures. The axial velocity profile deviates from a “pipe flow profile” due to the bends located upstream of the turbine, whereby one can observe higher axial velocity in the outer part of the bend outlet. As seen also in Figure 5.25, there are regions with high velocity near the walls. Even though the differences in swirl and uniformity index for the four runners are not large, yet these indices correlate well with the instantaneous shaft power: i.e. runners which give the largest instantaneous index (runners 1 and 4) also give the highest instantaneous shaft power. However, it is not enough to assess only the peak values of uniformity and swirl indices but one has to consider also the duration (or rather the integral of the index over time). It must also be emphasized that the mass flow, pressure and temperature trace (which give the available energy) are not the same for the four pulses assessed.

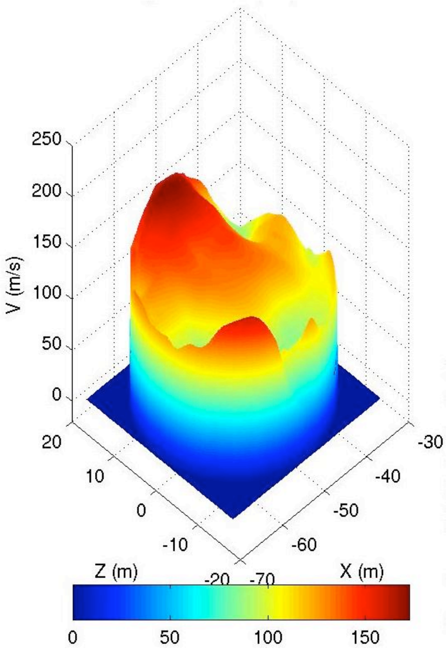

Figure 5.25. The axial velocity component at the inlet plane to the turbine at an instance with high mass flow rate.

The axial velocity distribution in the volute becomes more uniform when it is convected downstream, but still, far away from the most beneficial velocity distribution in the volute. The axial and secondary flow disturbances, in combination with the pulsatile flow, affect the relative flow incidence angle into the turbine wheel. For the operational point assessed in this study, the incidence angle varies from 60° to -90° during four pulses, which gives further incidence losses. At low mass flow rates, the relative incidence angle is less than -45°, which results in a weak vortex at the pressure side at the leading edge of the blades. When the mass flow is increasing, the relative incidence angle is increasing, and at high mass flow rates, the flow separates at the suction side of the leading edge. At high mass flow rate, the vortices created at leading edge are stronger than the vortices at low mass flow rates. These vortices created at the leading edge are convected downstream in the wheel, and at high mass flow rates, these vortices interacts with the blade tips vortices, and forming a strong structure with low axial velocity in the middle. The mechanisms for these structures are the same as described in previous sections.

5.2.3c. *Effects of heat transfer at the walls.* To assess the effect of heat losses at the turbine housing during pulsatile flow, two different cases are considered; one with adiabatic walls and a second with fixed wall temperature. For both cases, time resolved temperature and mass flow traces are applied at the inlet of the turbine. The inlet conditions are the same one as depicted in the left figure in Figure 5.15. For the case with heat transfer, the temperature at the volute wall is set to 823°K and the temperature at the diffuser wall is set to 726°K, as depicted in Figure 5.26. These temperatures were determined from measurements of an equivalent turbine working at approximately the same operation point. The turbine wheel wall is assumed to be adiabatic, since there is gas in the region between the wheel and back plate, but this cavity is not modeled in this study.

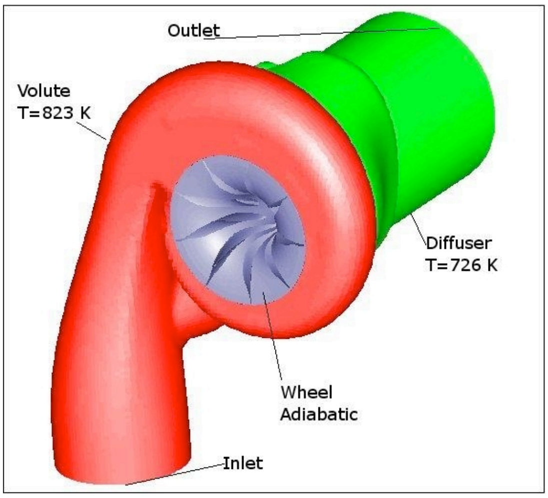

FIGURE 5.26. The applied wall temperatures for the non-adiabatic case.

The differences for the shaft power between the two cases are very small and in the same order as the numerical uncertainty. The difference in pressure ratio over the turbine is also small. The global parameters that differ are of course the heat losses at the walls and the outlet temperature. The instantaneous heat transfer from the walls at certain times is as high as the shaft power, see Figure 5.27. The time mean shaft power during one pulse is 3.66 kW for the case with heat transfer and 3.71 kW for the case with adiabatic walls. This gives that time mean heat losses are as large as 59% of the delivered shaft power for this case. This is due to the fact that the shaft power is very low during larger portion of the pulse, while the heat transfer is not. However, since the shaft power and heat transfer at the walls are much smaller than the instantaneous enthalpy at the inlet and outlet, the heat losses have only a small affect on the shaft power. The temperature difference at the outlet of the turbine depends only on the heat losses at the walls, since the shaft power is the same. The isentropic power for the different case are integrated over one pulse, and the time mean efficiency for the case with heat transfer is 61% and for the case with adiabatic walls it is 63%, respectively.

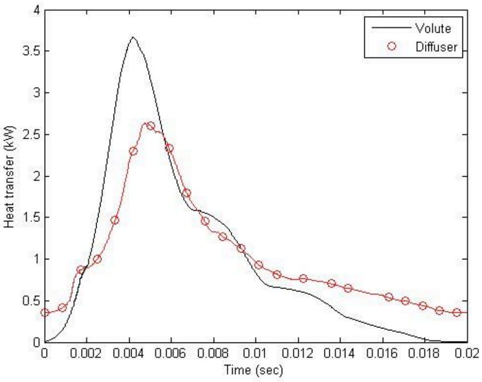

FIGURE 5.27. The heat losses from the volute and diffuser.

In the volute, a thin thermal boundary layer is formed near the walls for the case with non-adiabatic walls, and the temperature in the bulk flow in the volute does not differ between the two cases. In the diffuser, the temperature differs significantly between the cases. This is of course due to the character of the heat transfer in the volute and diffuser. Also, all flow structures created in the wheel effectively mixes the warmer gas from the bulk flow with the colder gas from the thermal boundary layer for the case with non-adiabatic walls, which ends up in the relative large temperature difference in the diffuser. The vortex structures created in the diffuser captures hot gas from instants at high mass flow rate, which results in a higher heat transfer from the diffuser compared to the volute during instants with low mass flow rate, as can be seen in Figure 5.27.

5.2.3d. *Comparison of results from 1-D and 3-D computations.* In this study the results from 1-D and 3-D simulation are compared to assess some of limitations in the 1-D approach (Hellstrom *et al.* (2010)), namely those related to the secondary flow. Three different cases are considered with different complexity of the geometry, and in the 1-D simulations, the turbine performance is based on measured turbine maps. The 3-D results are from the computations analyzed above, and the boundary conditions to the 1-D simulations are from the 3-D simulations to ensure that the same mass flow, temperature and pressure is specified at the respectively inlet and outlet. The results show that the RMS values of the deviation of the shaft power from the 1-D and 3-D are almost as large as the predicted shaft power. When comparing the time resolved data, the largest deviations occur at instants at low mass flow rates. At low mass flow rates, the turbine operates in a region where no measured points are available in the turbine map and the used data in the 1-D simulation for this region is extrapolated. This shows that the extrapolation routines in the 1-D must be improved or that the ability of measuring the turbine map over a wider range in gas stands must be enhanced. Also, at low mass flow rates, the bearing losses cannot be neglected, and hence the experimental data include these, making direct comparison with computations more difficult. Since the predicted shaft power differ, the temperature at the outlet of the turbine also differ, since the different modeling approaches do not extract the same amount of energy out of the gas. The results also indicate that it is important to incorporate the energy of the secondary flow in the 1-D energy equation to predict the correct temperature. One way to improve the results is to extend the map with data from 3-D simulations. In this study, an improvement in predicted pressure ratio was achieved with the extended map, while the improvement in predicted shaft power was less good. The latter is due to the assumptions in the 3-D modeling and that the bearing losses are not included in 3-D results, while they are included in the measures turbine map. Yet, the results show that 3-D CFD can be used to extend the range of turbine maps whereby improving the 1-D simulations results.

5.3. Unsteady flow in a radial compressor

The objective with this part of the work has been to assess the flow field in a radial compressor operating close to surge (Paper 8), so as to investigate the mechanism that drives the unsteadiness in the compressor. An operational point far from surge is also considered to be able to assess the flow field under more optimal operational conditions (Guillou *et al.* (2010*a*) and Guillou *et al.* (2010*b*)).

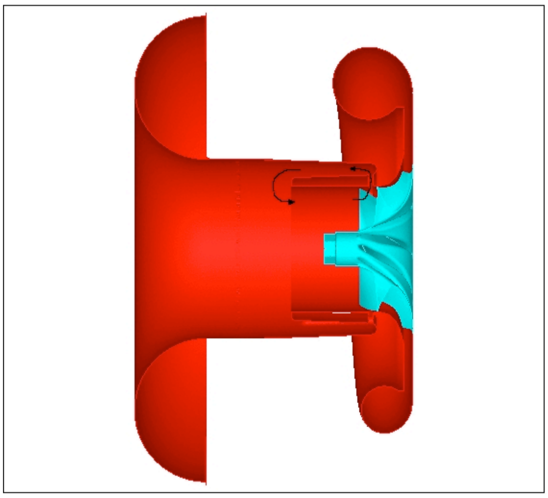

FIGURE 5.28. The geometry of the compressor. The arrow in the figure shows the recirculation flow in the ported shroud.

5.3.1. *Methods and computed cases*

As for the turbine computations the LES approach has been used. The second order MARS scheme has been used for spatial discretization of the convection terms. For the temporal discretization, a formal second order Crank-Nicholson scheme was used. A modified version of the PISO solver has been used to solve the equations at each time-step, where the number of corrector stages is determined by the convergence criteria. Rotating Reference Frame (RRF) handles the rotation of the wheel. In the RRF concept, the momentum equation is modified to take into account the Coriolis and centrifugal forces by adding the appropriate source terms. Since source terms are added to the governing equations, no mesh motion is required, and this technique is also known as the frozen rotor approach. This approach is not as computational expensive as the sliding mesh technique, where the wheel is actually rotating relative to the stationary compressor housing. The drawback is that the blade passage effects are not captured and the position of the non-rotating wheel relative to the tongue may influence the results, but data from measurements yields that the dominating frequencies of the perturbations are much lower than the blade passage frequency, which then implies that the RRF technique can be used.

A ported shroud compressor of the Honeywell GT40 turbocharger (Figure 5.28) has been studied. The ported shroud is a design feature that is used to extend the operational range of the compressor by increasing the surge marginal. The ported shroud recirculates air from the wheel through a slot and then back to the inlet region, as depicted in Figure 5.28, in order to suppress surge. For the studied compressor, the ported shroud consists of four channels with supporting legs in between each channel. Due to vibrations, the cross section area of the four ported shroud channels is not the same. The compressor wheel has 10 blades with an exducer diameter of 88 mm. This turbocharger is suited for heavy truck engines to deliver power ranged from 400 to 850 kW.

Since one of the objectives with this study is to compare the computational results with experimental data, the same inlet configuration with a bell mouth is used in the computations. To avoid effects of the inlet boundary and to reproduce the inlet condition of the experiment, the mesh at the inlet region is extruded to a half sphere. Two different operational points have been considered, one close to surge and one far from surge. At the inlet to the compressor, the mass flow rates and temperature are specified (see Table 6), while at the outlet a constant pressure is applied. For both considered operational points, the rotational speed of the wheel is specified to 64 000 rpm.

TABLE 6. Compressor parameters for the considered operational points

Case	Mass flow at inlet (kg/sec)	Temperature at inlet $^\circ C$	Pressure at outlet (kPa)
Close to surge	0.105	23	165
Far from surge	0.27	23	156

5.3.2. *Comparison of computed and measured data*

Computed global data, such as pressure ratio and efficiency is compared with measured data for the same compressor. The measurements have been performed using the turbocharger test rig in the Gas Dynamics and Propulsion Laboratory (GDPL) at the University of Cincinnati. For the computations, the area-averaged outlet pressure and temperature are calculated at 300 mm

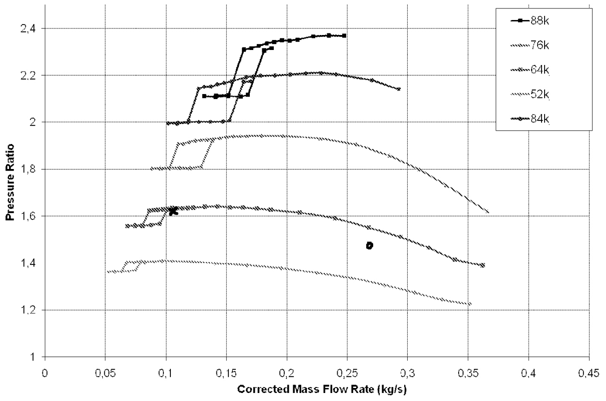

FIGURE 5.29. The measured compressor map with the two computed operational point marked by X and O.

downstream of the volute outlet, which is at the same location where the pressure has been measured in the experiments. The area-averaged inlet pressure is calculated at the inlet boundary.

In Figure 5.29 the computed operation points are marked by X and O and the pressure ratio, outlet temperature and efficiency is summarized in Table 7. The agreement between the computed and experimental pressure ratio is very good for the operational point close to surge. The discrepancy between the measured and computed temperature and efficiency is much larger, where the efficiency is defined as:

$$\eta_C = \frac{(p_{02}/p_{01})^{\frac{\gamma-1}{\gamma}} - 1}{(T_{02}/T_{01} - 1)} \tag{5.6}$$

Since the Mach number at the both inlet and outlet is relatively low, it is assumed that the total pressure and temperature are the same as the static, and therefore the static inlet and outlet pressure and temperature are used to compute the efficiency. In the computations, the walls are modeled as being smooth and adiabatic, implying that the outlet temperature should be higher than the measured. The modeling of the wheel with the RRF technique and the fact that the space between the back plate and the wheel is neglected are likely to result in a lower outlet temperature, because the rotation of the wheel yields viscous losses and a lower efficiency. Sun *et al.* (2009) performed numerical computations for a radial compressor with and without modeling the space between the back plate and the wheel, and showed that the efficiency is

Table 7. Measured and computed data

	Pressure ratio (-)	Outlet temperature $^\circ C$	Efficiency (-)
Measurements	1.63	108	0.55
CFD	1.60	92	0.60
Measurements	1.56	354	0.73
CFD	1.45	348	0.68

higher for the case in which the region between the wheel and back plate was neglected.

For the operational point far from surge, the pressure ratio from the computations deviates from the measured one. The computation gives a lower pressure ratio for a given mass flow rate compared to the measured data. The difference in pressure ratio is approximately 7%. The accuracy of measured mass flow is estimated to 10%, and for this speed line, an uncertainty of 10% in the measured mass flow rate means that for this operational point, the pressure ratio can vary between 1.58 and 1.50, which means that the computed pressure ratio is almost in the uncertainty range. Since the pressure ratio and outlet temperature are not the same in the measurements and computations, the efficiency will also deviate.

5.3.3. *Flow field for an operational point close to surge*

In this sub-section, only the unsteady flow is discussed. For details about the time mean averaged flow, see Paper 8. The instantaneous flow varies with time, since the computed operational point is close to surge. Spectral analysis of the temporal variation of the area averaged pressure (shown in Figure 5.30) in a plane located in the outlet pipe downstream of the volute, yields dominant frequencies of 120 Hz and 200 Hz. The mass flow through the same plane has a temporal variation with a dominant frequency of 120 Hz. The area averaged pressure at a plain crossing the inlet region between the bell mouth and the wheel also shows a time variation of 120 Hz, while the mass flow through the same plane varies with a frequency of 200 Hz. Also, the area averaged pressure at the different ported shroud channels varies with a dominating frequency of 120 Hz, while the frequency of the mass flow coming out of the ported shroud channels is not well defined.

In the inlet region of the compressor (defined as the area between the bell mouth and the leading edge of the wheel, see Figure 5.31), the flow is unsteady

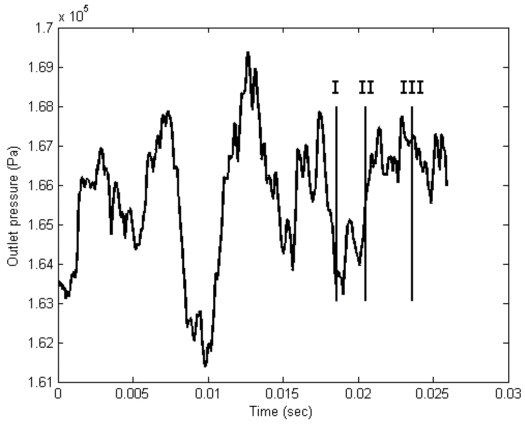

FIGURE 5.30. The area averaged pressure in the outlet pipe at a position between the volute and the outlet boundary.

and non-uniform in the circumferential direction. The reversed flows from the wheel region and from the ported shroud channels convect structures created in the wheel and ported shroud channels. When the back-flow interacts with the core flow, strong shear layers are formed and new structures are created and convected back into the wheel. The flow field in the wheel consists of several different coherent structures. At leading edges near the hub side, horseshoe vortices are formed at certain time instants and blade tip vortices can clearly be seen. At the leading edges, vortices are formed along the flow separation zones on the suction side of the blades. The extent of flow separation at the leading edges of the blades varies with varying inflow conditions. Also, in blade passages whose outlets are located where back-flow occurs in the diffuser, many turbulent structures are formed.

Back-flow occurs at the regions in the diffuser where the pressure is high and the velocity is low. At some instances and locations in the diffuser the flow is totally reversed while at other instants the flow in the same region is only partially reversed. At locations with a fully reversed flow, the radial pressure gradients are strong, such that the pressure at the outlet of the wheel is high, and at these blade passages, strong back-flow occurs from the inlet region of the wheel to the inlet region of the compressor.

Since the pressure field in the diffuser and volute varies in time and space, the flow in the diffuser and volute is unsteady. In Figure 5.32 the pressure and velocity distributions in the diffuser and volute (denoted as plane C in Figure 5.31) are depicted at three different time instances. The time of these different instances are marked by lines in Figure 5.30 and are denoted I, II and III. The regions with high velocity correspond to locations where the radial pressure

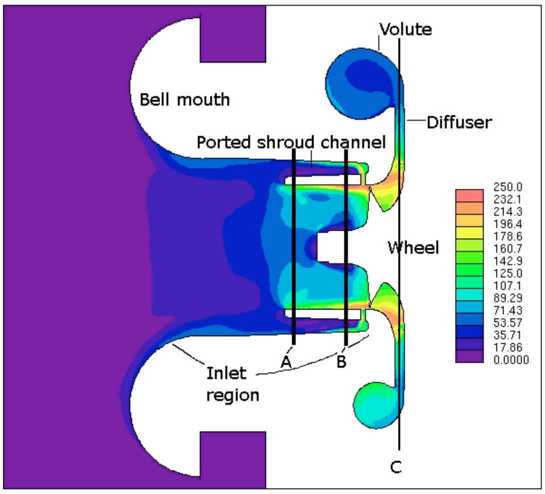

Figure 5.31. Time mean velocity magnitude in a plane passing along the axis of the shaft.

gradient is lower. The pressure and velocity fields are rotating in the clockwise direction, which is also quantified by correlating pressure signals from different positions around the volute (see Paper 8). However, the rotational speed of the pressure field is not constant and the region with lower pressure remains somewhat longer at approximately three o'clock due to the recirculation zone downstream of the tongue. At the tongue, the flow splits and while a certain part exits through the outlet pipe, the other part flows back into the volute. This leads to increased losses in the volute compared to operation at higher mass flow rates (Gu *et al.* (2001)). Downstream of the tongue, an unsteady recirculation zone is created at certain time instances depending on if the pressure gradient is adverse or favorable. The extent and strength of recirculation zone varies with time, and at some instances, vortex structures are released from the flow separation zone and are convected downstream in the volute.

At different positions in the computational domain, probes are located to monitor the pressure and velocity. These time-resolved signals can be used to analyze the behavior of the flow at these locations. The frequency spectra are analyzed. However, the relatively small number of statistically independent samples limits the accuracy in resolving low frequencies. Therefore, frequencies below 100 Hz are not considered, and the results for frequencies below 300 Hz are less accurate. In the inlet region, no dominant frequencies can be identified in the pressure spectrum signifying that the amplitude of the pressure perturbations is small. Analysis of velocity signals in various positions in the inlet region shows a frequency of 180 Hz in the axial component. The perturbations

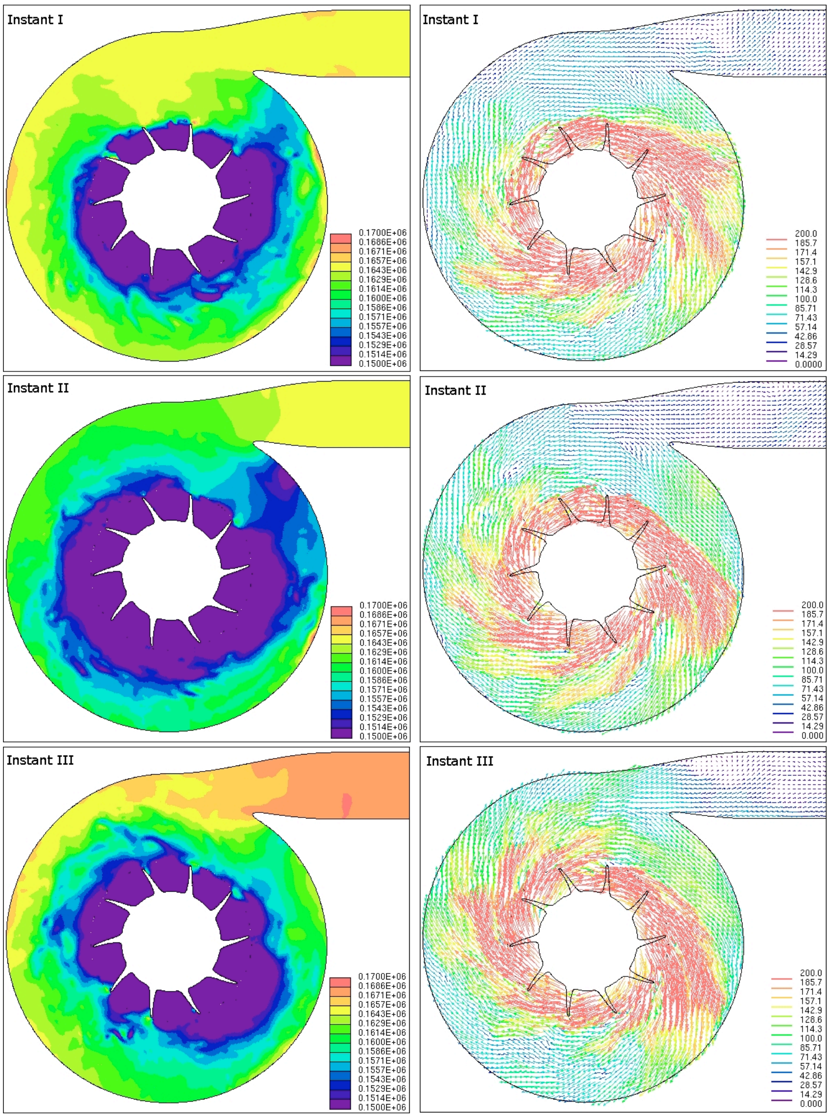

Figure 5.32. Snapshots of the pressure and velocity field in the diffuser (Plane C) at three different time instants.

at a frequency of 180 Hz stems from pressure fluctuations in the diffuser and volute, which cause back-flow in the diffuser and in some blade passages. This means that reversed flow with this frequency is coming out through the ported shroud channels and the wheel, creating flow fluctuations in the inlet region of the compressor. Within the wheel, different frequencies can be found, depending on the location, but all signals (p, U, V, W) have peaks in the range of frequencies between 120 Hz to 500 Hz. The streamwise velocity component and pressure signal have a peak at 180 Hz. The dominant frequency of the pressure fluctuations in the volute is 300 Hz. Also, peaks at 120 Hz and 180 Hz are present in spectra. The 180 Hz and 300 Hz are also present in the spectra of the velocity signals from probes located in the volute. The length of the volute is approximately 0.55 m, and the mean convective speed in the volute is approximately 105 m/s yielding a frequency of 190 Hz. This could indicate that the frequency of 180 Hz corresponds to convection of velocity perturbations along the volute. Guo *et al.* (2007) concluded from a numerical study that pressure oscillations in the volute develop into a standing wave because the volute acts as a closed pipe that amplifies the flow unsteadiness. In the present study, with the given length of the volute and a speed of sound of approximately 380 m/s, a quarter wave pipe assumption yields a frequency of 172 Hz. It is proposed that the flow unsteadiness created at the tongue and then convected around the volute is amplified by the standing pressure wave in the volute. The 300 Hz peak frequency is likely related to the pressure perturbations that are created by the recirculation zone at the tongue, since the 300 Hz peak is stronger in spectra at locations near the tongue.

No evidence has been found as to where and what mechanism is responsible to initiate this unsteadiness. It might be a structure from the inlet region of the compressor that disturbs the flow in the diffuser and volute, and then creates the unsteady separation zone at the tongue. The perturbation might also come from the diffuser and volute.

5.3.4. *Flow field for an operational point far from surge*

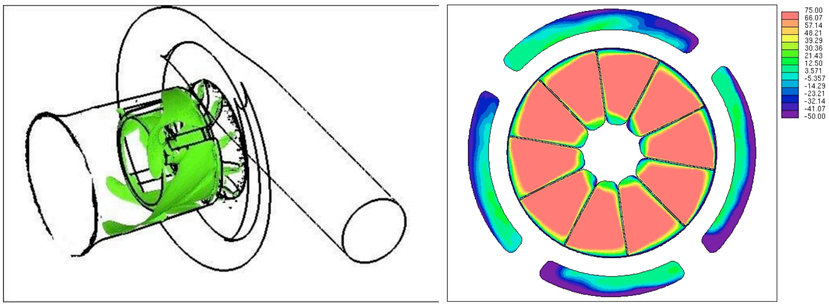

FIGURE 5.33. Iso-surface of negative axial velocity and axial velocity distribution in the inlet region of the wheel.

For the stable operational point, back-flow also occurs in the inlet region of the compressor, as depicted in Figure 5.33. No flow comes out from the wheel as it does for the operational point close to surge. Back-flow can only be seen to exit from the four ported shroud cavities and not uniformly; more flow is coming out of the "right" cavity. The flow from this cavity has higher momentum compared to the one from the other cavities. The total mass flow rate coming out from the ported shroud channels is approximately 0.025 kg/sec, which is approximately 10% of mass flow rate through the compressor. The cross section area for the four ported shroud channels is not the same, and almost 40% of the total mass flow rate from the ported shroud channels comes from the channel with the largest cross section area, which is the right channel. The backward flow region also enters further upstream from this cavity.

As seen in the iso-plot in Figure 5.33, the reversed flow has a clear helical shape. This is due to the fact that the flow entering the ported shroud through the slot is weak in the radial direction but has a strong circumferential component from the rotation of the wheel. This implies that a swirling motion is created in the ported shroud. The flow in the slot is not axisymmetric. More flow is entering in the upper right section of the slot as depicted in the cross sectional plot of 5.34. This yields more flow exiting from the "right" cavity. This asymmetry is due to the non axisymmetric pressure distribution into the cavities. Further upstream, closer to the blade leading edge, the pressure distribution is almost symmetric in the circumferential direction, which means that the non-uniform pressure distribution in the slot is an effect of either the geometrical shape of the ported shroud, or the pressure distribution further downstream. In the wheel, strong tip vortices are created on the low pressure side of the blade tips, and in the core regions of these vortices reversed axial flow occur due to the pressure gradient. The majority of these regions of

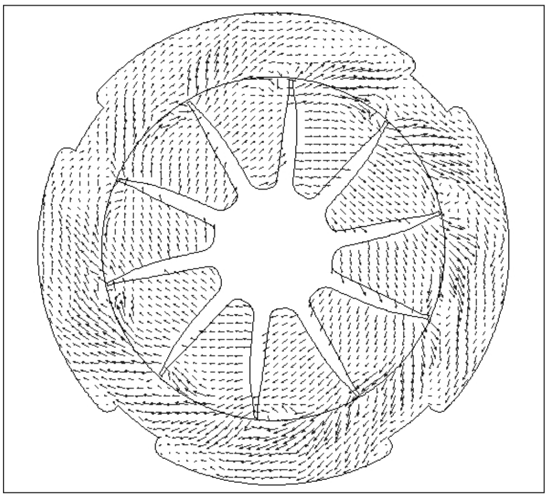

Figure 5.34. Cross-section of the in-plane velocity component into the ported shroud slot

reversed flow are then convected into the slot to the ported shroud channels, and upstream of the leading edge of the blades, no back flow occurs. No flow separation occurs in the diffuser, even though the flow in the wheel is unsteady with reversed flow structures. Downstream of the diffuser and volute, the flow has a strong swirling motion, where the velocity magnitude of the swirling component is at least as strong as the axial component.

CHAPTER 6

Summary and conclusions

The unsteady flow in pipes, a radial turbine and a centrifugal compressor have been computed by using LES. The purpose of the pipe flow computations was to study the non-pulsatile and pulsatile internal flow in curved geometries, which are relevant to the inlet to the turbo-charger turbine. For one of the used geometries, a comparison with measured data has also been performed. The results show that an Implicit LES turbulence modeling approach gives the best agreement with measured velocities among the tested turbulence modeling approaches. For the pulsatile flow a phase shift between the pressure and the bulk flow has been found. The phase shift varies during the pulse, depending on the balance between the different terms in the momentum equation. The phase shift also implies that flow in the boundary layer and in the core region of the pipe are out phase, since the low momentum flow in the boundary layer is more sensitive to changes in the axial pressure gradient than the flow in the core region. The bends in the pipe introduced secondary flow structures. In the first bend, two counter-rotating vortices are created and the axial velocity component after the bend is not uniformly distributed. When this non-uniform axial velocity distribution enters a second bend, situated in an orthogonal plane downstream of the first bend, a swirling motion is created downstream of the second bend. This swirling motion is also affected by the Dean vortices created in the bends upstream. Since an exhaust manifold can be viewed as being composed of straight and bent pipe sections, the flow into the turbine has non-negligible secondary flow structures in addition to the pulsatile axial flow. This implies that a turbocharger turbine for an IC-engine will have operation conditions that are far away from the conditions that they are used in normal tests i.e. steady state flow in a gas stand.

To assess the influence of different modeling approaches on the predicted turbine performance a study with different modeling strategies was performed. The different turbulence modeling strategies were the RANS (k-ϵ based model) and LES approaches and two different ways of modeling the rotation of the wheel; Rotating Reference Technique (also known as the frozen rotor technique) and Sliding Mesh technique was used. The computed data was compared to measured turbine performance and the LES together with the Sliding Mesh technique showed the best agreement with the measured performance. The deviation between measured and computed shaft power is less than 6%. In the case where URANS was used together with the Sliding Mesh technique the shaft power fluctuated with a large amplitude, due to pressure waves in between the blades. The pressure fluctuations from the tongue interact with the modeled turbulence, which then amplifies the perturbation, and pressure waves are created in the wheel.

To investigate the effects on the turbine performance due to secondary flow structures created in for example the manifold upstream of the turbine, computations with different types of perturbations at the inflow to the turbine have been carried out. The results show that both small and large scale perturbations at the inlet to the turbine affect the shaft power. The undisturbed inlet profile gives the best power output from the turbine while a case with strong swirl in combination with 3-dimensional turbulent perturbations gives the largest loss in the shaft power output. The deterioration of the performance is due to large scale structures created in the volute, which then result in unfavorable inlet conditions into the wheel.

The effect of the pulsatile flow on the turbine performance has been assessed by conducting computation at different frequencies and mass flows rates. When plotting the mass flow versus the shaft power a closed loop is formed, where the shaft power is lower during the acceleration phase of the mass flow compared to deceleration phase. The incidence angle of the flow into the wheel has large variation during the pulse which affects the shaft power output and the efficiency of the turbine. A deviation from the optimal angle results in strong tip vortex at the leading edge of the blade, which detaches and is convected downstream and affecting the axial velocity in between the blades. The results also show that the turbine cannot be treated as being quasi-stationary when working in pulsatile flow, due to inertia of the system, detached flow during the acceleration phase and a non-constant phase shift between the pressure, mass flow and shaft power. The deviation from the quasi-stationary approach increases with increasing pulsation frequency.

The combined effects of pulsatile flow, secondary flow components and a non-uniform axial velocity component were assessed by considering a case with an exhaust manifold mounted upstream of the turbine, where pulsatile mass flow traces were applied at the inlet to the respectively runners. The geometry upstream of the turbine has a large effect on how the turbine behaves. The shaft power is almost a linear function of the pressure at turbine inlet, which it was not for the cases where pulsatile inflow conditions were applied direct at the turbine inlet. This probably due to the effect of the manifold acting as a reservoir, which damps the pressure pulses and reduces the instantaneous mass flow through the turbine. The turbulence levels are also higher resulting in a lower phase shift. The results also show that the mass flow rate into the turbine is affected by the manifold. The disturbances created in the manifold are damped in the volute, causing a substantial pressure drop at high mass flow rates. Nevertheless, the flow in the volute is not uniform, which causes strong non-uniformity in the flow into the wheel. A correlation between the strength of the disturbances of the inlet flow to the turbine and the turbine performance was noted.

To study the effects of heat transfer at the walls on the turbine performance working under pulsatile flow conditions, two different cases were considered; one with adiabatic walls and another with heat transfer at the walls. The results show that the external heat transfer has a small effect on the turbine performance for the considered operational point. The parameter that differs is the time resolved temperature at the outlet, which is lower for the case with non-adiabatic walls due to the heat-losses.

The flow in a ported shroud compressor has also been computed with Large Eddy Simulation for two different operational points, one close to surge and one far from surge. Global data, such as pressure ratio for a given mass flow rate is compared with measured data for the considered geometry, and the agreement is good for the operational point close to surge. For the operational point close to surge, the results show that the flow is highly unsteady with reversed flow in the inlet region, wheel and diffuser. The analysis of the flow field, the frequency analysis and the cross-correlations show that the driving mechanism behind the unsteadiness is related to the tongue, where the flow separates at some instances depending on the local pressure gradient at that location. A region with low pressure and high velocity is rotating around in the diffuser and the volute. At locations with strong radial pressure gradient in the diffuser, the velocity is reversed, causing strong reversed flow in the neighboring blade passages and further upstream in the inducer region and into the ported shroud channels. In the shear layer between the back-flow and the bulk flow in the inlet region of the compressor, structures are created and then convected into the wheel. This can most probably be avoided by a better design of the ported shroud channels by guiding the back-flow back in the main stream direction, which then most probably should improve the inflow to wheel which then improves the efficiency of the compressor. Due to the complex unsteady flow at this operational point, it is impossible to determine what the mechanism is that starts the unsteadiness. It might be started in the inducer region, since the flow entering the wheel is varying in both time and space due to structures created in the compressor inlet region by the reversed flow from the ported shroud. The instability might also start in the diffuser, due to structures created in the wheel (tip vortices, recirculation zones at the leading edges, and horseshoe vortices) or separation at the tongue region.

The main achievements that are presented in this thesis can be summarized as follows:

- *Detailed analysis of turbine flows:* By using LES it was possible to pinpoint the unsteady characteristics of the flow in the turbine, the importance of inlet conditions and the effects of the exhaust manifold of the IC-engine.
- *Determining boundary conditions effects on the turbine:* Turbine performance is strongly affected by perturbations and unsteadiness of the inflow conditions. It is less affected by heat-losses at the housing walls
- *Analysis of quasi-stationary flow assumption in IC-engine gas management:* By comparing LES with URANS and 1D modeling deeper understanding of the flow is possible. Validity of simplified assumptions strongly depends on the particular geometry and flow conditions.
- *Analysis of mechanisms at stall and surge:* Pioneering work of LES of a turbocharger compressor and comparison with PIV data. One of the mechanisms that yields flow unsteadiness in a ported shroud compressor is the unsteady separation bubble at the tongue of the compressor. Other mechanisms are also possible and require further study.

6.1. Suggested future work

The work related to the turbine so far has been limited to a single case. For assessing the quality of the results one has to repeat the computations for the whole turbine including inlet manifold on refined grids. One would like to improve the spatial resolution in general and of the tip area in particular in addition to near wall regions. One may expect that the lack of near wall resolution on the blade may lead to under-estimation of the separation regions and thereby also some viscous losses. One may also expect that the separation bubbles are unsteady. Such unsteadiness can act as an acoustic source and may act as a dynamic flow regulator.

Two major challenges in integrating the turbocharger into an IC-engine system are the inherent driving flow unsteadiness and the effects due to the exhaust manifolds. The former issue requires a better understanding of the flow and how steady-state gas stand data could be utilized for unsteady flow conditions. The latter issue is related not only on geometrical effects but also to sensitivity of the flow to imperfection in geometry (shape, thickness, mounting). Currently, no such knowledge exists. To address such issues one has to carry out many more LES computations and develop tools for handling efficiently uncertainties in the problem parameters (boundary conditions, geometry and physical properties).

Surge of compressor is an intricate phenomenon where more than one mechanism interact with each other. Hysteretic effects make the problem more difficult for numerical treatment. The compressor operates at transonic regime which is highly non-linear and sensitive to perturbations. Thus effects of shocks and shock-boundary-layer interaction should be addressed in some detail. Equally, the fact that the pressure ratio is very weakly dependent on the mass flow, in a rather wide range of flows, makes the computations more sensitive to uncertainties and inaccuracies which require further careful and detailed studies so as to ensure high fidelity numerical simulations.

CHAPTER 7

Papers and authors contributions

Paper 1

Numerical computations of steady and unsteady flow in bended pipes.
F. Hellstrom & L. Fuchs.
AIAA 2007-4350, 37th Fluid Dynamics Conference and Exhibit, Miami Fl. 2007

The purpose of this work is to investigate the non-pulsatile and pulsatile flow in bent pipes. The results from one of the cases with different turbulence modeling approaches are compared with measured data. A study of the influence of perturbations at the inlet is also performed. The work was performed by Hellstrom under supervision by Prof. Fuchs. The results were presented at the 37th Fluid Dynamics Conference and Exhibit, Miami, Florida, 2007 by Hellstrom.

Paper 2

Numerical computations of pulsatile flow in a turbo-charger.
F. Hellstrom & L. Fuchs.
AIAA-2008-735, 46th Aerospace Sciences Meeting, Reno, 2008.

The objective of this work is to assess the effect of different pulsatile inlet conditions on the turbine performance. Therefore three different cases with different frequencies and mass flow pulses are considered. The performance of the turbine for the non-pulsatile computations is also compared with measured performance for the same geometry. The work was performed by Hellstrom under supervision by Prof. Fuchs. The results were presented at the 46th Aerospace Sciences Meeting, Reno, 2008 by Hellstrom.

Paper 3

Effects of inlet conditions on the turbine performance of a radial turbine.
F. Hellstrom & L. Fuchs.
ASME Turbo Expo 2008: Power for Land, Sea and Air June 9-13, 2008, Berlin, Germany.

In this paper the effect of the different perturbations on the performance of a radial nozzle-less turbine is assessed and quantified by using Large Eddy Simulations. Five different cases are considered, where the base case has a non-disturbed velocity profile applied at the inlet. The other cases have 3-dimensional turbulence added to the velocity profile. Three of the cases have also different secondary flow structures added at the inlet. The turbine performance is compared for the different cases and the flow field is investigated to give a better insight into the unsteady flow field and the effects from the different inlet conditions. The work was performed by Hellstrom under supervision by Prof. Fuchs. The results were presented at ASME Turbo Expo 2008: Power for Land, Sea and Air, June 9-13, 2008, Berlin, Germany by Hellstrom.

Paper 4

Numerical computation of the pulsatile flow in a turbocharger with realistic inflow conditions from an exhaust manifold.
F. Hellstrom & L. Fuchs.
ASME Turbo Expo 2009: Power for Land, Sea and Air June 8-12, 2009, Orlando, Florida.

The combined effect of different secondary perturbations at the turbine inlet and the pulsatile flow on the turbine performance was assessed and quantified in this paper. The considered geometry consisted of an exhaust manifold and a radial turbine. The flow entering the turbine was strongly disturbed, resulting in a perturb inlet flow to the wheel which affects the shaft power output from the turbine. The work was performed by Hellstrom under supervision by Prof. Fuchs. The results were presented at ASME Turbo Expo 2009: Power for Land, Sea and Air June 8-12, 2009, Orlando, USA by Hellstrom.

Paper 5

Heat transfer effects on the performance of a radial turbine working under pulsatile flow conditions.
F. Hellstrom & L. Fuchs.
48th AIAA Aerospace Sciences Meeting Including the New Horizons Forum and Aerospace Exposition 4-7 January 2010, Orlando, Florida .

In this paper, the effects of heat transfer at the walls on the turbine performance working under pulsatile flow conditions. Two cases are considered, one with adiabatic walls and another with heat transfer at the walls. The flow field is assessed with focus on the differences between the two cases. The work was performed by Hellstrom under supervision by Prof. Fuchs. The results were presented at 48th AIAA Aerospace Sciences Meeting Including the New Horizons Forum and Aerospace Exposition 4-7 January 2010, Orlando, Florida by Hellstrom.

Paper 6

Assessment of Heat Transfer Effects on the Performance of a Radial Turbine using Large Eddy Simulation.
F. Hellstrom & L. Fuchs.
IMechE, 9th International Conference on Turbochargers and Turbocharging, 19-20 May 2010

The objective with this work is to assess the heat transfer effects on the turbine performance. The results show that the difference in the obtained shaft power is small. Even the differences in the time mean efficiency is small, it only differs with 2 percent units, even though the heat transferred to surroundings is as large as approximately 60 percent of the delivered shaft power. The work was performed by Hellstrom under supervision by Prof. Fuchs. The results were presented at the 9th International Conference on Turbochargers and Turbocharging, 19-20 May 2010 by Hellstrom.

Paper 7

On numerical computations of the unsteady flow field in a radial turbine: Assessment and validation of different modeling strategies
F. Hellstrom & L. Fuchs.
To be submitted.

Global results are compared with measured data for a radial turbine in this paper. Different turbulence modeling strategies, the RANS and LES approach, were used. Also, two different modeling approaches for the turbine wheel were used, the sliding mesh technique and the Rotational Reference Frame technique. The results show that the most advanced technique with sliding mesh and LES gave the best agreement with the measurements. The work was performed by Hellstrom under supervision by Prof. Fuchs.

Paper 8

Large Eddy Simulation of the Unsteady Flow in a Radial Compressor Operating Near Surge
F. Hellstrom, E. Gutmark & L. Fuchs.
To be submitted.

In this study, the results from LES of the flow in a radial compressor working at an operational point near surge was assessed. The flow field in the entire compressor stage is unsteady. Back-flow occurs in the diffuser, wheel and the ported shroud channels resulting in back-flow at the walls in the inlet region of the compressor. In the diffuser and volute, the flow is highly unsteady with perturbations that are convected around the volute, affecting the flow field in most of the entire compressor. The mechanism driving this unsteadiness is assessed by flow visualizations, frequency analysis and correlations of pressure and velocity data so as to gain more comprehensive understanding of the mechanism leading to stall and surge. The work was performed by Hellstrom under supervision by Prof. Gutmark and Prof. Fuchs.

Acknowledgements

First of all, I would like to thank my supervisor Professor Laszlo Fuchs. I am extremely grateful and appreciative of all your support, guidance and encouragement throughout the duration of this work. Without this, the path to the goal would have been so much longer and difficult. I look forward to more challenging collaborations in the future.

Also, a huge thankyou to all my colleagues at the Department at Mechanics, CICERO and the Department of Aerospace Engineering and Engineering Mechanics, University of Cincinnati for the support, guidance, answers and fruitful discussions. Special thanks are dedicated to Olle Bodin and my roommate Niklas Winkler, I will miss our discussions!

I would also like to thank my former employer GM Powertrain, Sweden AB and my present employer SAAB Automobile Powertrain AB, for making my PhD studies possible and I would especially like to thank Dr. Raymond Reinmann, Dr. Fredrik Westin and Per-Inge Larsson, for your support and also that you gave me the possibility to complete my PhD studies without any interruptions.

The Swedish Emission Research Program, Swedish National Energy Administration, GM Powertrain and SAAB Automobile Powertrain are acknowledged for their financial support. I would also like to thank the Sweden-America Foundation, Forskarskolan and SAAB Automobile Powertrain for the financial support which made it possible for me to spend six months at the Department of Aerospace Engineering and Engineering Mechanics, University of Cincinnati.

Furthermore, I would like to thank Professor Effie Gutmark for all your help and support during my time at the University of Cincinnati and that you and your family took care of us. Myself and my family are deeply appreciative of the hospitality that you, your wife Laura, and your daughter Iris showed us during our time in Cincinatti; we felt like we were members of the family Gutmark. Fanny, Nina and I will always remember the six months that we spent in Cincinnati as one of the best periods in our life! I also would like to thank Dr. Mihai Mihaescu for your help at UC, the useful discussions and all the fun that we had together. See you soon!

Last, but definitely not least, I would like thank my wife Nina and my daughter Fanny for all their support, patience and love!

References

Andersen, J., Karlsson, E. & Gawell, A. 2006 Variable turbine geometry on si engines. *SAE 2006 World Congress, Detroit, Michigan* **SAE 2006-01-0020**.

Anwer, M. So, R. M. C. & Lai, Y. G. 1989 Pertubation and recovery from bend curvature of a fully developd turbulent pipe flow. *Physics of Fluid* **1**, 1387–1397.

Arcoumanis, C., Karamanis, N., Martinez-Botas, R. & Su, C. C. 1999 Unsteady characteristics of a mixed-flow turbocharger turbine. *IMechE paper no C557/030* pp. 905–921.

Baines, C. N. 2005 Fundamentals of turbocharging. *Concepts NREC, ISBN 0-933283-14-8* .

Baines, N., Wygant, K. & Dris, A. 2009 The analysis of heat transfer in automotive turbocharger. *GT2009-59353, ASME Turbo Expo 2009: Power for Land, Sea and Air Orlando, USA* .

Baines, N. C. 1996 Flow development in radial turbine rotors. *ASME Paper no. 96-GT-65* .

Bardina, J., Ferziger, J. & Reynolds, W. 1980 Improved subgrid scale models for large eddy simulation. *AIAA Paper 80-1357* .

Barr, L., Spence, S. W. T., & McNally, T. 2006 A numerical study of the performance characteristics of a radial turbine with varying inlet blade angle. *ImechE Conference Transactions from 8th International Conference on Turbochargers and Turbocharging* pp. 169–181.

Benson, R. 1974 Nonsteady flow in turbocharger nozzleless radial gas turbine. *SAE 740739* pp. 1–11.

Benson, R. & Scrimshaw, K. 1965 An experimental investigation of non-steay flow in a radial gas turbine. *Instn Mech Engrs* **180**, 74–85.

Bohn, D., Heuer, T. & Kusterer, K. 2005 Conjugate flow and heat transfer investigation of a turbo charger. *Journal of Computational Physics of Engineering of Gas Turbines and Power* pp. 663–669.

Brucker, C. 1998 A time-recording piv-study of the swirl switching effect in a 90° bend flow. *Proceedings of the Eight International Symposium on Flow Visualizations, Sorento, Italy* .

Capobianco, M. & Gambarotta, A. 1990 Unsteady flow performance of turbocharger radial turbines. *C405/017, Proceeding of the Institute of Mechanical Engineers, Fourth International Conference, Turbocharging and Turbochargers* pp. 123–132.

Capobianco, M. & Gambarotta, A. 1992 Variable geometry and waste-gated automotive turbochargers: Measurements and comparision of turbine performance. *Transactions of ASME: Journal of Engineering for Gas Turbines and Power* **114**, 553–560.

Capobianco, M. & Gambarotta, A. 1993 Performance of a twin-entry automotive turbocharger turbine. *ASME, 93- ICE-2. Energy-Sources Technology Conference & Exhibition.* pp. 1–10.

Capobianco, M. & Marelli, S. 2005 Transient performance of automotive turbochargers: Test facility and preliminary experimental analysis. *SAE 2005-24-066, ICE 2005, 7th International Conference on Engines for Automobile* .

Capobianco, M. & Marelli, S. 2006 Turbocharger turbine performance under steady and unsteady flow: test bed analysis and correlation critera. *ImechE Conference Transactions from 8th International Conference on Turbochargers and Turbocharging* pp. 193–206.

Carpinlioglu, M. & Gundogdu, M. 2001 A critical review on pulsatile flow studies directing towards future research topics. *Flow measurements and Instrumentations* **12**, 165–174.

CD-adapco 2005 *Methodology manual*. STAR-CD Version 3.26.

Celik, I. B. 2005 Procedure for estimation and reporting of discretization error in cfd applications. *Internal report, Mechanical and Aerospace Engineering Department, West Virgina University, Morgantown Wv, USA, ismail.celik@mail.wvu.edu* .

Chapple, P., Flynn, P. F. & Mulloy, J. 1980 Aerodynamical design of fixed and variable geometry nozzleless turbine casings. *Transactions of the ASME Journal Eng for Power* **102**, 141–147.

Chen, H. 2006 Turbine wheel design for garrett advanced variable geometry turbines for commercial vehicle applications. *8th International Conference on Turbochargers and Turbocharging, Institution of Mechanical Engineers.* .

Chen, H. 2009 A discussion on volute design method for radial inflow turbines. *GT2009-59110, Proceedings of ASME TurboExpo 2009, June 8-12, Orlando, Florida, USA* .

Chen, H., Baines, N. C. & Abidat, M. 1997 Exit traverse study of mixed-flow turbines with inlet incidence variation. *Proceedings of the Institute of Mechanical Engineers* **211 Part A**, 461–475.

Chen, L., Zhuge, W., Zhang, Y., Li, Y. & Zhang, S. 2008 Investigation of flow structure in a turbocharger turbine under pulsating flow conditions. *SAE 2008-01-1691, SAE International Powertrains, Fuels and Lubrications Congress, Shanghai, China,* .

Chen, L., Zhuge, W., Zhang, Y., Li, Y. & Zhang, S. 2009 The effect of leading edge curvature on a mixed flow turbine under pulsating flow conditions. *GT2009-59004, Proceedings of ASME Turbo Expo 2009, Orlando, Florida, USA* .

Chou, C. & Gribbs, C. 1989 The design and testing of a mixed flow turbine for turbochargers. *SAE 890644* .

Copeland, C., Martinez-Botas, R. F. & Seiler, M. 2009 Comparision between steady and unsteady double-entry turbine performance using the quasi-steady assumption. *GT2009-59110, Proceedings of ASME TurboExpo 2009, June 8-12, Orlando, Florida, USA* .

Dale, A. & Watson, N. 1986 Vaneless radial turbocharger turbine performance. *ImechE Conference Transactions; "Turbochargers and Turbocharging", London* pp. 65–76.

Dambach, R. & Hodson, H. 2001 Tip leakege flow in a radial inflow turbine with varying gap height. *Journal of Propulsion and Power* **17**, 644–650.

Dec, J. E. & Keller, J. O. 1989 Pulse combustor tail-pipe heat-transfer dependence on frequency, amplitude and mean flow rate. *Combustion and flame* pp. 359–374.

Dec, J. E., Keller, J. O. & Hongo, I. 1991 Time-resolved velocities and turbulence in oscillating flow of a pulse combustor tail pipe. *Combustion and flame* **83**, 271–292.

Doran, W. J., Spence, S. W. T. & Artt, D. W. 2001 Experimental performance evaluation of a 99.0 mm radial inflow nozzled turbine with varying shroud profiles. *Proceedings of the Institute of Mechanical Engineers: Journal of Power and Energy* **215**, 267–280.

Ehrlich, D., Lawless, P. B. & Fleeter, S. 1997 On-engine turbocharger turbine inlet flow characterization. *SAE 971565, 8th Earthmoving industry Conference, Peoria, Illinios* .

Filipi, Z., Wang, Y. & Addanis, D. 2001 Effect of variable geometry turbine (vgt) on diesel engine and vehicle system transient respons. *SAE 2001 World Congress, Detroit, Michigan* **SAE 2001-01-1247**, 1–19.

Flaxington, A. & Swain, E. 1999 Turbocharger aerodynamic design. *Proceedings of the Institute of Mechanical Engineers* **Vol 213 Part C**, 43–57.

Fukaya, M., Watanabe, M. & Udagawa, T. 2000 Compressible turbulent flow analysis on variable nozzle vanes and spacer in turbocharger turbine. *SAE 2000 World Congress, Detroit, Michigan* **SAE 2000-01-0526**.

Futral, S. M. & Holeski, D. E. 1970 Experimental results of varying the blade-shroud clearence in a 6.02-inch radial-inflow turbine. *Tech. Rep.*. NASA TN D-5513.

Germano, M., Piomelli, U., Moin, P. & Cabot, W. 1991 A dynamic subgrid-scale eddy viscosity model. *Physics of Fluid* **3**, 1760–1764.

Ghosal, S., Lund, T., Moin, P. & Akselvoll, K. 1995 A dynamic localization model for large-eddy simulations of turbulent flows. *Journal of Fluid Mechanics* **286**, 229–255.

Gu, F., Engeda, A., Cave, M. & Liberti, J.-L. D. 2001 A numerical investigation on volute/diffuser interaction due to the axial distortion at the impeller exit. *Journal of Fluids Engineering* **123**, 475–483.

Guillou, E., Gancedo, M., DiMicco, R. G., Gutmark, E., Hellstrom, F., Mohamed, A. & Fuchs, L. 2010*a* Stall development in a ported shroud compressor using piv measurements and large eddy simulation. *SAE 2010 World Congress & Exhibition* .

Guillou, E., Gancedo, M., DiMicco, R. G., Gutmark, E., Hellstrom, F., Mohamed, A. & Fuchs, L. 2010*b* Surge characteristics in a ported shroud compressor usin piv measurements and large eddy simulation. *9th International Conference on Turbochargers and Turbocharging* .

Guo, Q., Chen, H., Zhu, X.-C., Du, Z.-H. & Zhao, Y. 2007 Numerical simulations of stall inside a centrifugal compressor. *Proceedings of the Institution of Mechanical Engineers, Part A: Journal of Power and Energy* **, Number 5 / 2007**.

Habib, M., Attya, A., Said, S., Eid, A. & Aly, A. 2004 Heat transfer characteristics and nusselt number correlation of turbulent pulating pipe air flows. *Heat and Mass Transfer* **40**, 307–318.

Hamakiotes, C. & Berger, S. 1988 Fully developed pulsatile flow in a curved pipe. *Journal of Fluid Mechanics* **195**, 22–55.

Hellstrom, F. & Fuchs, L. 2008*a* Effects of inlet conditions on the turbine performance of a radial turbine. *GT 2008-51088, ASME Turbo Expo 2008, Power for Land, Sea and Air, Berlin, Germany* .

Hellstrom, F. & Fuchs, L. 2008*b* Numerical computations of pulsatile flow in a turbo-charger. *AIAA-2008-073, 46th AIAA Aerospace Sciences Meeting and Exhibit, Reno, Nevada, 7-10 January 2008* .

Hellstrom, F., Renberg, U. & Westin, F. 2010 Predictions of the performance of a radial turbine with different modeling approaches: Comparison of the results from 1-d and 3-d cfd. *SAE 2010 World Congress & Exhibition* .

Issa, R. 1986 Solution of the implicity discretised fluid flow equations by operator-splitting. *Journal of Computational Physics* **62**, 40–65.

Issa, R., Ahmadi Befrui, B., Beshay, K. & Gosman, A. 1991 Solution of the implicitly discretised reacting flow equations by operator-splitting. *Journal of Computational Physics* **93**, 388–410.

Issa, R., Gosman, A. & Watkins, A. 1986 The computation of compressible and incompressible recirculation flows by a non-iterative implicit scheme. *Journal of Computational Physics* **62**, 66–82.

Iwasaki, Y., Ikeya, N., Marutani, Y. & Kitazawa, T. 1994 Comparison of turbocharger performance between steady flow and pulsating flow on engines. *SAE 900839, International Congress and Exposition, Detroit, Michigan, USA* .

Jeong, J. & Hussain, F. 1995 On the identification of a vortex. *Journal of Fluid Mechanics* **285**, 69–94.

Johansson, A. V. & Alfredsson, P. H. 1988 *Experimental methods in fluid mechanics*. Dept. of Mechanics, Royal Institute of Technology, Stockholm.

Karamanis, N. & Martines-Botas, R. F. 2002 Mixed flow turbines for automotive turbochargers: steady and unsteady performance. *Journal of Engine Research* **3**, 127–138.

KARAMANIS, N., MARTINEZ-BOTAS, R. & SU, C. 2001 Mixed flow turbines: Inlet and exit flow under steady and pulsating conditions. *ASME Journal of Turbomachinery* **123**, 359–371.

KLEIN, M., SADIKI, A. & JANICKA, J. 2003 A digital filter based generation of inflow data for spatially developing direct numerical or large eddy simulations. *Journal of Computational Physics* **186**, 652–665.

LAM, J. K. W., ROBERTS, Q. D. H. & MCDONNELL, G. T. 2002 Flow modelling of a turbocharger turbine under pulsating flow. *ImechE Conference Transactions from 7th International Conference on Turbochargers and Turbocharging, 14-15 May London UK* pp. 181–196.

LYNE, W. 1970 Unsteady viscous flow in a curved pipe. *Journal of Fluid Mechanics* **45**, 13–31.

MATTINGLY, G. & YEH, T. 1991 Effects of pipe elbows and tube bundles on selected types of flowmeters. *Flow Meas. Instrum* **2**, 4–13.

MOUSTAPHA, H., ZELESKY, M., BAINES, N. & JAPISKE, D. 2003 *Axial and radial Turbines*. Concepts NREC.

NAJAFI, A., SAIDI, M.S.AND SADEGHIPOUR, M. & SOUHAR, M. 2005 Numerical analysis of turbulent swirling decay pipe flow. *International Communications in Heat and Mass Transfer* **32**, 627–638.

PALFREYMAN, D. & MARTINEZ-BOTAS, R. 2005 The pulsating flow field in a mixed flow turbocharger turbine: An experimental and computational study. *ASME, Journal of Turbomachinery* **127**, 144–155.

PALFREYMAN, D., MARTINEZ-BOTAS, R. F. & KARAMANIS, N. 2002 Computational and experimental investigation of the aerodynamics of turbocharger mixed-flow turbines. *ImechE Conference Transactions from 7th International Conference on Turbochargers and Turbocharging, 14-15 May London UK* pp. 45–59.

PANTING, J., PULLEN, K. R. & MARTINEZ-BOTAS, R. F. 2001 Turbocharger motor-generator for improvement of transient performance in an internal combustion engine. *Proc Inst ImechE* **215, Part D**.

PESIRIDIS, A. & MARTINEZ-BOTAS, R. 2006 Active control turbocharger for automotive application: an experimental evaluation. *ImechE Conference Transactions from 8th International Conference on Turbochargers and Turbocharging* pp. 223–234.

RAJOO, S. & MARTINEZ-BOTAS, R. 2007 Improving energy extraction from pulsating flow by active control of a turbocharger turbine. *SAE 2007-01-1557* .

RAJOO, S. & MARTINEZ-BOTAS, R. 2008 Mixed flow turbine research: A review. *Journal of Turbomachinery* **130**.

RAMAPRIAN, B. R. & TU, S. W. 1983 Fully developed periodic turbulent pipe flow. part 2. the detailed structure of the flow. *Journal of Fluid Mechanics* **137**, 59–81.

ROGO, C., HAJEK, T. & CHEN, A. 1986 Variable stator radial turbine. *Tech. Rep.*. NASA CR-174663.

ROMAGNOLI, A. & MARTINEZ-BOTAS, R. 2009 Heat transfer on a turbocharger under constant load points. *GT2009-59618, ASME Turbo Expo 2009: Power for Land, Sea and Air Orlando, USA* .

Rutten, F., Schroder, W. & Meinke, M. 2005 Large eddy simulation of low frequency oscillations of the dean vortices in turbulent pipe bend flows. *Physics of Fluids* **17**.

Serrano, J., Guardiola, C., Dolz, V., Tiseira, A. & Cervello, C. 2007 Experimental study of the turbine inlet gas temperature on turbocharger performance. *SAE 2007-01-1559, World Congress Detroit, Michigan,USA* .

Shaaban, S. & Seume, J. 2006 Analysis of turbocharger non-adiabatic performance. *ImechE Conference Transactions from 8th International Conference on Turbochargers and Turbocharging* pp. 119–130.

Shaaban, S., Seume, J., Berndt, R., Pucher, H. & Linnhoff, H. 2006 Part-load performance prediction of turbocharged engines. *ImechE Conference Transactions from 8th International Conference on Turbochargers and Turbocharging* .

Simpson, A., Spence, S. W. T. & Early, J. 2009*a* A numerical and experimental study of the rotor inlet flow fields of radial turbines using vaned and vaneless stators. *GT2009-59998, Proceedings of ASME Turbo Expo 2009, Orlando, Florida, USA* .

Simpson, A., Spence, S. W. T. & J.K., W. 2009*b* A comparision of the flow structures and losses within vaned and vaneless stators for radial turbines. *Journal of Turbomachinery* **Vol 131**.

Spence, S., Rosborough, R., Artt, D. & McCullough, G. 2007 A direct performance comparison of vaned and vaneless stators of radial turbines. *Journal of Turbomachinery* **129**, 53–61.

Spence, S. W. T. & Artt, D. W. 1998 An experimental assessment of incidence losses in a radial inflow turbine rotor. *Proceedings of the Institute of Mechanical Engineers. Part A: Journal of Power and Energy* **212**, 43–53.

Steenbergen, W. & Voskamp, J. 1998 The rate of decay of swirl in turbulent pipe flow. *Flow Measurements and Instrumentations* **9**, 67–78.

Sudo, K. Sumida, H. & Hibara, H. 2000 Experimental investigation on turbulent flow through a circular-sectioned 180° bend. *Experiments in Fluids* **28**, 51–57.

Sudo, K., Sumida, H. & Hibara, H. 1998 Experimental investigation on turbulent flow through a circular-sectioned 90° bend. *Experiments in Fluids* **25**, 42–49.

Sun, Z., Tan, C. & Zhang, D. 2009 Flow field structures of impeller backside cavity and its influence on the centrifugal compressor. *Proceedings of ASME TurboExpo 2009, June 8-12, Orlando, Florida* .

Wallace, F., Adgey, J. & Blari, G. 1969 Performance of inward radial flow turbines under non-steady flow conditions. *Proc Instn Mech Engrs* **184**, 183–195.

Wallace, F. & Blair, G. 1965 The pulsating flow performance of invard radial flow turbines. *American Society of Mechanical Engineers* **Publ. 65-GTP-21**, 1–20.

Wang, X. & Zhang, N. 2005 Numerical analysis of heat transfer in pulsating turbulent flow in a pipe. *International Journal of Heat and Mass Transfer* **68**, 3957–3970.

Watanabe, T., Koike, T., Furukawa, H., Ikeya, N. & Sakakida, M. 1996

Development of a turbocharger for improving passenger car acceleration. *SAE 960018* .

Winterbone, D. E., Nikpour, B. & Alexander, G. I. 1990 Measurements of the perfomance of a radial inflow turbine in conditional steady and unsteady flow. *ImechE Conference Transactions, 4th International Conference: Turbocharging and turbocharging* **C405/015**, 153–160.

Winterbone, D. E., Nikpour, B. & Frost, H. 1991 A contribution to the understanding of turbocharger turbine perfomance in pulsating flow. *International Conference on Internal Combustion Research, Paper no C433/011. Inst. of Mech. Engrs.* pp. 19–28.

Yakhot, V., Orszag, S. A., Thangam, S., Gatski, T. B. & Speziale, C. G. 1992 Development of turbulence models for shear flows by a double expansion technique. *Physics of Fluids* **7**, 1510–1520.

Yeo, J. H. & Baines, N. C. 1990 Pulsating flow and behaviour in a twin-entry vaneless radial-inflow turbine. *ImechE Conference Transactions, 4th International Conference: Turbocharging and turbocharging.* **C405/004**, 113–122.

Part II

Papers

Paper 1

Paper 2

Paper 3

Paper 4

Paper 5

Paper 6

Paper 7

Paper 8